Magnetism, current-induced switchings and domain-wall propagation in single and exchange coupled Gd based ferrimagnets thin films

Jean-Loïs Bello

Magnetism, current-induced switchings and domain-wall propagation in single and exchange coupled Gd based ferrimagnets thin films

Thèse de doctorat de l'Université de Lorraine

en Physique

préparée à l'Institut Jean Lamour

présentée et soutenue à Nancy, le 28 mars 2022, par

JEAN-LOÏS BELLO

Composition du Jury :

Rapporteurs:	Stefania Pizzini	Institut Néel, France
	Gilles Gaudin	SPINTEC, France
Examinateurs:	Andrew Kent (Président)	New York University, USA
	Roman Morgunov	Institute of Problems of Chemical Physics, Russia
Directeur de thèse	Michel Hehn	Institut Jean Lamour, France
Co-directeur de thèse	Stéphane Mangin	Institut Jean Lamour, France

---

Institut Jean Lamour - UMR 7198 - Université de Lorraine

Département de Physique de la Matière et des Matériaux

Nanomagnétisme et Electronique de spin

Ecole doctorale C2MP

Magnetism, current-induced switchings and domain-wall propagation in single and exchange coupled Gd based ferrimagnets thin films

Thèse de doctorat de l'Université de Lorraine

en Physique

préparée à l'Institut Jean Lamour

présentée et soutenue à Nancy, le 28 mars 2022, par

JEAN-LOÏS BELLO

Composition du Jury :

Rapporteurs:	Stefania Pizzini	Institut Néel, France
	Gilles Gaudin	SPINTEC, France
Examinateurs:	Andrew Kent (Président)	New York University, USA
	Roman Morgunov	Institute of Problems of Chemical Physics, Russia
Directeur de thèse	Michel Hehn	Institut Jean Lamour, France
Co-directeur de thèse	Stéphane Mangin	Institut Jean Lamour, France

---

Institut Jean Lamour - UMR 7198 - Université de Lorraine

Département de Physique de la Matière et des Matériaux

Nanomagnétisme et Electronique de spin

Ecole doctorale C2MP

À mes parents

Acknowledgements

On m'avait prévenu que la thèse ne serait pas de tout repos et ça a été le cas. Mais une pandémie mondiale était-ce bien nécessaire ? Quelle aventure tout de même ! Je ne regrette aucunement de m'être lancé dans celle-ci. J'aurais tellement appris et grandi durant ces trois ans et demi aussi bien personnellement que professionnellement et j'en tire les bénéfices tous les jours dans la vie quotidienne.

Bien sûr tout cela n'a été possible que grâce à l'implication de nombreuses personnes que j'aimerais ici remercier en commençant évidemment par Michel Hehn, mon directeur de thèse. Michel, dès le premier jour où je suis arrivé en thèse, tu m'as formé et encadré. Très vite, j'ai été autonome et j'ai appris tellement de choses à tes côtés. Merci beaucoup pour toutes nos nombreuses discussions, pour ta disponibilité, ton aide et ton soutien. Ce fut un plaisir et un honneur de travailler avec toi.

J'aimerais également remercier mon autre directeur de thèse, Stéphane Mangin. Stéphane tu m'as accordé ta confiance en me prenant en thèse dans l'équipe et en me proposant d'aller en New York. Je te remercie énormément pour m'avoir donné cette opportunité mais également pour ton support et ton encadrement.

Je remercie très sincèrement Andrew Kent qui m'a donné l'immense chance de visiter le Center for Quantum Phenomena. J'ai passé 6 mois incroyables à New York et cela reste une des plus grandes expériences de ma vie. J'ai pu tellement évolué et progressé aussi bien scientifiquement que à titre personnel grâce à ce séjour.

Je tiens à remercier tous les membres de la Spin Team, merci à tous pour vos conseils, pour les réunions, pour l'aide que vous m'avez apporté ainsi que pour les bons moments partagés.

Je remercie également tous les membres de l'Institut Jean Lamour que j'aurais croisé durant mon doctorat et qui ont contribué de près ou de loin à ce travail. Je remercie les membres des centres de compétence, ceux-ci n'existent pas dans tous les labos et c'est une vrai chance d'avoir leur aide au quotidien. Je remercie particulièrement Laurent Badie pour sa grande aide et son extrême gentillesse.

Je souhaite remercier mes amis, qui auront été bien important dans les moments les plus durs. Ceux rencontrés

à l'IJL, Quentin, Charles, merci à vous. Ainsi que mes amis en dehors et en particulier Rudy, merci !
Enfin, last but not least, bien au contraire puisque c'est pour moi le plus important. Je remercie mes parents du fond de mon cœur, ils ont toujours été là depuis le tout début sans aucune exception et ont toujours été d'un support sans faille, aussi bien psychologiquement que matériellement. Je n'aurais pas pu réussir sans leur aide, c'est pourquoi je leur dédie ce travail de thèse. Papa, Maman, merci beaucoup ! Je vous aime !

It has been one hell of a ride !

Titre: Magnétisme, retournements d'aimantation par courant et propagation de parois de domaine dans des couches minces simples et couplées de matériaux ferrimagnetiques à base de Gd

Mots clés: Dépôt de couches minces, Matériaux ferrimagnétiques, Antiferromagnétiques synthétiques, Couple de transfert de spin, Parois de domaine, Electronique de spin

Résumé: Les découvertes qui ont suivi l'émergence de l'électronique de spin ont révolutionné le domaine de la télécommunication et du stockage de données. L'électronique de spin est un champ de recherche qui combine l'étude d'une propriété intrinsèque de l'électron appelée spin qui est liée à un moment magnétique intrinsèque et la charge de l'électron. Dans un monde où la consommation d'énergie entrainée par le trafic internet et le stockage de l'information double tous les 4 ans en moyenne, l'électronique de spin doit faire face à de nouveaux défis. Afin de satisfaire les besoins d'un stockage plus dense, plus rapide et moins couteux en énergie, la manipulation de l'aimantation au moyen de courant de spin est très prometteur et permet de proposer de nouveaux dispositifs utilisant la propagation de parois magnétiques sous l'effet de courant.

Les matériaux dont l'aimantation est perpendiculaire au plan de la couche ont été l'object d'intenses recherches et sont cruciaux dans le développement de mémoires magnétiques telles que les disques durs ou les MRAM. Parmi ces matériaux, les films minces d'alliage amorphe terre rare / métal de transition sont connus pour leurs intéressanftes propriétés magnétiques. Une aimantation perpendiculaire pour de faibles anisotropies peut être stabilisé et la compensation du moment magnétique total peut être obtenu en fonction de la composition et de la température. En plus des champs magnétiques, il a été montré que l'aimantation peut être retournée au moyen de courant polarisé en spin ou par pulse laser femto-seconde. Puisque ces alliages ferrimagnétiques terre-rare/métal de transition semblent prometteurs, nous avons concentré notre travail sur des multicouches qui inclus ces matériaux.

On rapporte en premier la dépendance des propriétés magnétiques de couches simples d'alliage ferrimagnétique $Gd_x(Fe_{90}Co_{10})_{100-x}$ en fonction de la composition et de la nature des interfaces. Des couches de 5 nm de $Gd_x(Fe_{90}Co_{10})_{100-x}$ ont été intégrées dans différentes multicouches, toutes déposées par pulvérisation cathodique magnétron. Pour des valeurs de x comprises entre 22% et 33 %, nous montrons que la composition à laquelle intervient la compensation magnétique dépend des couches au dessus et en dessous de notre alliage. Nous avons étudié différentes interfaces M/GdFeCo/N avec M ou N = Cu, Pt, Ta, Ir. Puis, nous avons élaboré un empilement GdFeCo/Ir/GdFeCo en variant l'épaisseur d'Ir. Nous montrons qu'il est possible d'obtenir un couplage antiferromagnétique entre les couches de GdFeCo. De telles structures, appelées antiferromagnétiques synthétiques se sont révélées performantes quant à la vitesse de propagation de parois de domaines. Dans cette thèse, nous proposons de combiner les propriétés du GdFeCo ainsi que celles du couplage antiferromagnétique.

Dans des dispositifs micrométriques, nous avons ensuite étudié le retournement de l'aimantation sous l'effet de couple de spin dans nos systèmes antiferromagnétiques synthétiques ainsi que dans les couches simples qui les composent. Si le retournement de l'aimantation conventionnel qui requiert un champ magnétique externe a pu être observé, nous avons également trouvé que le renversement s'obtient en l'absence de champ externe. Après de plus amples investigations, notamment par l'imagerie de domaines magnétiques au moyen d'un microscope Kerr, nous avons montré qu'il s'agit de l'effet du champ généré par l'injection de courant (champ d'Oersted) qui ne peut pas du tout être négligé dans nos échantillons. Cela conduit à un comportement de l'aimantation très particulier et affecte fortement le retournement par couple de spin.

Enfin, nous avons regardé la propagation de parois de domaines et nos résultats préliminaires montrent des propriétés intéressantes à condition d'éliminer le champ induit par le courant. Cette étude nous a donné des premières pistes à explorer en fonction des nombreuses interactions et paramètres qui peuvent être ajuster dans les antiferromagnétiques synthétiques à base de GdFeCo.

Title: Magnetism, current-induced switchings and domain-wall propagation in single and exchange coupled Gd based ferrimagnet thin films)

Keywords: Thin films deposition, Ferrimagnets, Synthetic antiferromagnets, Spin-Torques, Domain-wall, Spintronics

Abstract: The discoveries ensuing the emergence of spintronics have revolutionized technology, especially in communication and data storage. Spintronics is a field of research that combines the study of an intrinsic property of the electron, the *spin* to which is bound an intrinsic magnetic moment and the *charge* of the electron. In a world where the energy consumption of internet traffic and data storage doubles every four years, Spintronics faces new challenges. To meet the need to increase the density, the operation speed and to lower the power consumption of memory devices, using spin-currents to manipulate the magnetization is very promising and has led to new ideas of possible devices in which such currents are used to propagate magnetic domain-walls.

Materials with perpendicular to film plane magnetization have been the subject of intense research and they are crucial for the development of magnetic memories such as hard disk drive or MRAM. Among those, amorphous rare-earth transition-metal GdFeCo thin films are well-known to exhibit many interesting magnetic properties. Perpendicular magnetization can be stabilized with weak anisotropies and a total moment compensation can be achieved depending on the concentration and the temperature. In addition to magnetic fields, its magnetic moment has been shown to be switched either by single femtosecond laser pulse or spin-orbit torque. Since this material appears to be promising for future spintronics applications, we focused on the study of the magnetic properties of multilayers that include this material.

We first report the dependence of magnetic properties in $Gd_x(Fe_{90}Co_{10})_{100-x}$ ferrimagnetic alloys single layers on the composition and on the nature of the interfaces. 5nm thick $Gd_x(Fe_{90}Co_{10})_{100-x}$ layers were integrated in different multilayers, all grown by magnetron sputtering. For x between 22% and 33%, we show that the composition at which the magnetic compensation occurs changes depending on the layers under and over the TE-RM layer. We studied different interfaces M/GdFeCo/N with M or N = Cu, Pt, Ta, Ir. Then, for GdFeCo layers having out of plane magnetization, more complex structures have been grown associating two GdFeCo layers. Especially, we grew GdFeCo/Ir/GdFeCo with varying Ir thickness. We show that it is possible to have an antiferromagnetic coupling. Those synthetic antiferromagnets are proven to improve the velocity of propagation of magnetic domain-wall. In our work, we propose to combine the properties of such a structure with the ones of GdFeCo.

After micro-fabrication of devices, we have first investigated the magnetization reversal induced by spin-torques in our synthetic antiferromagnetic systems and the layers that compose them. If standard switching that requires an external magnetic field has been observed, we also have found that switching occurs in the absence of magnetic field. After further measurements, especially with magnetic domain imaging with a Kerr microscope, we have shown that the field induced by the current injection cannot be neglected, leads to a peculiar behavior of the magnetization in our devices and strongly affects spin-torque switching.

Finally, we looked into the domain-wall propagation and our preliminary results show promising features at the condition to eliminate the current-induced fields. This study has given us first hints and possibilities to be explored as a function of the numerous interactions and parameters that can be tuned especially in GdFeCo-based synthetic antiferromagnets.

Contents

Chapter 1

Introduction

The improvements of growth techniques had helped to observe for the first time in 1988 the giant magnetoresistance (GMR) effect in spin valve[1] (for this discovery, the Nobel Prize was awarded to Albert Fert and Peter Grünberg in 2007). A spin valve is a system that consists in superposing two magnetic layers separated by a thin non-magnetic conductive spacer. When a current flows through the system, the conductivity will depend on the respective orientation of the magnetization of each layer (fig.1.1). For example, the difference of resistance at room temperature can go up to 110% for Co-Fe/Cu multilayers[2] giving new ideas for memory storage devices. The first success was a magnetic read head based on spin valve structure that permits to increase the storage areal density of hard disk drive. In parallel of the development of the spin-valve head, it was predicted in 1996[3–6] that the spin angular moment of a spin-polarized current could be transferred to the magnetization of a layer. For example, in a spin-valve, the magnetization of one layer is pinned so a current flowing through it will acquire a spin-polarization. The polarized electrons, due to the exchange interaction, will then align their moment with the magnetization of the free layer. To respect the total angular momentum conservation law, the magnetization of the free layer will tend to be aligned towards the direction of the magnetic moments of the spin-current, this is spin-transfer torque (STT). In the case of STT, a spin-current is generated because of the band structure of the magnetic materials. Indeed, the strong exchange interaction has the consequence of shifting differently in energy the spin-up and the spin-down bands that is the origin of the ferromagnetic moment. From this shift, the spin-conserving transitions and the spin-dependent scattering probabilities, it results in two different channels of conduction[7].

The discovery of the GMR has been the starting point of a new field of research in magnetism: Spintronics.

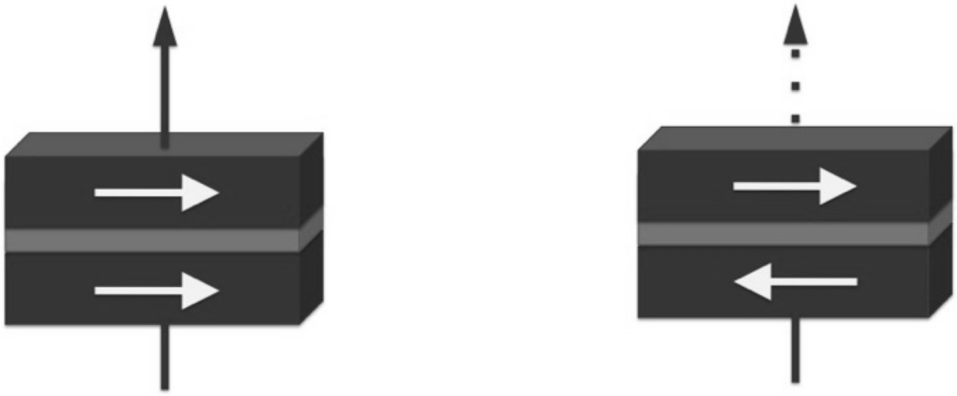

Figure 1.1: Schematic of a current through a spin valve in the case of low conductivity when the magnetizations alignment is antiparallel

To meet the need to increase the density, the operation speed and to lower the power consumption of memory devices, magnetic materials are the subject of intense research. The possibility to deposit dozens of nanometers or less thin layers has allowed more control of the anisotropy of the magnetic materials and to obtain hysteresis cycle of the magnetization which is essential for memory devices. Moreover, it is a key point to have an efficient way to manipulate their magnetization to encode data. Before the emergence of spintronics, only magnetic fields were used to read and write the information. The generation of spin polarized currents, their injection in complex magnetic structures and spin transfer torques have been game-changing results. More recently, a new way of generating spin currents and creating a torque on the magnetization has been considered: spin-orbit torques (SOT).

1.1 Spin-dependent Hall effects and spin-orbit torques

In condensed matter physics, the Dirac equation, relativistic analogue of Schrödinger equation describes relativistic particles. For a spin-$\frac{1}{2}$ free particle in the presence of an electromagnetic field, it takes this form:

$$i\hbar\frac{\partial\psi(\boldsymbol{r},t)}{\partial t} = \hat{H}\psi(\boldsymbol{r},t) = (c\tilde{\boldsymbol{\alpha}}.(\hat{\boldsymbol{p}} - q\boldsymbol{A}(\boldsymbol{r},t)) + \tilde{\beta}mc^2 + q\phi(\boldsymbol{r},t))\psi(\boldsymbol{r},t) \tag{1.1}$$

where m and q are respectively the mass and the charge of the particle and c is the speed of light. $\psi(\boldsymbol{r},t) = \sum\psi_n(\boldsymbol{r},t)$ the superposition of N base wavefunctions is a column vector, $\tilde{\boldsymbol{\alpha}} = \begin{bmatrix} 0 & \boldsymbol{\sigma} \\ \boldsymbol{\sigma} & 0 \end{bmatrix}$, $\tilde{\beta} = \begin{bmatrix} 1 & 0 \\ 0 & -1 \end{bmatrix}$ in compact notation are 4×4 matrices, $\hat{\boldsymbol{p}} = -i\hbar\nabla$ the momentum operator, $\boldsymbol{A}(\boldsymbol{r},t)$ the vector potential and $\phi(\boldsymbol{r},t)$

the electric potential.

For an electron in the field of a proton i.e. in a spherically symmetric scalar potential, $\boldsymbol{A}(\boldsymbol{r},t) = 0$ and $\phi(\boldsymbol{r},t) = \phi(r)$, the equation becomes:

$$i\hbar\frac{\partial\psi(\boldsymbol{r},t)}{\partial t} = (c\tilde{\boldsymbol{\alpha}}.\hat{\boldsymbol{p}} + \tilde{\beta}mc^2 - q_e\phi(r))\psi(\boldsymbol{r},t) \tag{1.2}$$

To obtain the relativistic corrections from the previous equation, we can write the Hamiltonian in the weakly relativistic domain as a power series expansion in $\frac{v}{c}$[8]:

$$\hat{H} = m_ec^2 + \underbrace{\frac{\hat{\boldsymbol{p}}^2}{2m_e} + V(R)}_{H_0} - \underbrace{\frac{\hat{\boldsymbol{p}}^4}{8m_e^3c^2}}_{W_{mv}} + \underbrace{\frac{1}{2m_e^2c^2}\frac{1}{R}\frac{dV(R)}{dR}\hat{\boldsymbol{L}}.\hat{\boldsymbol{S}}}_{W_{SO}} + \underbrace{\frac{\hbar^2}{8m_e^2c^2}\Delta V(R)}_{W_D} + ... \tag{1.3}$$

H_0 corresponds to the non-relativistic Hamiltonian, W_{mv} corresponds to the correction of the energy due to the relativistic variation of the mass with the velocity and W_D is called the Darwin term and is a correction due to the non-local interaction between the electron and the field of the nucleus. The part that we are interested in, is W_{SO} and it describes the spin-orbit coupling (SOC). This coupling can be understood as the movement of the electron in the electrostatic field created by the proton. Then, according to special relativity, the electron sees its own-generated magnetic field in his frame. The SOC is the interaction between this field and the intrinsic magnetic moment of the electron ($\boldsymbol{M_s} = \frac{q_e\boldsymbol{S}}{m_e}$).

The relativistic spin-orbit coupling is at the origin of a number of phenomena that are used for the manipulation of magnetic materials. One of them is the anomalous Hall effect (AHE). Similar to the ordinary Hall effect (OHE) in a metal kept in a magnetic field, it generates a transverse voltage via a longitudinal charge current usually in a ferromagnetic (FM) metal. The AHE originates from three main mechanisms in solids with broken time-reversal symmetry as a consequence of spin-orbit coupling[9]:

- The intrinsic deflection which depends only on the band structure crystal and is related to the Berry's phase curvature of the electrons
- The side-jump which can be understood as the displacement of the wave vector of a wave packet by an impurity with SOC
- The skew-scattering which is the mechanism proportional to the Bloch state transport lifetime: the tran-

sition probability from a state to another is the same than the reversed transition but these probabilities are asymmetric in the presence of SOC.

All these effects can be seen as spin-dependent scattering and because of the difference of population between the majority and minority carriers in ferromagnets, a transverse voltage can be measured and can be used to locally probe the magnetization of the material (fig.1.2). The Hall resistivity is $\rho_H = R_{OHE}\mu_0 H_z + R_{AHE}\mu_0 M_z$ where R_{OHE} and R_{AHE} are respectively the ordinary and extraordinary Hall coefficients, H_z is the perpendicular magnetic field and M_z is the perpendicular component of the magnetization.

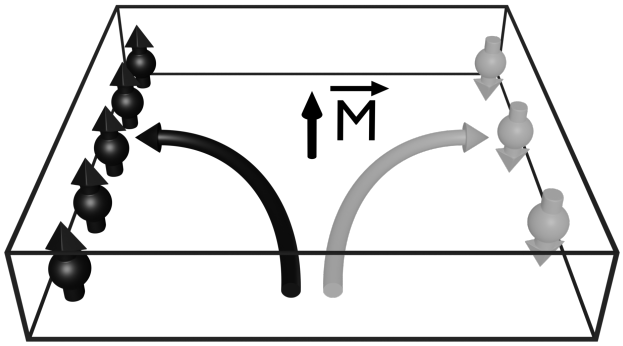

Figure 1.2: Schematic representation of the Anomalous Hall Effect

Spin Hall effect (SHE) is quite the same effect in a non-magnetic (NMs) material. Thus a pure spin current is generated and a spin accumulation of opposite sign appears at opposite edges instead of a transverse voltage (fig.1.3 (right)). Initially depicts as Mott scattering in a solid, the SHE is actually quite more complex and takes its origin from the three same microscopic mechanisms (intrinsic, side-jump, and skew-scattering)[10]. In 2007, it has been experimentally demonstrated that is possible to inject a spin current in a FM via a NM attached to it and reciprocally (ISHE: Inverse Spin Hall Effect)[11]. The spin current generated from a charge current is defined as $\boldsymbol{J_s} = \frac{\hbar}{2e}\theta_{SH}\boldsymbol{J_c} \times \boldsymbol{\sigma}$ with $\boldsymbol{J_s}$ and $\boldsymbol{J_c}$ respectively the spin and the charge current, $\boldsymbol{\sigma}$ the polarization of the spin current and θ_{SH} is the spin Hall angle which is the efficiency of the charge to spin conversion defined as the ratio of the spin-current to the charge current in a heavy metal (HM) layer. The injection of a spin current, created in a NM, in a FM results in a STT that can be called SHE-STT or SOT. One should note that $\boldsymbol{J_s}$, $\boldsymbol{J_c}$ and $\boldsymbol{\sigma}$ are mutually orthogonal (fig.1.3 (left)) which implies that a charge current injected in the film plane can only leads to a in-plane polarization at the film surface. Thus it is needed to apply an in-plane field on perpendicularly magnetized material in order to obtain a torque.

However, it has been discovered that SHE is not the only mechanism responsible for the torque applied on

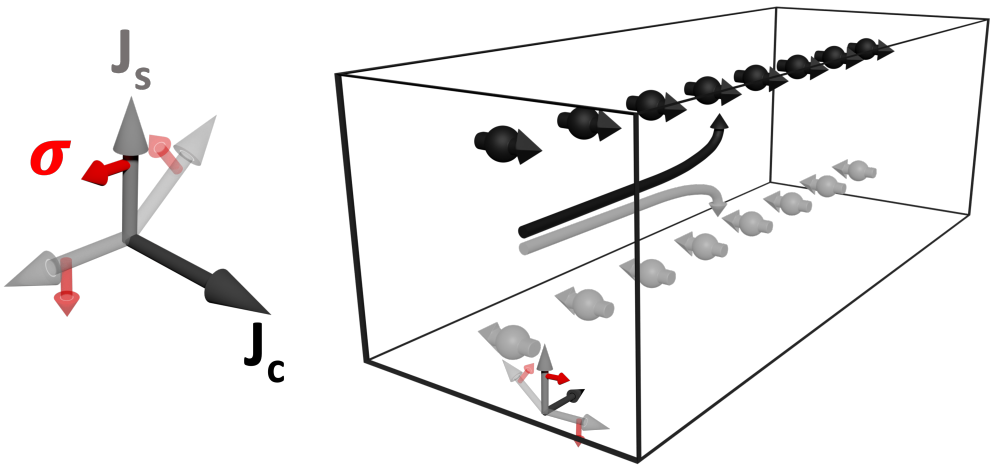

Figure 1.3: Schematic representation of the Spin Hall Effect (left) and geometry of the spin to charge conversion (right)

the adjacent layer. In a such system, the structural inversion symmetry is broken by the interface FM-NM which gives rise to the so-called spin galvanic phenomena. Among these phenomena, it is the spin galvanic effect that has been discovered first in an asymmetrically confined two-dimensional electron gas[12]: an electrical current is induced by a nonequilibrium, but uniform, polarization of electron spins. In spintronics, the inverse spin galvanic effect (ISGE) also known as the Edelstein effect, is really interesting since it generates a spin polarization from an electrical current. The microscopic origin of this effect is an electric-field and k-dependent spin flip scattering induced redistribution of carriers on the Fermi surface whose spin texture has an inversion asymmetry. It results from this redistribution, a nonzero spin density and if the spins are exchange coupled to magnetic moments of the adjacent layer then a torque is applied (fig.1.4).

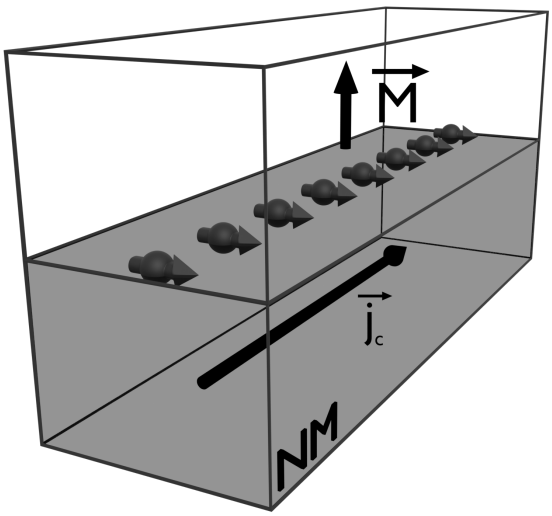

Figure 1.4: Schematic representation of the Inverse Spin Galvanic Effect

For materials without a strong SOC or breaking of inversion symmetry, the typical Fermi contour of the band structure is represented in figure 1.5 (left). At a Rashba interface with strong SOC, the spin degeneracy of the band structure is lifted (fig.1.5 (center)). With the ISGE, the Fermi contour is displaced under a charge current. Since the spin-momentum locking of the spin texture implies that for k_x the next spin state is s_y, and respectively for k_y the next spin state is s_x, a spin accumulation results from the displacement of the Fermi contour (fig.1.5 (right)).

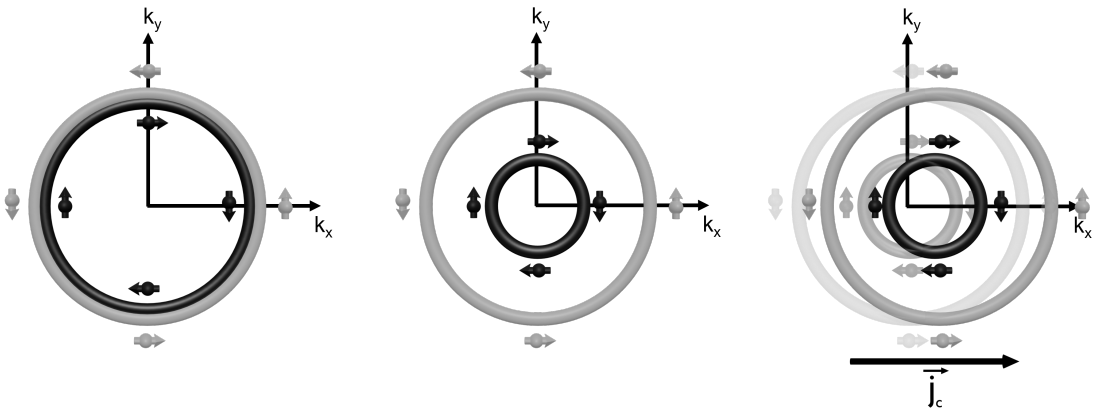

Figure 1.5: Schematic of the Fermi contour for a material without SOC or breaking of inversion symmetry (left), the Rashba spin texture with lifted spin degeneracy (center), the Rashba contour under the effect of a charge current j_c (right)

1.2 Magnetization dynamics induced by spin-orbit torques

As seen in the previous paragraph, SHE and ISGE are two companion effects that allow us to generate SOTs and therefore to manipulate the magnetization without external magnetic fields. The dynamics of the magnetization under STT and/or SOT is described by a phenomenological equation known as Landau-Lifshitz-Gilbert (LLG) equation:

$$\frac{d\boldsymbol{m}}{dt} = \underbrace{-\gamma\mu_0 \boldsymbol{m} \times \boldsymbol{H}_{eff}}_{precession\ term} + \underbrace{\alpha \boldsymbol{m} \times \frac{d\boldsymbol{m}}{dt}}_{damping\ term} + \underbrace{\frac{\gamma}{M_s}\boldsymbol{T}}_{torques\ term} \tag{1.4}$$

where γ is the value of the gyromagnetic ratio (1.76×10^{11} rad s^{-1} T^{-1} for free electrons), α is the Gilbert damping parameter (dimensionless), M_s is the saturation magnetization, $\boldsymbol{m} = \boldsymbol{M}/M_s$ is the magnetization unit vector and $\boldsymbol{H}_{eff}$ is an effective magnetic field that takes in account the demagnetization, anisotropy and exchange contributions. If the anisotropy and the exchange stiffness are defined by material constants, respec-

tively K (J/m) and A (J/m^3), the demagnetizing field (or stray field) is defined like:

$$\boldsymbol{H_d} = -\mathcal{N}\boldsymbol{M} = -\begin{bmatrix} N_x & 0 & 0 \\ 0 & N_y & 0 \\ 0 & 0 & N_z \end{bmatrix} \boldsymbol{M} \tag{1.5}$$

$\mathcal{N}$, the demagnetization tensor is determined by the shape of the magnetic material. In the case of a large thin film that exhibits perpendicular magnetic anisotropy (PMA), as is the case for all the samples in this thesis, we have $N_x = N_y = 0$ and $N_z \approx 1$. We can notice from here that the anisotropy in PMA material has to be larger than the demagnetization energy (expressed as $-\frac{\mu_0}{2}\int_V \boldsymbol{H_d}.\boldsymbol{M}\,dV$) since this one is maximal when the magnetization points perpendicular to the plane of the film. We can then define an effective perpendicular anisotropy as:

$$K_{eff} = K - \frac{1}{2}\mu_0 M_s^2 \tag{1.6}$$

Hence, if $K_{eff} > 0$, the magnetization will be out of plane since the PMA is larger than the demagnetization energy. Finally, the torques term of the LLG equation, $\boldsymbol{T}$ represents the different torques that have an effect on the magnetization and may not derive from an energy density such as the effect of a charge current. We will consider here the general expression of $\boldsymbol{T}$:

$$\boldsymbol{T} = \tau_{FL}\boldsymbol{m} \times \boldsymbol{\zeta} + \tau_{DL}\boldsymbol{m} \times (\boldsymbol{m} \times \boldsymbol{\zeta}) \tag{1.7}$$

τ_{FL} and τ_{DL} are coefficients and $\boldsymbol{\zeta}$ is a unit vector. They depend on the considered mechanism. For instance, in the case of STT, $\boldsymbol{\zeta}$ is the polarization vector and is aligned with the magnetization direction of the polarization layer. In the case of SOT, $\boldsymbol{\zeta}$ depends on the spin current generated by SHE and thus the sign of the spin Hall angle. τ_{FL}, for field-like, is the component that acts like a uniform magnetic field similarly to the precession term of eqn.1.4. It is the transverse component of the torque, normal to the $(\boldsymbol{m}, \boldsymbol{\zeta})$ plane. τ_{DL}, for damping-like (also called Slonczewski-like), is the longitudinal component. It acts like an effective damping (equivalent to the damping term in eqn.1.4), and lies in the $(\boldsymbol{m}, \boldsymbol{\zeta})$ plane (fig.1.6).

Historically, the damping-like component was observed in a NM/FM bilayers by a change in the damping parameter measured by ferromagnetic resonance (FMR) and induced by an in-plane DC current[13]. This is a consequence of the SOT that can thus creates a small angle FMR precession. The dynamics of ferromagnet is then useful to measure the SHE of non-magnetic heavy metal. But from these experiments, it has been

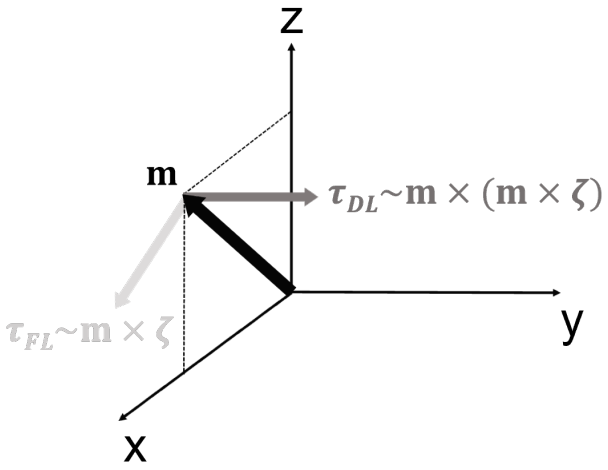

Figure 1.6: Schematic of the geometry of the different torques applied on the magnetization for $\boldsymbol{\zeta} = \boldsymbol{y}$

discovered that for large enough current, the SOT can even fully switch the magnetization. This discovery paved a new way to manipulate the magnetization. If SOT can seem similar to STT, there are some fundamental differences: for STT, the current is injected perpendicular to the plane of the heterostructure and a current flows through the reference layer and the polarized electrons transfer their spin-angular momentum to the recording ferromagnet. In order to increase the efficiency, it is possible to increase the current intensity or to choose materials with low magnetic damping[3]. Unfortunately, the switching process via STT, in magnetic tunnel junction (MTJ) for example, is limited by thermally activated oscillations since there is no STT when both layers are parallel or anti-parallel leading to an important incubation time. Ultrafast switching can be achieved with high currents but at the cost of damaging ultrathin oxide barriers. Moreover, the read and write paths are the same causing some reading disturbances. The geometry of SOT is different, the electrons are injected in the plane of the bilayer NM/FM and it has been proved that it is a very efficient way to manipulate magnetization[14]. One of the advantages for PMA devices is that the torque is always perpendicular to the magnetization reducing the incubation time. Also, for MTJs, writing and reading paths are separated and it avoids electrical stress in the tunnel barrier. Then, memory devices using MTJs are very promising since the switching speed of SOT-MRAM is superior[15], however, it remains one major limitation for SOT switching. When a current is injected in the system, the magnetization is brought to the equator by the exerted torque but both perpendicular states are stable because of the PMA (fig.1.7 left). To break the symmetry of the system, an in-plane magnetic field is needed to tilt the magnetization toward the opposite axis in order to reverse the magnetization (fig.1.7 right). A permanent in-plane magnetic field is obviously not convenient for applications such as magnetic memories and some experimental solutions have already been found. The field free SOT switching or zero field switching

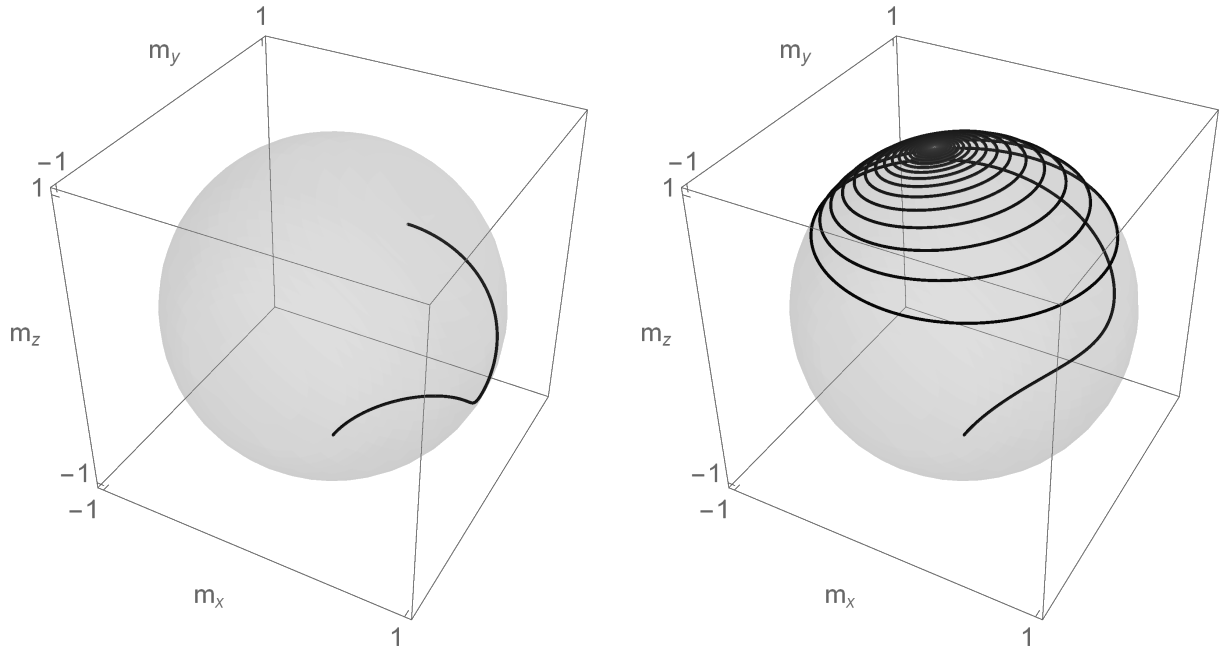

Figure 1.7: Simulation of the magnetization dynamics under a SOT, based on the numerical solution of LLG equation for $\boldsymbol{\zeta} = \boldsymbol{y}$ with $H_x = 0\ T$ (left) and with $H_x = 0.01\ T$ (right)

has been shown in antiferromagnet(AFM)/ferromagnet structures where the exchange bias exerted by the AFM contributes to an effective in-plane magnetic field[16–18]. The in-plane field can also be replaced by a pinned magnetic layer exchange coupled with the free layer[19] or by tuning the polarization of the spin current[20]. In MTJs, the zero-field switching through the interplay of SOT and STT has been demonstrated[21] but also by combining the junction with an AFM[22]. Finally, an other way to get rid of the magnetic field is the use of wedged layers such as a wedge in the thickness of the sample[23] or in the composition of the material[24].

1.3 A promising material: GdFeCo ferrimagnet

GdFeCo is an amorphous rare earth-transition metal (RE-TM) alloy. The magnetism of this alloy comes from two different sub-lattices[1]: the Gd $4f$ shell and both Fe/Co $3d$ magnetic moments and mobile s-p spins. These moments are antiferromagnetically coupled (fig.1.8 (left)) and this coupling is mediated by Gd $5d$ electrons via $4f$-$5d$ exchange interaction and $3d$-$5d$ hybridization[25,26] and indirect RKKY conduction band exchange. Due to this unique configuration, its magnetic properties (net magnetization, anisotropy, and Curie temperature) can be tuned by changing the composition. Moreover, an other particularity of the GdFeCo resides in the different

[1] the term lattice is here abusive since the metal is amorphous and does not exhibit a crystallographic structure

Landé g factors of the rare earth ($g_{Gd} \approx 2$) and transition metal elements ($g_{FeCo} \approx 2.2$) causing different compensation temperatures of magnetization and angular momentum[27], at which, respectively, the magnetizations and angular momenta of both sub-lattices have the same magnitude but opposite directions.

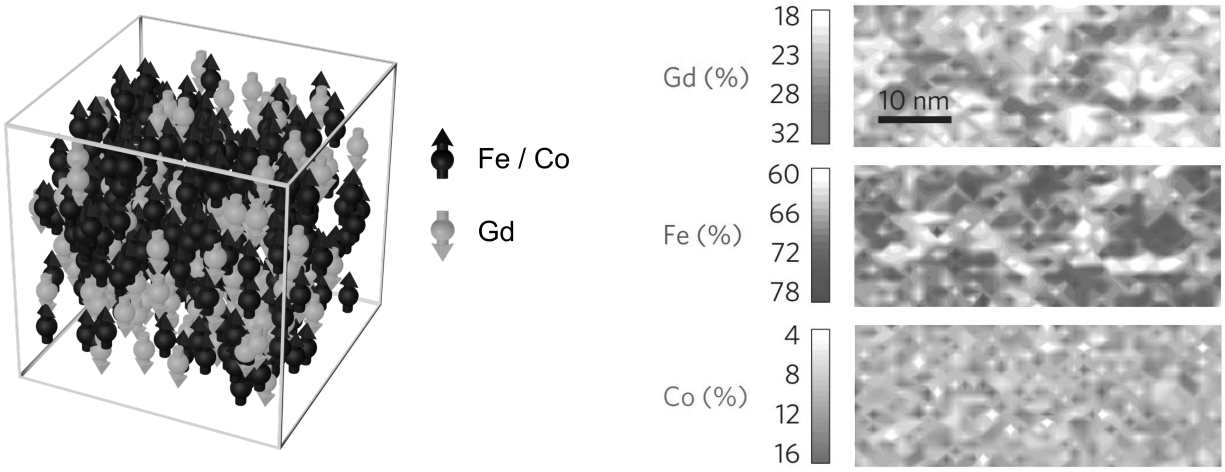

Figure 1.8: Schematic of the magnetic moments distribution in GdFeCo (left) and local charge nanoscale variations for Gd, Fe and Co in $Gd_{24}Fe_{66.5}Co_{9.5}$ measured with STEM–EDX adapted from [28] (right)

The typical thin film composition of the GdFeCo used in a lot of application is $Gd_x(Fe_{90}Co_{10})_{100-x}$ and as seen before the interplay between the two sub-lattices is at the origin of highly tunable properties with the composition. Because this alloy is amorphous, the elements are not periodically and symmetrically ordered and it has been shown that the composition is inhomogeneous along the film plane (fig.1.8 (right)). Depending of the composition or the temperature, the total magnetization can be dominated either by the Gd sub-lattice total moment (Gd-rich) or by the FeCo sub-lattice total moment (FeCo-rich). It is important to note that if, usually, magnetic characterization methods probe average values of the system, if it is close to the compensation, it can be very sensitive to the film inhomogeneity. GdFeCo thin films are well-known to exhibit many interesting spintronics features. Among those properties, perpendicular to film plane magnetization could be stabilized with weak anisotropies which is still not well understood and the weak stray field because of the antiferromagnetic alignment of the moments is not sufficient to explain it.

In addition to magnetic fields, its magnetic moment has been shown to be switched either by SOT (fig.1.9 (left)) or single femtosecond laser pulse by all-optical switching (AOS) (fig.1.9 (right)). In 1996, the ultrafast demagnetization of a nickel thin film using femtosecond laser pulses[29] has paved the way to the magnetic ultrafast reversal using light. A decade ago, the all-optical switching (AOS) of a GdFeCo thin film[30] has been shown before that this phenomenon was observed in a broader variety of materials[31,32]. GdFeCo was already used in magneto-optical recording[33] and known for its strong magneto-optical effects[34]: the Faraday rotation

is about 200 times higher than that in orthoferrites (materials known to modify the polarization of light under the effect of a magnetic field) in which strong inverse Faraday effect has been observed[35]. Furthermore, these effects are not only useful to manipulate the magnetization but also they allow us to easily probe and observe the magnetization of the GdFeCo, which is also known to exhibit large magnetic domains, using polarized light techniques such as Kerr microscope as it will be presented in the second chapter.

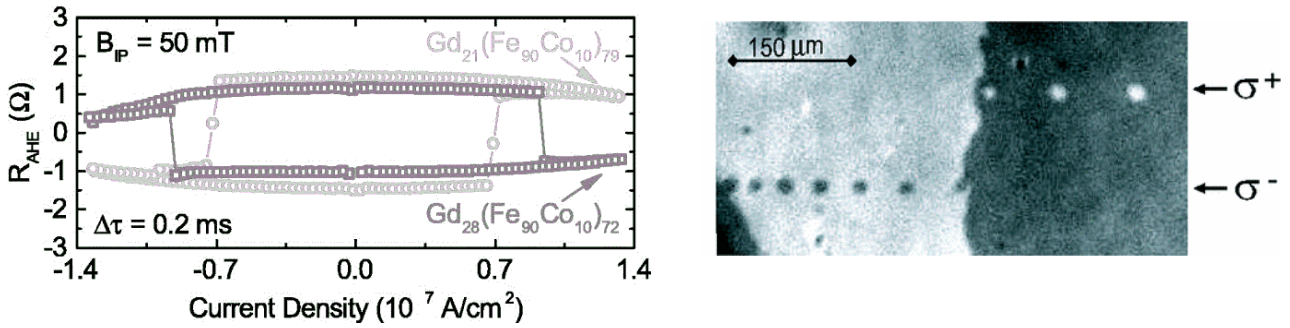

Figure 1.9: (Left) SOT switching of the magnetization with an in-plane field of 50 mT and a pulse width of 200 μs adapted from [36]. (Right) All-optical magnetic switching by 40-fs long laser pulses on magnetic domains in $Gd_{22}Fe_{74.6}Co_{3.4}$ adapted from [30].

GdFeCo seems also to be a good candidate to be integrated in domain wall devices. Proposed 15 years ago[37,38], the racetrack memories are magnetic nanowires in which data are stored in sequences of magnetic domains that can be moved using spin-currents to bring them to read or write devices. In this technology, the demagnetizing field coming from each domain leads to strong dipolar interactions between them and limits the density[38,39]. In ferrimagnets, the demagnetizing field is reduced and high velocities have already be shown in GdFeCo wires[40]. Moreover, its magneto-optical properties could be an interesting way to unify AOS with current-driven domain walls motion as shown in Pt/Co/Gd racetracks[41].

1.4 This Thesis

In the thesis, we explore the many properties and possibilities that offers the TM-RE alloy GdFeCo by focusing on the current-induced magnetization switching and domain-wall driving. The main objective of this work is to investigate the properties of a GdFeCo magnetic bilayer where both layer are antiferromagnetically coupled by an interplaced spacer in a goal to achieve high efficient current control of the magnetization and high domain-wall velocities.

Such integration of soft ferrimagnets in multilayers samples requires some preliminary studies. This is the reason why chapter 2 is first dedicated to the study of full thin films of single GdFeCo layer deposited by magnetron sputtering. We have investigated the fundamental magnetics properties as a function of the composition of the alloy and the nature of the adjacent layers. Series of samples have been grown and a systematic study has been conducted using Kerr magnetometry. The investigations have been completed with some other techniques such as Transmission Electron Microscopy or X-Ray Diffraction. The results suggest a great dependency of the total magnetic moment, the temperature of magnetic compensation and the PMA of the GdFeCo with the interfaces.

Following these initial results, in chapter 3, the ferrimagnet has been integrated in bilayer stacks and we have shown that it is possible to obtain GdFeCo-based synthetic antiferromagnet. We have characterized the GdFeCo/Ir/GdFeCo samples as in the previous chapter. We also have demonstrated different new features for synthetic antiferromagnet using the unique properties of this alloy.

In chapter 4, the samples have been patterned and micro-devices have been fabricated in order to perform magneto-transport measurements. We have injected micro-second pulses in Ta/Cu/GdFeCo/Ir/Pt and Ta/Ir/GdFeCo/Cu/Pt samples. The typical reversal of the magnetization by standard SOT has been observed but also in the absence of external field. We have shown in our samples the interplay between spin-transfer torque and current-induced magnetic fields.

Finally, in chapter 5, we present our first results on the domain-wall propagation in our samples. Even if strongly affected by Oersted fields, this study has given us first hints and possibilities to be explored as a function of the numerous interaction and parameters that can be tuned especially in synthetic antiferromagnet.

Chapter 2

Dependence of magnetic properties in GdFeCo single layers on the composition and on the nature of the interfaces

In the previous chapter, we have seen the particularities of the GdFeCo. For this thesis, we focused on very thin films of 5 nm thick of this alloy with the objective to favor SOT over the STT. Thus, we can not consider at first glance that the behavior of the material is dominated by bulk properties and the samples have to be sensitive to the interfaces. As seen before, the competition between the demagnetizing field and the anisotropy is the essential condition to maintain the magnetization perpendicular to the film plane. Since the objective is to integrate GdFeCo thin films in different kind of stacks, it is necessary to take an interest in a preliminary study of the effect of the interfaces on the magnetic properties of the ferrimagnet.

2.1 Thin film deposition

Magnetron sputtering is a common, simple and versatile way to deposit materials with a good ability to control thicknesses and the growth rates down to the sub-nanometer regime. This technique allows to deposit either single material or alloys. The principle is shown in figure 2.1 and is the following: an ultra-high vacuum (UHV) chamber is filled with pure argon gas. Then, a large potential is applied to a specific material disk called

a target. The argon atmosphere is ionized by pre-existing free electrons and Ar^+ ions are accelerated during the discharge to the target. When argon ions hit the atoms that make up the target, they are knocked out to the substrate by transfer of momentum. Moreover, the collision also emits secondary electrons. The stray field coming from the magnetrons improves efficiently the time of the electrons in the plasma via helical paths and increases the probability of ion collisions. The plasma is then well sustained at lower argon pressure giving a higher deposition rate and confining the ionization near the target.

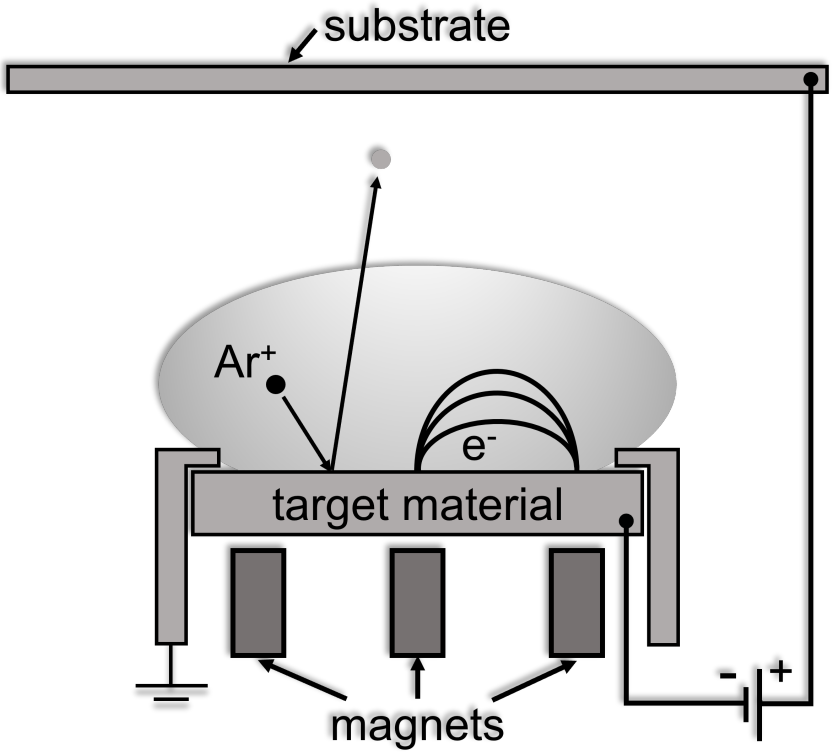

Figure 2.1: Schematic of sputter deposition

A huge part of the thesis project has been dedicated to the growth of series of samples of GdFeCo thin films using magnetron sputtering system ATC-Orion 8 by AJA International Inc. This system consists in two chambers, the load-lock chamber to insert up to 6 substrates and the 8 targets deposition chamber. Each target can be used either for DC or RF sputtering. The interest of RF sputtering is the deposition of insulating materials but it can also be used to deposit at lower rates, which is useful in the case of GdFeCo since the composition in cobalt is only about 8%. The base pressure of the sputter chamber after a bake out is less than 4×10^{-8} mbar and during a deposition, the pressure is equal to 3×10^{-3} mbar.

2.2 Magnetic characterization

2.2.1 MOKE magnetometry

Our sputter tool allows us to deposit quickly series of samples and to vary the composition and the interfaces resulting in different properties. The magneto-optical Kerr effect (MOKE) is more sensitive than classic magnetometry such as SQUID (superconducting quantum interference device) or VSM (vibrating-sample magnetometer) allowing us to measure very thin samples. Moreover, we minimize the signal coming from the magnetic response of the substrate. Even if it does not permit to get the value of the magnetization, it is also the fastest and most versatile way to locally probe the magnetism. It has the huge advantage to give essential information (perpendicular or in-plane magnetization, coercive field, saturation field or even the nucleation behavior) very quickly. Therefore, MOKE is the preferred technique to measure the magnetic properties of many series of samples, especially of materials with high magneto-optical effects such as GdFeCo.

The principle of magneto-optical techniques is the rotation of the polarization plane of the light after the reflection (Kerr effect) or the transmission through a magnetic sample (Faraday effect)[42]. The linearly polarized light can be seen as a superposition of two circularly polarized waves with opposite helicities According to the standard electromagnetism in anistropic media[43], the complex index of refraction is different for the left and right circularly polarization and upon reflection, the two components propagates differently. This results in a rotation of the polarization plane of a certain angle and the light acquires a finite ellipticity that are proportional to the magnetization that arises from the sample.

The MOKE laser setup (fig.2.2) consists in a helium neon laser that emits a light beam which is linearly s-polarized through a polarizer. Then, the beam reflected by the magnetic sample, goes through a photo-elastic modulator (PEM) whose axis of vibration is parallel to the optic table and through a second polarizer called analyzer at 45° with respect of the PEM axis. A photodetector is placed at the end of the optical path and the signal is sent to a lock-in amplifier whose reference frequency is the PEM frequency, 50 kHz. In order to have the Kerr rotation given by the second harmonic signal, the PEM modulation amplitude is optimized and set to 3.05. The output signal of the lock-in is defined to one phase and thus the sign of the signal is arbitrary. But, in our case, the sign is relevant since we probe essentially the TM at 633 nm[44], the wavelength of the laser, and GdFeCo can be either Gd-rich or CoFe-rich. Then, the phase is calibrated with a Co/Pt sample which has the same Kerr rotation sign as the alloy. The Kerr sensitivity depends on the geometry of the setup and the

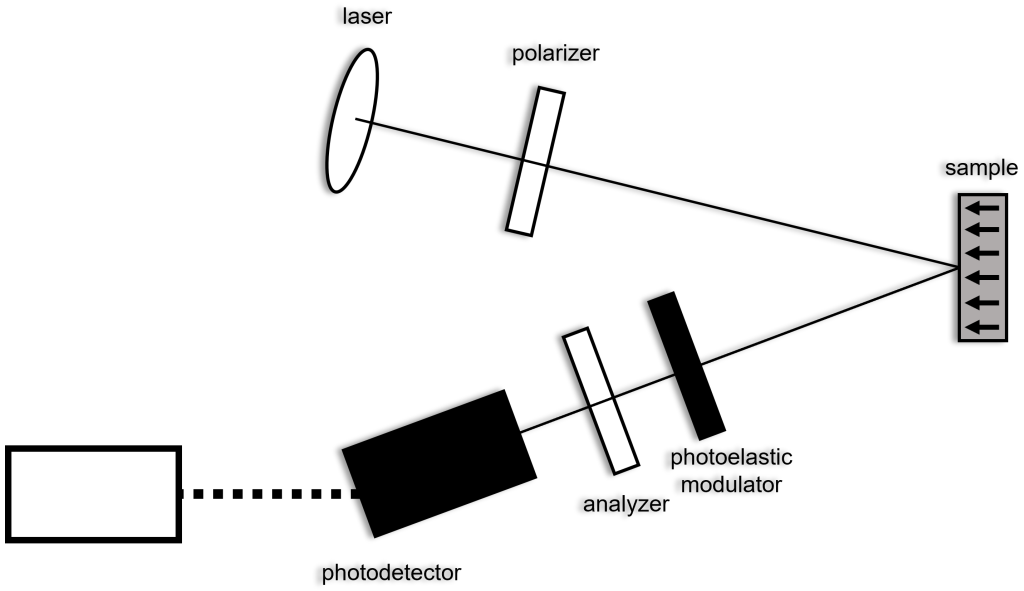

Figure 2.2: Schematic of the polar MOKE magnetometry setup

magnetic anisotropy of the sample. For instance, in our case with PMA, the Kerr signal from the perpendicular component of the magnetization is maximum with the plane of incidence parallel to the thin film normal. This geometry is called polar MOKE.

2.2.2 Kerr microscopy

The Kerr effect can also be used for wide-field-of-view observations as MOKE microscopy which allows to image magnetic domains, their nucleation and their propagation down to the micrometer scale. One major limit of this technique is the Kerr contrast that is very low, especially at high magnification because of the greatly reduced quantity of light. However, this problem can be mostly compensated by real-time processing and Kerr microscopy is really limited by the diffraction limit.

If the principle and the setup of the Kerr microscope are obviously really similar to the Kerr laser setup, imaging magnetic domains requires some adjustments. The ray diagram of our Evico-magnetics Kerr microscope is shown in figure 2.3. Light comes from a white LED and is focused by a collector (Fresnel lens) onto the plane of the aperture slit. This aperture allows to select the angle of incidence of the light and thus the Kerr sensitivity to the different components of the magnetization. The beam is then collimated by a lens and goes through the field diagram that determines which part of the surface is illuminated before being linearly polarized by a polarizer. An other lens can be placed to change the magnification before that the light is focused

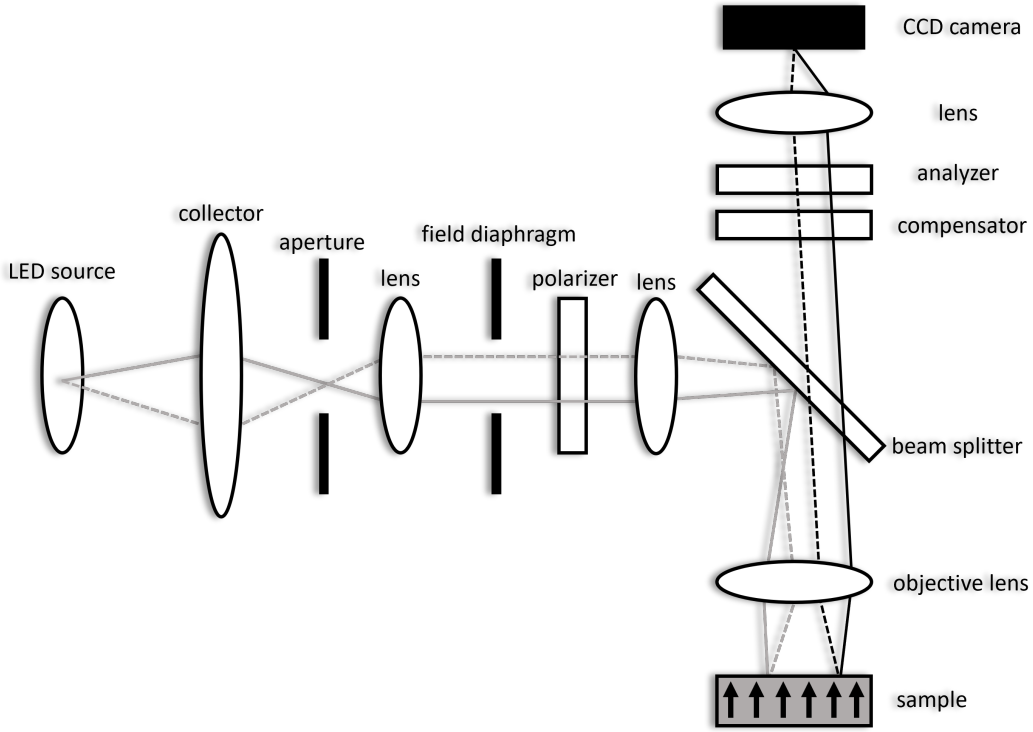

Figure 2.3: Schematic and ray paths of the Kerr microscope setup

on the surface sample by the objective. The reflected light is directed towards a CCD camera but first a compensator converts elliptical light into a linear wave and a analyzer extinguishes more or less the light depending on the Kerr rotation, giving the contrast and different intensity levels.

As explained before, the wide-field Kerr contrast is quite low and real-time processing solves this issue. The idea is to save an average image of the sample that we call background and it is then subtracted to each frame from the live feed. The resulting image depicts only the changes from the initial state allowing to see the nucleation sites or the displacement of domain walls either in full films or lithographed structures but if a magnetic domain is already there, it is included in the background and thus subtracted. In figure 2.4 is presented some examples of Kerr microscopy images with different magnetic structures. As a result of the competition between the different interactions, the magnetic configuration can be a single domain propagating along the film plane (a) or it can break into multi-domains of different shapes and sizes ((b) and (c)). Finally, the Kerr microscope can also image magnetic micrometer devices such as Hall crosses (d).

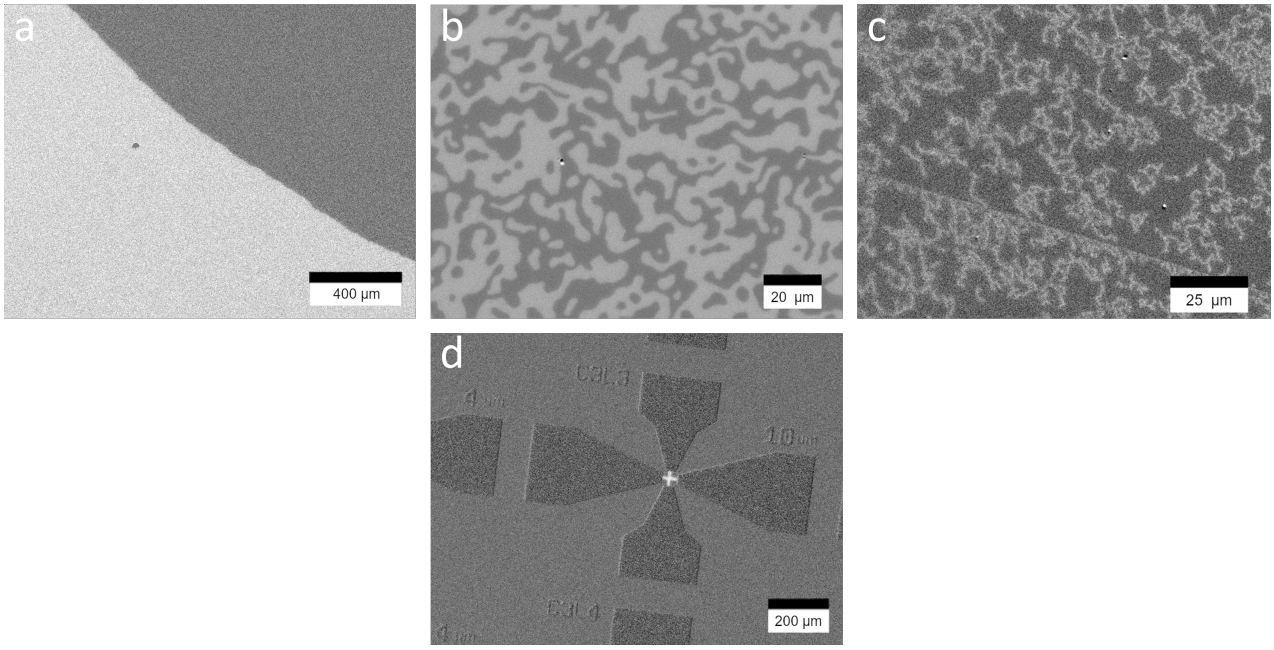

Figure 2.4: Different samples observed with MOKE microscope. (a) Si/SiO/Ta/Cu/$Gd_{24.3}$FeCo/Ir/Pt. (b) $[Co_{79.1}Dy_{20.9}]\times3$. (c) Maze-like magnetic domains in CoHo. (d) 10 μm Hall cross of GdFeCo

2.3 Study on composition and interfaces

2.3.1 Samples

For the GdFeCo, we have at our disposal a highly pure target for each element which allows us to have an excellent control of the composition. The alloy is deposited on silicon substrates with a 100 nm thick thermally grown SiO_2 layer essential to avoid leaks of current into the substrates during transport measurements. After cutting and blown dry with N_2, the surface of the substrate, before each deposition, is etched by a RF Ar plasma of 50 W at a pressure of 1.10^{-2} mbar during 5 minutes. In order to make the thin films as uniform as possible, the sample holder is rotated at several dozen of revolutions per minute. We deposited series of 5 nm thick $Gd_x(Fe_{90}Co_{10})_{100-x}$ (in atomic composition) single layers integrated in different multilayers. A buffer of tantalum is always sputtered before the magnetic layer and a platinum layer is added over as a capping layer. The composition is varied systematically in a range of 22% < x < 33% and we studied different interfaces M/GdFeCo/N with M or N = Cu, Pt, Ta, Ir. For each sample, we measured their magnetic hysteresis loop at room temperature with the Kerr laser setup. From the loops, we know if the magnetization is out-of-plane (OOP) or lies in the film plane and we also have the value of the coercive field or the saturation field. The former is expected to diverge at the magnetic compensation because the net magnetization is zero. From the

sign of the loop, we can deduce which sub-lattice dominates the magnetization of the sample.

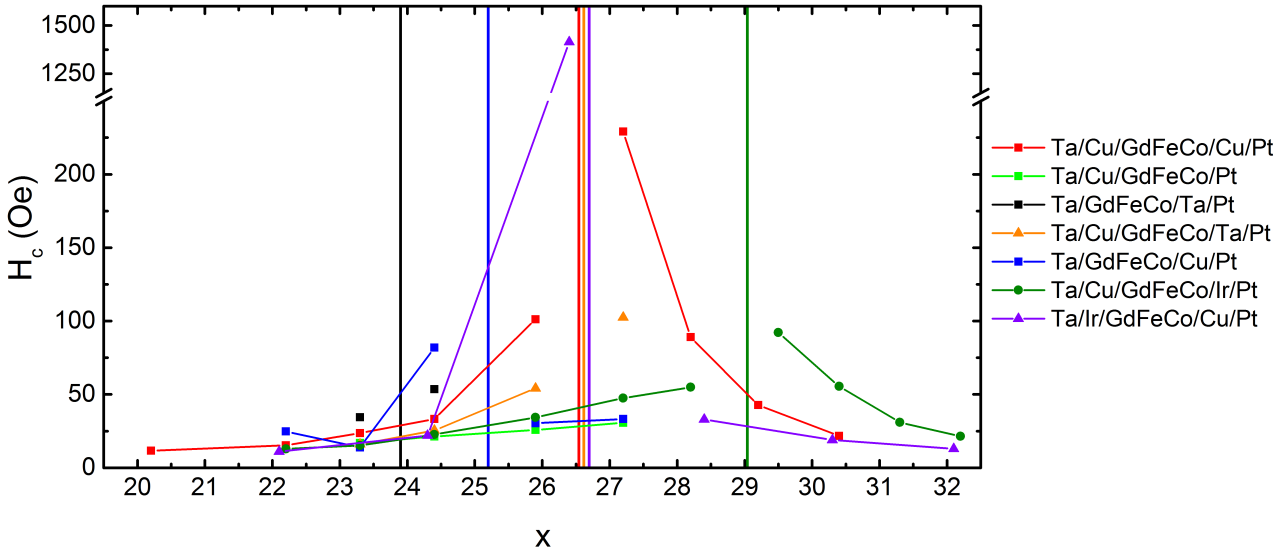

Figure 2.5: Coercive field as a function of the composition in Gd for GdFeCo layers with different interfaces

In figure 2.5 is presented the summary of the study. Each point represents the coercive field of a sample that exhibits PMA. Samples with in-plane magnetization in the range 22% < x < 33% are not shown on the graph. The vertical lines represent the change between CoFe-rich samples and Gd-rich samples, respectively on the left and right side of the lines, for each set of interfaces. These lines thus represent the approximate composition of compensation and it is clear that the coercive field diverges at the vicinity of this singularity.

2.3.2 Effects on the perpendicular magnetic anisotropy

The first thing that we can notice in the figure 2.5 is that all the samples do not exhibit PMA on the same range of composition. For instance, with Ta at the bottom and Pt at the bottom, in the considered range, we haven't been able to obtain frank perpendicular anisotropy (fig.2.6). For 22.2% < x < 23.3%, we obtain typical in-plane loops. However, we can see as we get closer to the magnetic compensation, the saturation field decreases until the shape of the loops changes to a curvy signature characteristic of multi-domains states such as the one presented in figure 2.4 (b). At x = 29.2%, the magnetization goes back to the plane but the sign of the loop changes indicating that we passed the composition of magnetic compensation.

For Ta interfaces (fig.2.5 ■ (black square)) under and over the ferrimagnet, the samples are perpendicular

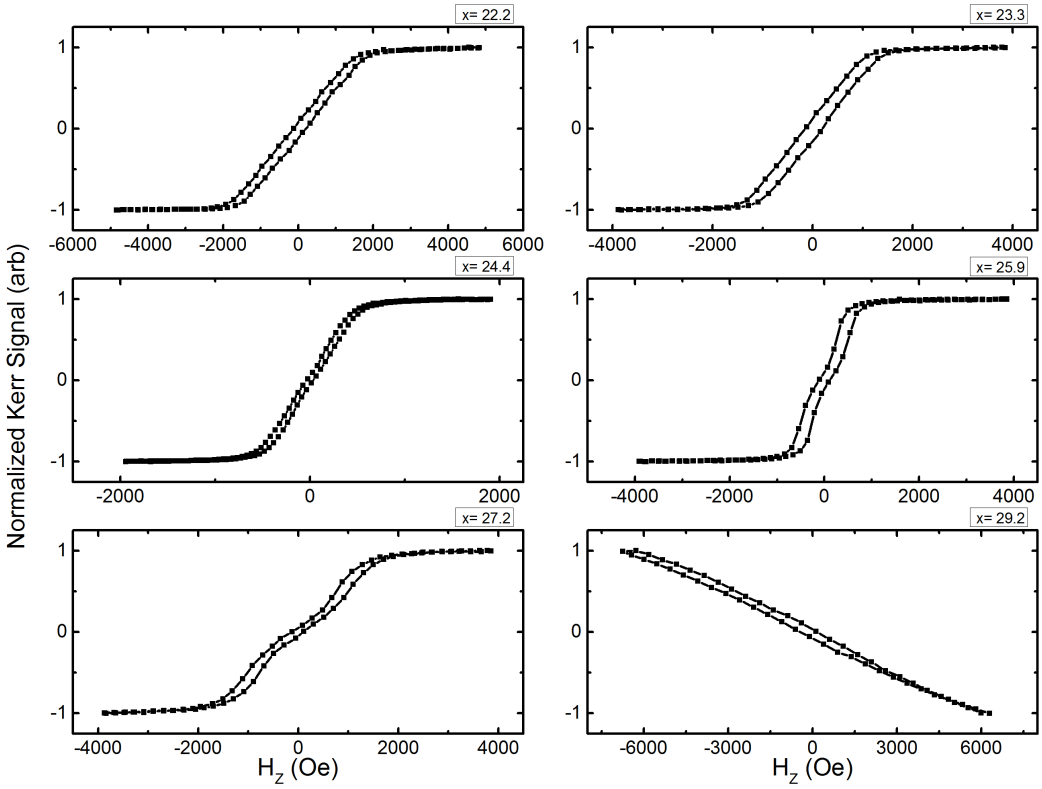

Figure 2.6: Hysteresis loops for Ta/GdFeCo/Pt samples at different compositions measured by Kerr magnetomery in polar geometry

only for two different compositions on both sides of the composition of compensation and the other composition lead to in-plane magnetization in the considered range.

We now focus on the addition of copper layers in the stacks that seems to have a major impact on the magnetic properties of the samples. With two Ta interfaces, the insertion of copper layer between the Ta buffer and the magnetic layer clearly improves the PMA (fig.2.5 ▲ (orange triangle)). For example, at the same nominal composition $Gd_{25.9}Fe_{65.1}Co_9$ without copper seed layer, the magnetization is in-plane but we obtain a typical OOP square hysteresis loop when the Cu layer is added (fig.2.7).

For Ta/Cu/GdFeCo/Pt or Ta/GdFeCo/Cu/Pt respectively (■ green square and ■ blue square in fig.2.5), several samples exhibit PMA on the studied range. Compared to the initial stack Ta/GdFeCo/Pt, it is clear that the copper either under or over the ferrimagnet stabilizes the perpendicular magnetization. For the composition x = 22.2%, it is to be noted that the magnetization of one Ta/Cu/GdFeCo/Pt sample remains in the film plane.

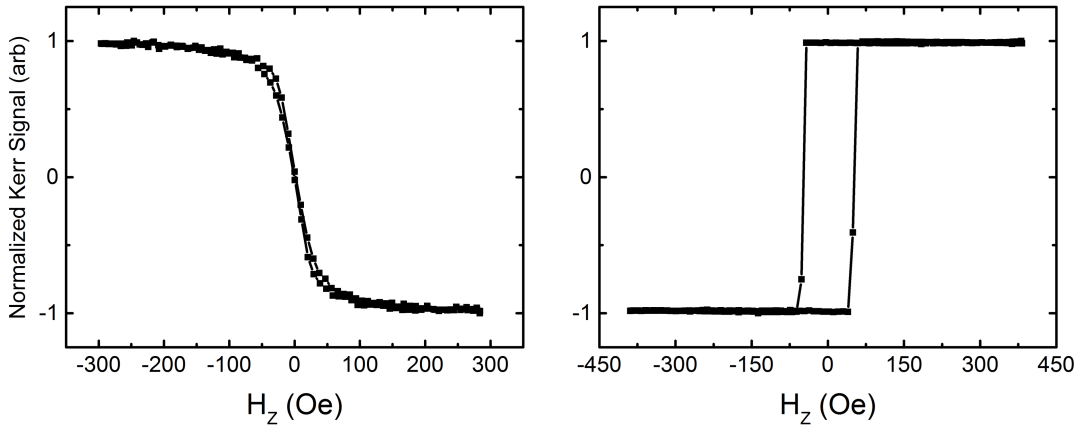

Figure 2.7: Hysteresis loops for Ta/$Gd_{25.9}Fe_{65.1}Co_9$/Ta (left) and for Ta/Cu/$Gd_{25.9}Fe_{65.1}Co_9$/Ta (right)

However, the PMA is further improved when the GdFeCo is surrounded by Cu layers. On a very large range of composition from x = 20.2% to x = 30.4%, PMA is maintained (fig.2.8). For extreme compositions far from the compensation, we still measure square Kerr loops for these samples even with very low coercive fields indicating higher magnetization and limit behavior for OOP anisotropy. From x = 20.2% to x = 25.9%, the magnetization is dominated by the FeCo sub-lattice. As we get closer to the compensation, the coercive field increases as expected and diverges around x = 26.6%. Then, the magnetization is still OOP but is dominated by the Gd sub-lattice as shown by the change of sign of the loops.

When one of the copper interface is replaced by an iridium one, either at the top or the bottom (respectively ● green circle and ▲ purple triangle in fig.2.5), the effect on PMA is quite similar and no in-plane samples have been observed.

2.3.3 Effects on the composition of compensation

The interfaces not only play a role on maintaining magnetization perpendicular but we also show that the composition at which the magnetic compensation occurs, changes depending on the layers under and over the TE-RM layer. In this study, the shift of composition of compensation goes up to $\Delta x \approx 3\%$. If we consider the compensation composition the least rich in Gd for Ta/GdFeCo/Ta, we observe two kind of shifts. First, we need to add more Gd to obtain the compensation when a copper layer is added over the buffer of Ta and the same behavior is seen for a copper layer on the top of the ferrimagnet. Second, the maximum shift occurs with a copper seed layer and when the GdFeCo is directly in contact with Ir and/or Pt.

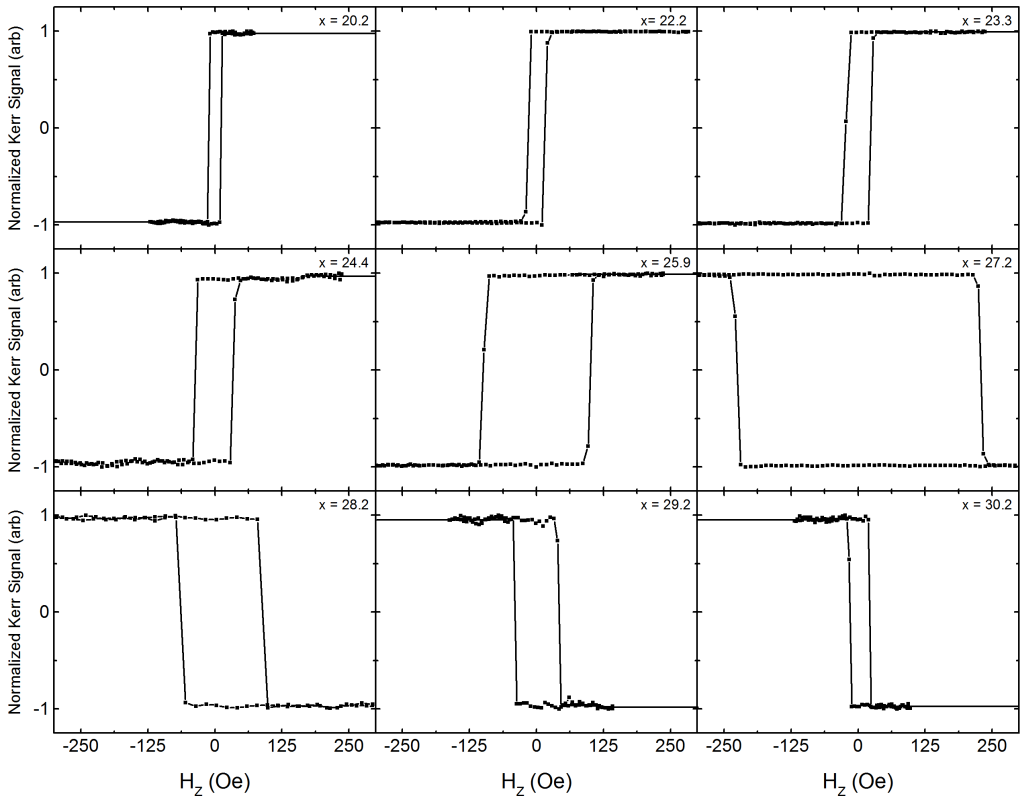

Figure 2.8: Hysteresis loops for Ta/Cu/GdFeCo/Cu/Pt samples at different compositions measured by Kerr magnetomery

2.4 Investigation and discussion

Since the origin of the anisotropy in the amorphous ferrimagnets still does not reach a consensus, we are still trying to understand how the interfaces can play a role in such important differences of PMA for the same nominal layers. However some ideas can be investigated such as the role of amorphous Ta layer compared to crystallized copper or even the well-known Pt polarization in contact with magnetic impurities or layers.

2.4.1 Polarization of the interfaces

Because the exchange interaction between conduction electrons is large in platinum, it is almost ferromagnetic and by consequence has a large susceptibility. Indeed, it exhibits giant magnetic moment induced by magnetic

impurities[45]. The proximity with ferromagnetic layers is known to induce ferromagnetic order due to long-range oscillatory indirect magnetic exchange interaction called the Ruderman-Kittel-Kasuya-Yosida (RKKY). Therefore, a magnetization is induced in 5d Pt either by the Co/Pt or the Fe/Pt interfaces[46–50]. At the Fe/Pt interface, the induced magnetic moment on the Pt atoms has been estimated to 0.3 μ_B[51] and at Co/Pt interface, 0.14 μ_B per Pt atom[52,53]. For Ta/Pt/Co, the moment can go down to 0.05 μ_B with the increase of the thickness of the Ta buffer layer[53]. Moreover, moments are also induced at the TM/Ir interfaces . The polarization of the Ir interface atoms is estimated at 0.3 μ_B with Co[54] and 0.2 μ_B with Fe[55]. Finally, the polarization of the d-band of the copper atoms is also reported either in Co/Cu multilayers of 0.05 μ_B[56,57] or in Fe/Cu multilayers up to 0.09 μ_B[57]. The induced moments in FeCu alloys and in CoCu alloys are similar and around 0.13 μ_B[56–58].

For our ferrimagnet, we have roughly 70% of Fe and 10% of Co so we consider the polarization of the copper, the iridium and the platinum by the FeCo sub-lattice. Therefore, we can explain the different shifts in the composition of compensation. When Pt or Ir is directly on the top of the GdFeCo grown on a Cu layer, the induced moments are maximum among our studied stacks which means additional moments parallel to the FeCo moment have to be taken in account. It is then needed to add more Gd (x $\approx$ 29%) compared to the other stacks to reach the magnetic compensation point. For Ta/Ir/GdFeCo/Cu/Pt, the compensation is at x $\approx$ 26.6% which can be explained by a lower induced moment of the Ir/GdFeCo interface than the GdFeCo/Ir one. For the other stacks, the moments which are needed to be added, come from the copper and are by consequence also lower. For Ta interfaces, there is no polarization which explains that less Gd is needed (x $\approx$ 23.9%).

The polarization of the interfaces implies an increase of the saturation magnetization. This effect explains the variation of the temperature of magnetic compensation. By consequence, the demagnetizing field also increases and this could be at the origin of the in-plane magnetization for Ta/Cu/$Gd_{22.2}$FeCo/Pt whereas its OOP for Ta/$Gd_{22.2}$FeCo/Cu/Pt. However, we cannot explain other major changes especially in the case of tantalum at each interface where the PMA is particularly difficult to obtain. We have to consider that the interfaces play a role in the intrinsic anisotropy K.

2.4.2 Effect of a crystallized seed layer

X-Ray Diffraction

In the previous part, we have seen a possible explanation for the differences in the composition of compensation that could also have an effect on the PMA. Other possible reasons could be the texture of the seed layer or the mixing of the interfaces.

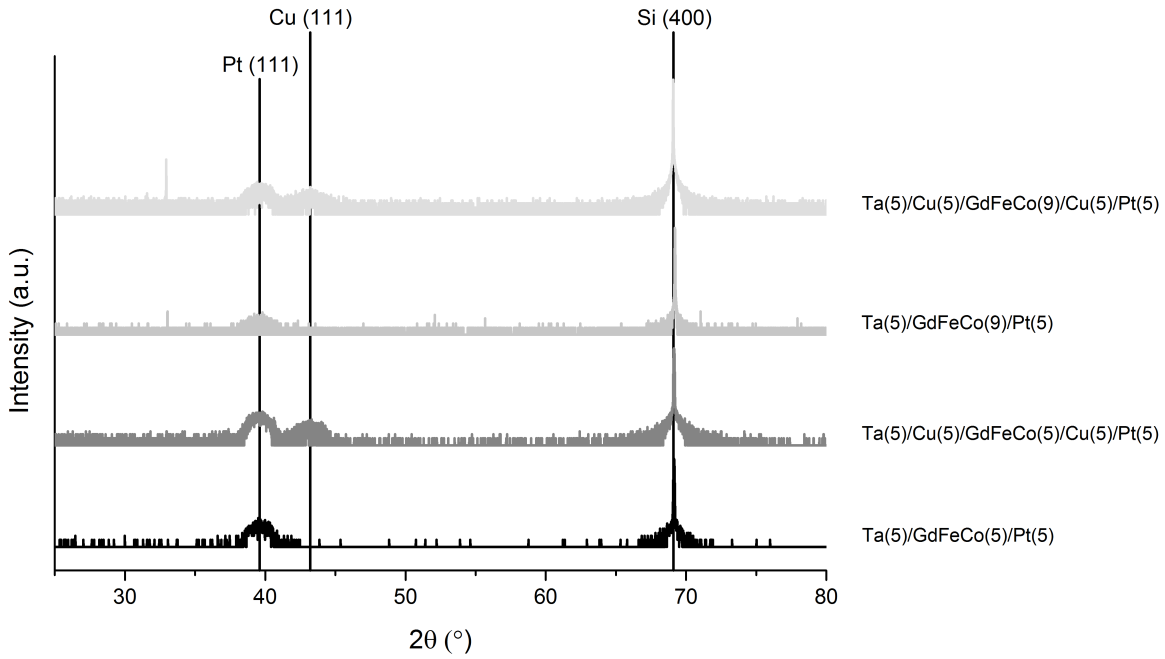

Figure 2.9: X-ray thin films diffractograms for GdFeCo samples of 5 nm and 9 nm with or without a Cu seed layer

After a few nanometers, the copper or the iridium acquire a (111) surface when deposited over the Ta that is amorphous. We have measured different samples by X-Ray diffraction to investigate the effect of such seed layers. We have tried to see any difference between samples with Cu layer or not for two different thicknesses (5nm and 9nm). On these samples, we can detect the diffraction peak of Si(100) which comes from our substrate, and also the peak for Pt(111) which is our capping layer (fig.2.9). When a Cu layer is added, the peak of Cu(111) appears but we cannot see any other difference. The thickness has been increase to 9 nm in order to increase the signal from the GdFeCo and to try to see if the copper induces any change in the ferrimagnet structure but no change has been noticed.

Dependence on the Cu layer thickness

If we consider the stack Ta(5 nm)/Cu(y nm)/$Gd_{23.4}$FeCo(5 nm)/Pt(5 nm) varying y from 1 nm to 4 nm, we obtain interesting results presented in figure 2.10. Indeed, the thickness seems to be directly related to the PMA. For 1 nm of Cu between the Ta and the GdFeCo, the magnetization lies clearly in the plane of the sample with a saturation field around 3200 Oe. For 2 nm, the magnetization remains in-plane but the saturation field is reduced around 2400 Oe. At 3 nm of Cu, the cycle seems to open up and the saturation field falls to 1200 Oe. Finally at 4 nm, the magnetization leaves the plane, the cycle is open and is typical of small magnetic structures such as bubbles or skyrmions. As seen before, for 5 nm, the magnetization is perfectly perpendicular to the plane.

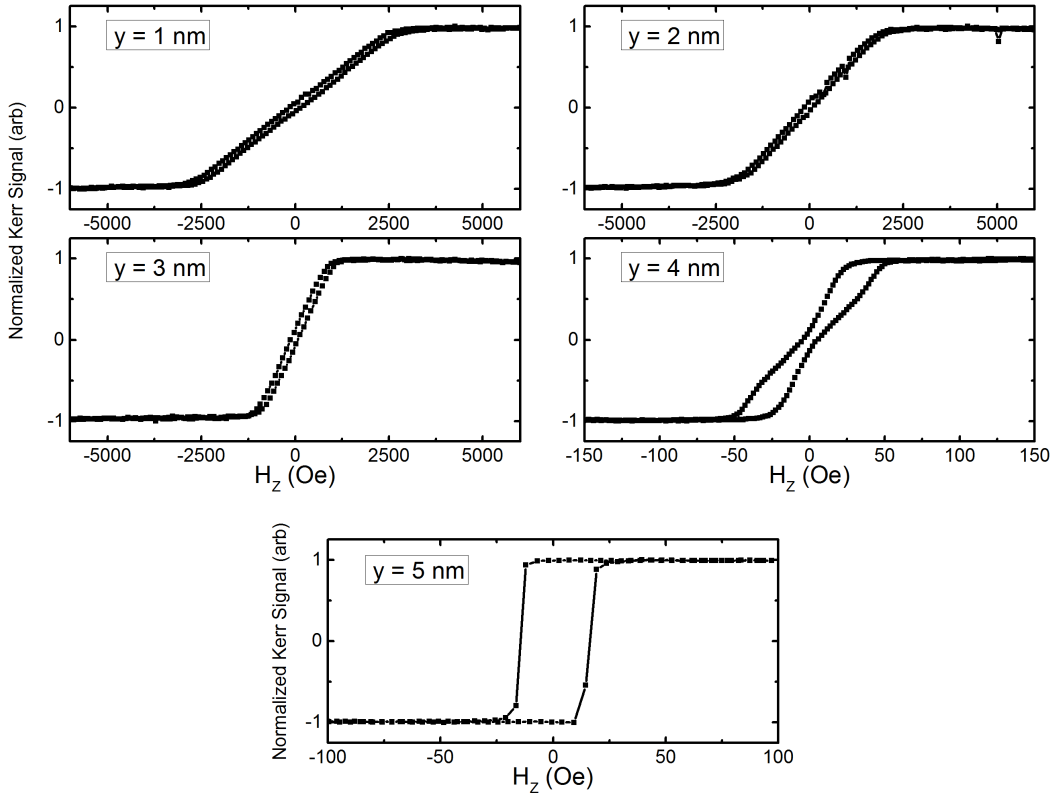

Figure 2.10: Hysteresis loops for Ta(5 nm)/Cu(y nm)/$Gd_{23.4}$FeCo(5 nm)/Pt(5 nm) with 1 nm < y < 5 nm.

Experimentally, the dependence of the PMA with the thickness of the Cu layer is clear but from these measurements, GdFeCo seems to remain amorphous. A local analysis is necessary to go deep into the details

of the local crystallographic structure.

Transmission Electron Microscopy

Therefore, transmission electron microscopy (TEM) investigations were carried out using a JEM - ARM 200F Cold FEG TEM/STEM operating at 200 kV and equipped with a spherical aberration (Cs) probe and image correctors (point resolution 0.12 nm in TEM mode and 0.078 nm in STEM mode). The samples are prepared by Focused Ion Beam (FIB) to mill a cross-section of them.

We first observed a Ta/Cu/$Gd_{24.3}$FeCo/Ir/Pt sample with Transmission Electron Microscopy Bright Field (TEM BF) and High-Resolution Transmission Electron Microscopy (HRTEM) presented in figure 2.11 (top and bottom respectively). The amorphous character of Ta and GdFeCo is confirmed. Indeed, the fast Fourier transform (FFT) of the GdFeCo layer shows the amorphous typical halo ring pattern. We can see the crystal structure of the Cu with a growth direction along [111] as shown by the reciprocal lattice, even if we can notice some grains. The intermixing and the roughness seems to be more important at the Ta/Cu interface than at the Cu/GdFeCo one. We can add that the interface between the amorphous ferrimagnet and the crystallized iridium is not well defined suggesting intermixing as well.

To complete the imaging of the stack, we performed Scanning Transmission Electron Microscopy spectrum imaging (STEM SI) which consists in a chemical analysis by mapping the different elements using Electron Energy Loss Spectroscopy (EELS). The elements map of a region of Ta/Cu/$Gd_{24.3}$FeCo/Ir/Pt is shown in figure 2.12. As it could be seen on the micrographs, when the bottom layer is amorphous, the interface with the top layer is mixed. For instance, the signals from the Ta and Cu are overlapped at the interface, as well as the signals at the GdFeCo/Ir interface where we can see a large gradient for iron, gadolinium and iridium. On the other hand, the overlapping at the Cu/GdFeCo is limited and the interface is well defined.

We also investigated the reverse order stack: Ta/Ir/$Gd_{24.3}$FeCo/Cu/Pt. There is no major difference in this stack (fig.2.13) GdFeCo is still clearly amorphous, none induced texture can be seen and the FFT is again a halo ring. Iridium crystallized too over tantalum in the [111] direction of its fcc unit cell. The mixing between Ta and Ir seems to be reduced compared to the Ta/Cu one. The Ir/GdFeCo interface is not as clear as the one with Cu and Ir is a bit diffused but the copper on the top mixes less with the alloy. Overall, the GdFeCo layer is more contained and there is no such gradient as in the previous stack.

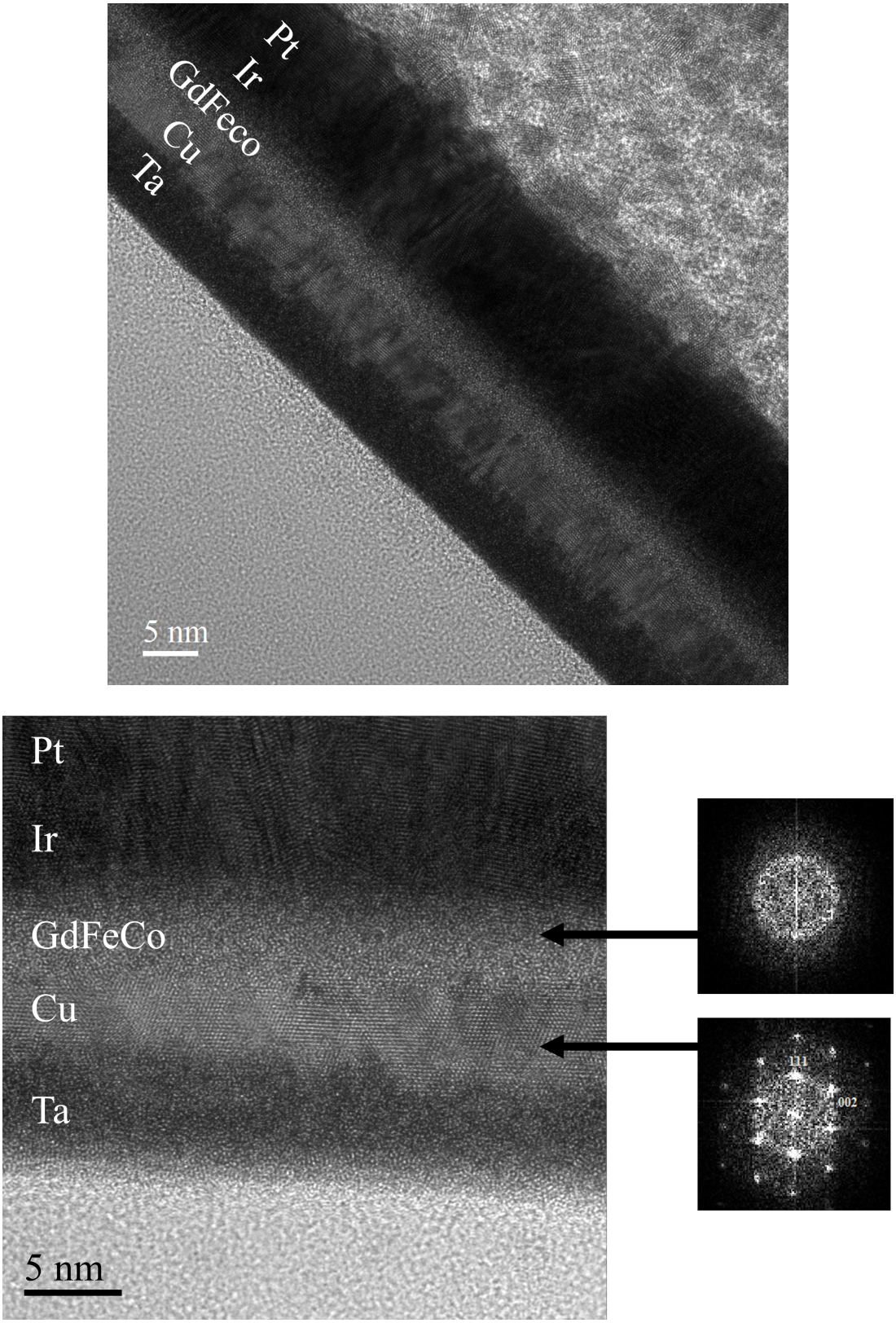

Figure 2.11: (Top) TEM BF micrograph and (bottom) HRTEM micrograph of Ta/Cu/$Gd_{24.3}$FeCo/Ir/Pt with the FFT of the GdFeCo and Cu layers

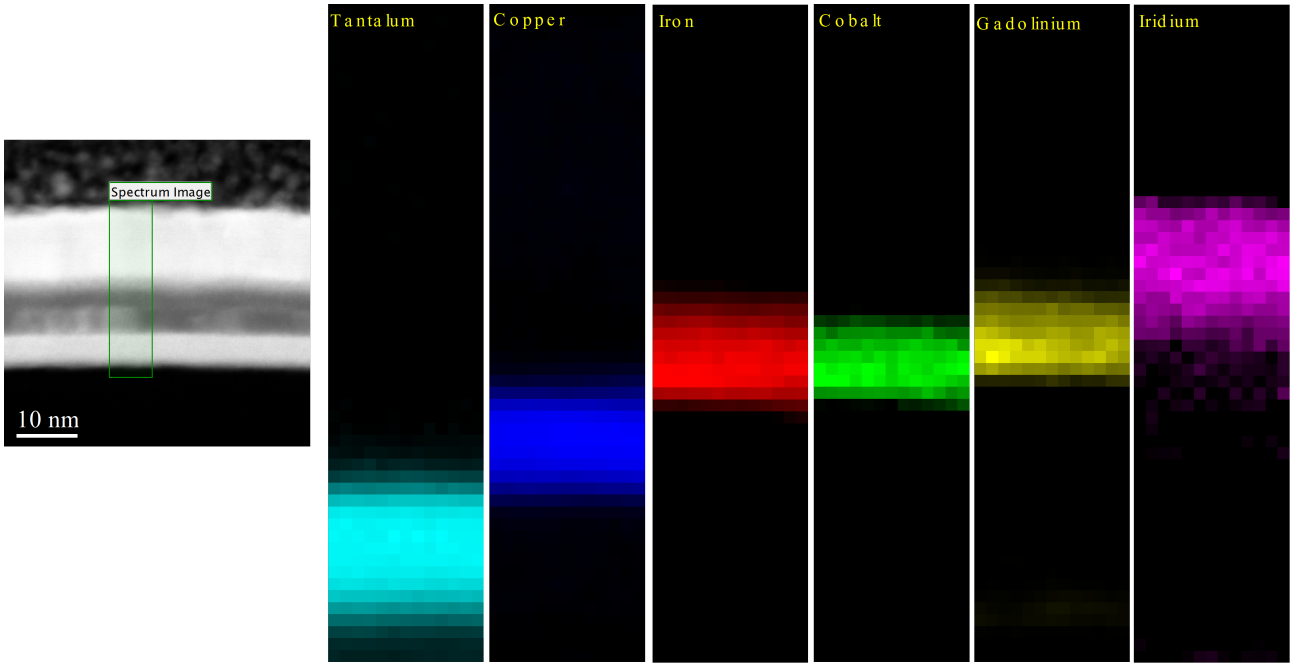

Figure 2.12: EELS spectrum for the different elements of Ta/Cu/$Gd_{24.3}$FeCo/Ir/Pt for the scanned region framed in green in the micrograph on the right

Globally, a copper, either under or over, ensures a clean interface without mixing with the GdFeCo. Concerning the iridium layers, despite its crystal structure, it turns out that this element spreads more at the interfaces. Despite these observations, an interface with Cu or Ir seems to be preferable that one with Ta. Since there is no visible change in the GdFeCo layer, it is complicated to conclude on the benefits of a particular interface however we can assume that a smoother interface improves the quality and preserves the correct composition of the film.

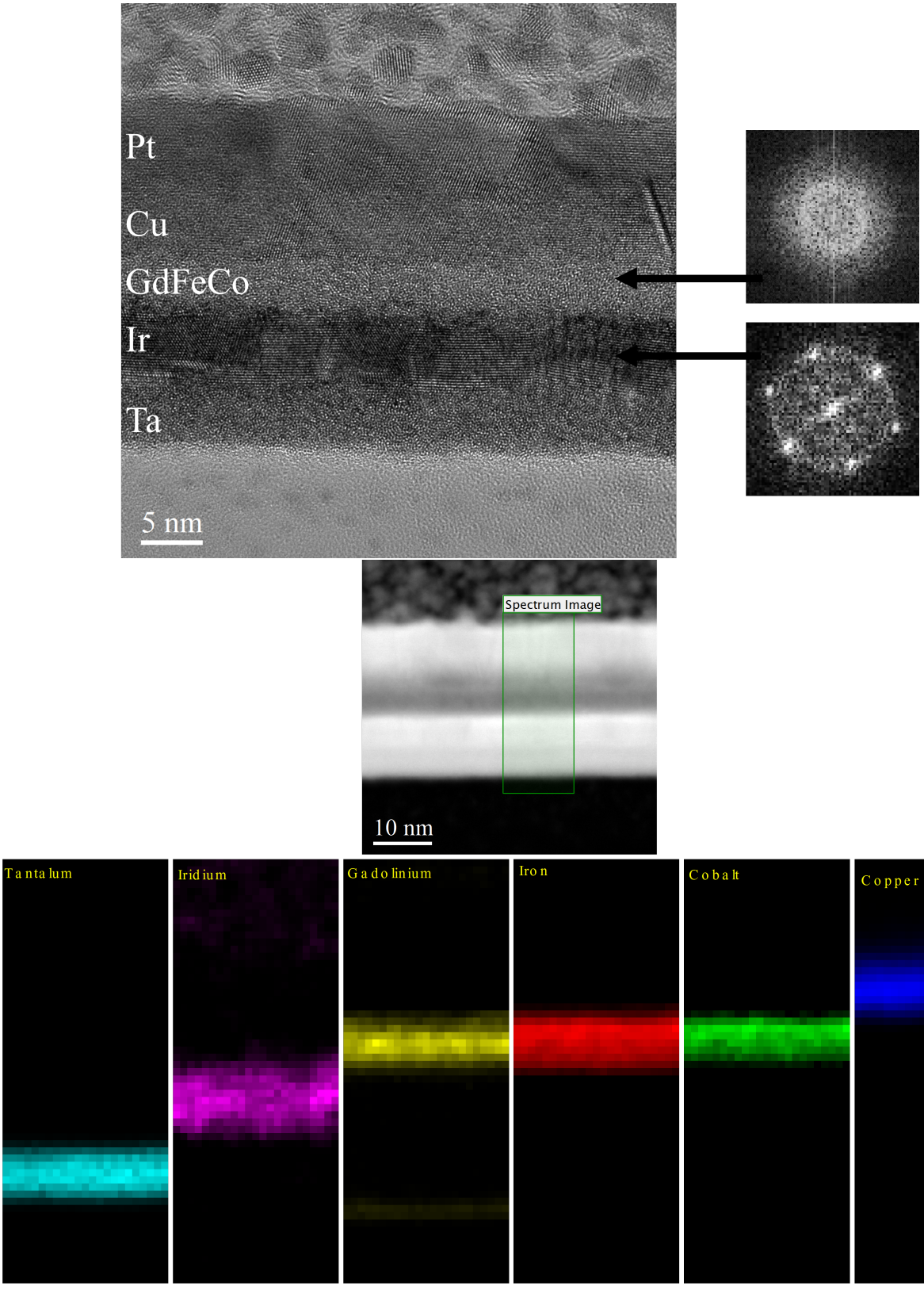

Figure 2.13: (Top) HRTEM micrograph of Ta/Ir/$Gd_{24.3}$FeCo/Cu/Pt with the FFT of the GdFeCo and Ir layers. (Bottom) EELS spectrum for the different elements of Ta/Ir/$Gd_{24.3}$FeCo/Ir/Pt for the scanned region framed in green in the micrograph

2.5 Conclusion

In this chapter, we have shown that in $Gd_x(Fe_{90}Co_{10})_{1-x}$ ferrimagnetic alloys single layers for x between 22% and 33%, the composition needed to reach the magnetic compensation can be shifted up to 3% as a function of the interfaces. We have found that the main reason is the well-known polarization of the adjacent layers with the iron and the cobalt of our material. This has for direct consequence the increase of the moment in the direction of FeCo of the sample thus the necessity to add more gadolinium in the sample to compensate the net total moment. We have observed that the PMA is also greatly affected by the interfaces. Even if a larger demagnetizing field can explained that the magnetization of the sample far from the compensation falls more easily in the plane, this cannot explain the behavior of all the considered stacks. The anisotropy in RE-TM has a bulk nature and some mechanisms have been observed in the literature such as columnar textures[59], microcrystallinity[60] or magnetic anisotropy or atomic-scale anisotropy[61–63]. Our TEM images have revealed as expected that our GdFeCo layers are truly amorphous and do not show any long-range structural order. Moreover, int the case of Gd the 4f shell has S=7/2 but L=0 and thus the spin-orbit coupling is zero when for instance Dy or Tb exhibit large local magnetic anisotropy due to their spin-orbit coupling[64]. From our work, the origin of the anisotropy is still uncertain but the atomic-scale anisotropy could be investigated.

We have now the rules to tune the magnetism of our ferrimagnet layers and to integrate them in the synthetic antiferromagnet stack. To favor the PMA, we have made the choice to always keep at least one layer of Cu adjacent to the GdFeCo.

Chapter 3

GdFeCo based Synthetic Antiferromagnet (SAF)

After the study in the previous chapter, we have a better idea of the behavior of the ferrimagnet integrated in a stack of different materials. So, for GdFeCo layers having out of plane magnetization, more complex structures have been grown associating two GdFeCo layers. Especially, we grew GdFeCo/Ir/GdFeCo with varying Ir thickness. The interests of synthetic antiferromagnetic structure are multiple. The main idea is to nullify the total magnetization of the sample. Indeed, the demagnetizing field coming from each magnetic domain interacts with its neighbors and limits the density of domains. Thus, it is relevant to reduce the stray field to improve memory devices. Also new devices have been proposed which consist in trains of magnetic domain in a nanowire that can be moved under the effect of an electric current. The domain walls velocity depends directly on the net magnetic moment in SAF structure[65] and high velocities are expected.

3.1 RKKY coupling

As mention before, the RKKY interaction is a long-range oscillatory indirect magnetic exchange interaction predicted by Ruderman and Kittel in 1954[66] and was later completed by Kasuya in 1956[67], and Yosida in 1957[68]. First observed in dilute magnetic alloys, the RKKY interaction is the spin polarization of the conduction electrons at the immediate neighborhood of a magnetic impurity. This polarization decays in an

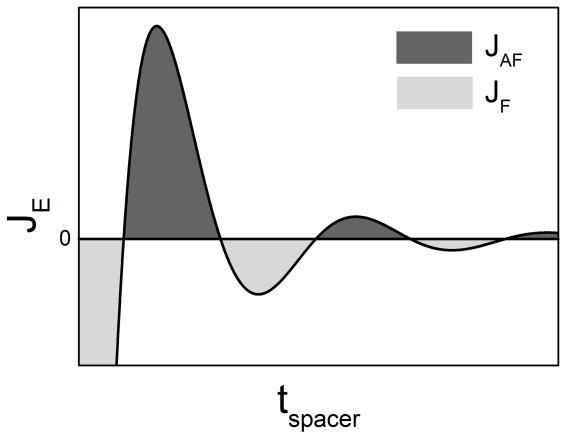

Ti	V	Cr	Mn	Fe	Co	Ni	Cu
No Coupling	9 3 / 0.1 9	7 7 / .24 18		Ferro-Magnet	Ferro-Magnet	Ferro-Magnet	8 3 / 0.3 10
2.89	2.62	2.50	2.24	2.48	2.50	2.49	2.56
Zr	**Nb**	**Mo**	**Tc**	**Ru**	**Rh**	**Pd**	**Ag**
No Coupling	9.5 2.5 / .02 *	5.2 3 / .12 11		3 3 / 5 11	7.9 3 / 1.6 9	No Coupling	No Coupling
3.17	2.86	2.72	2.71	2.65	2.69	2.75	2.89
Hf	**Ta**	**W**	**Re**	**Os**	**Ir**	**Pt**	**Au**
No Coupling	7 2 / .01 *	5.5 3 / .03 *	4.2 3.5 / .41 10		4 3 / 1.85 9	No Coupling	No Coupling
3.13	2.86	2.74	2.74	2.68	2.71	2.77	2.88

Element: A_1 (Å), ΔA_1 (Å), J_1 (erg/cm²), P (Å), r_{ws} (Å)

bcc, complex cubic, fcc, hcp

Figure 3.1: (Left) Evolution of the RKKY exchange coupling constant as a function of the thickness of the considered spacer with J_{AF} the antiferromagnetic and J_F the ferromagnetic coupling. (Right) Periodic table from [46] of A_1 (Å), the spacer-layer thickness of the first antiferromagnetic peak, J_1 (erg/cm^2), the magnitude of the antiferromagnetic exchange-coupling strength at this first peak, ΔA_1 (Å), the range of the first antiferromagnetic region, P (Å), the oscillation period and r_{ws} (Å) the Wigner-Seitz radii

oscillatory manner and for a free-electron gas, the period corresponds to the half Fermi wavelength of the non-magnetic metal, which is typically a couple of atomic spacings. Then, in a similar way, the possibility to couple two ferromagnetic layers by thin non-magnetic transition-metal spacer attracts a huge interest. This leads to a coupling with sign and amplitude that depend on the thickness of the spacer (fig.3.1 (left)) and it can be expressed as a function that takes the form[69]:

$$J_E(t) \approx F(t) = \frac{2k_F t\ cos(2k_F t) - sin(2k_F t)}{(2k_F t)^4} \tag{3.1}$$

with J_E, the exchange integral, t, the thickness of the spacer and k_F, the length of the Fermi vector for the considered metal.

For the case of magnetic layers instead of impurities, the oscillation period, related to the Fermi surface, is much larger and has been widely studied[46,70]. Some typical periods are about 10 Å for Cu and up to 18 Å for Cr (fig.3.1 (right)). For Ir, the spacer that is used in this work, the period of the oscillations is 9 Å, the first antiferromagnetic peak is at t_{Ir} = 4 Å and the second one at t_{Ir} = 13 Å

3.2 GdFeCo/Ir/GdFeCo

3.2.1 FeCo-rich based

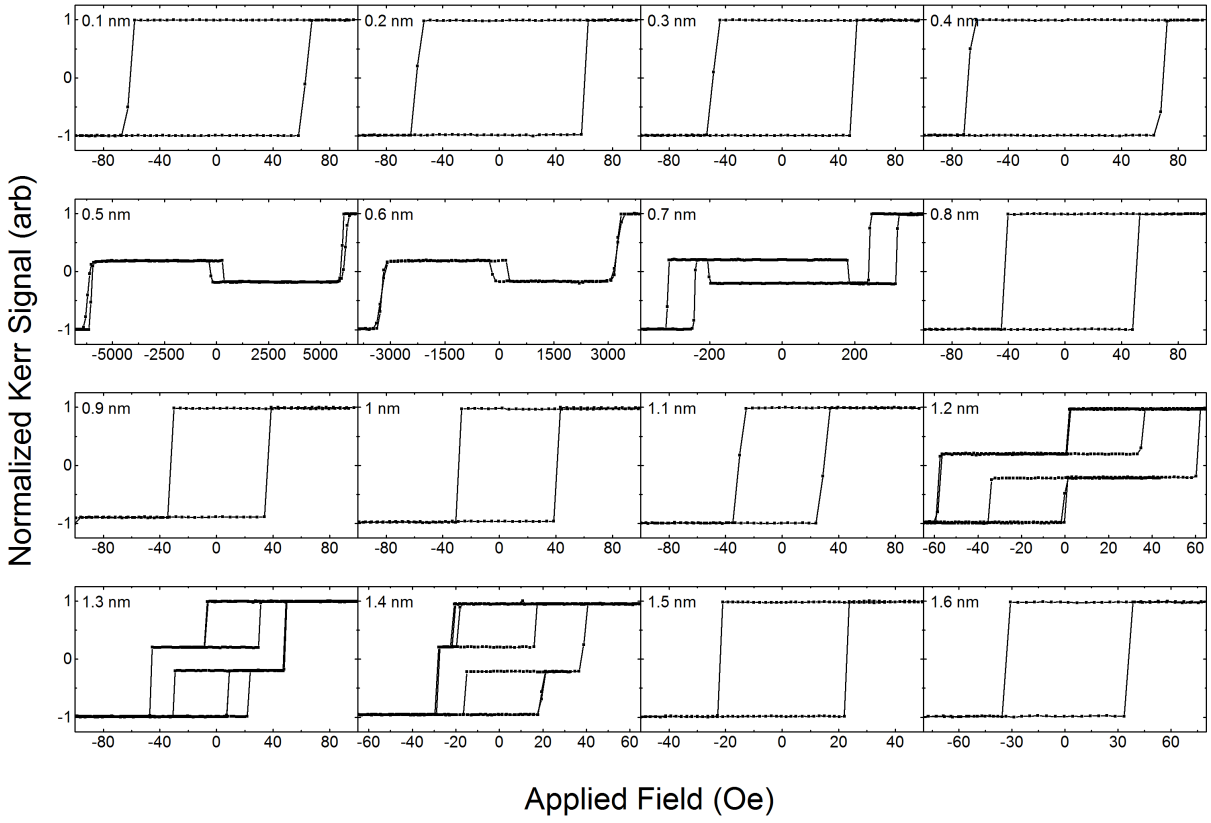

Figure 3.2: Hysteresis loops measured by MOKE for GdFeCo(5 nm)/Ir(x nm)/GdFeCo(5 nm) with 0.1 < x < 1.6

We show that it is possible to couple two GdFeCo ferrimagnetic layers. As for ferromagnetic layers, the coupling depends on the thickness of the Ir layer and varies following the typical oscillation of the RKKY interaction. The coupling is mediated through the Ir spacer between the FeCo sub-lattice of each layer. When the magnetization of both layers is dominated by the FeCo sub-lattice, the antiferromagnetic (ferromagnetic) coupling means that the FeCo moment of one layer is antiparallel (parallel) to the other. In figure 3.2 is presented the Ta(5)/Cu(5)/$Gd_{24.5}$FeCo(5)/Ir(x)/$Gd_{22.2}$FeCo(5)/Cu(5)/Pt(5) hysteresis loops measured by polar MOKE of different stacks with 0.1 nm < x < 1.6 nm. The Cu layers on both sides are there in order to maximize the PMA which is a great couple of interfaces with Ir as shown in chapter 2. We see that between x = 0.1 nm and x =

0.4 nm, we have only a simple square loop revealing a ferromagnetic coupling. Then, for 0.5 nm < x < 0.7, we obtain four levels hysteresis loops. They correspond to the different states of the SAF structure (fig. 3.3): P+ , when the magnetization of both magnetic layers are parallel for a positive field (P- for a negative field), AP+, when layers are anti-parallel with only one layer aligned with the positive field, AP-, which is the equivalent of AP+ for a negative field with the directions of both layers reversed. The layer opposite to the field can be either the top or the bottom one and results of the competition between the Zeeman, the RKKY exchange and the anisotropy and by consequence is the layer with the lower M_S. One has to note that for the AP+ state, we observe a lower Kerr signal than for the AP- state but the magnetization for AP+ is always higher than for AP-. This inversion is due to the difference of contribution to the total Kerr signal of each layer. In our case, the layer with higher Kerr signal is also the one with the lower M_S.

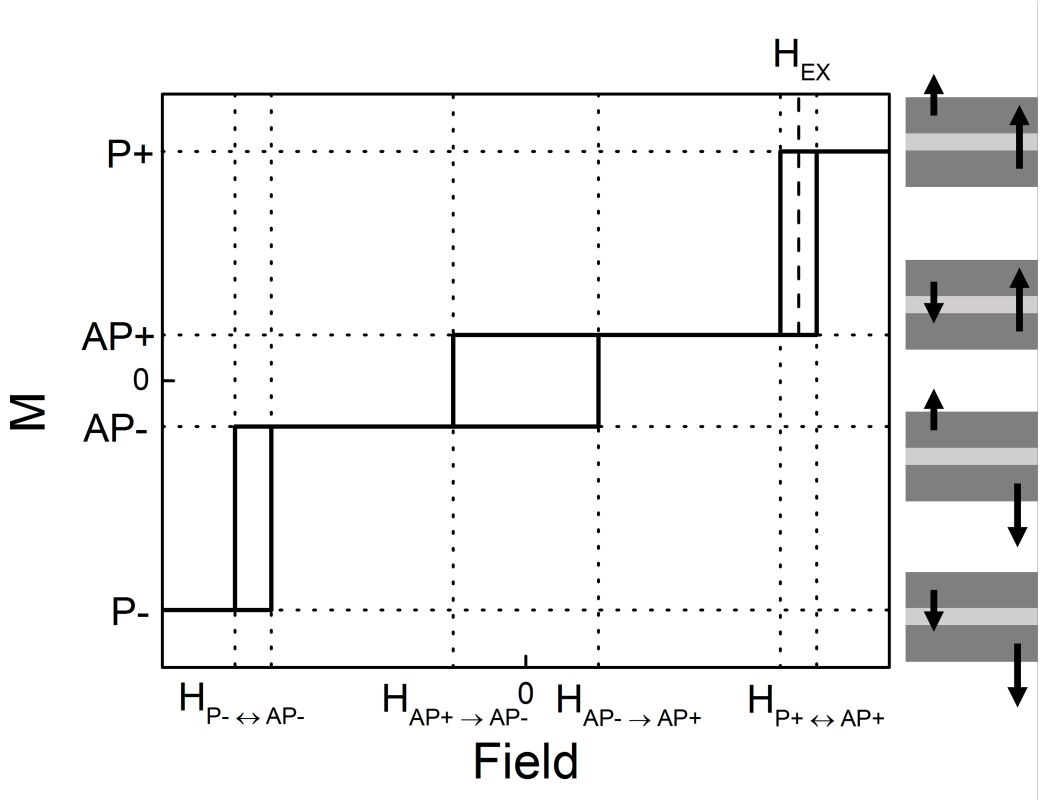

Figure 3.3: Schematic of the hysteresis loop of a perpendicular synthetic antiferromagnet as a function of an applied field

For 0.8 nm < x < 1.1 nm, the coupling is back again to ferromagnetic before we obtain a weaker antiferromagnetic coupling for x = 1.2 nm to x = 1.4 nm. For this range, we are not able to switch between AP- and AP+ as it was the case for the previous AF peak. Minor loops, which consist to stop the measure on an AP state, reveal the switching loop for a single layer. The shift to zero of the minor loops (H_{EX}) is directly related to the

coupling as $J_E = M_S.t_{FM}.H_{EX}$. Finally, for the couple last thicknesses studied, 1.5 nm and 1.6 nm, the coupling is ferromagnetic.

We report the exchange field H_{EX} as a function of the iridium thickness in figure 3.4. When the coupling is antiferromagnetic, the exchange field is represented with black circles and when the coupling is ferromagnetic, the exchange field is not defined and represented by crossed circle at zero. As expected, we obtain an oscillatory coupling between our ferrimagnetic layers with two antiferromagnetic peaks that we estimate at 0.5 nm and 1.2 nm which is quite close to the literature.

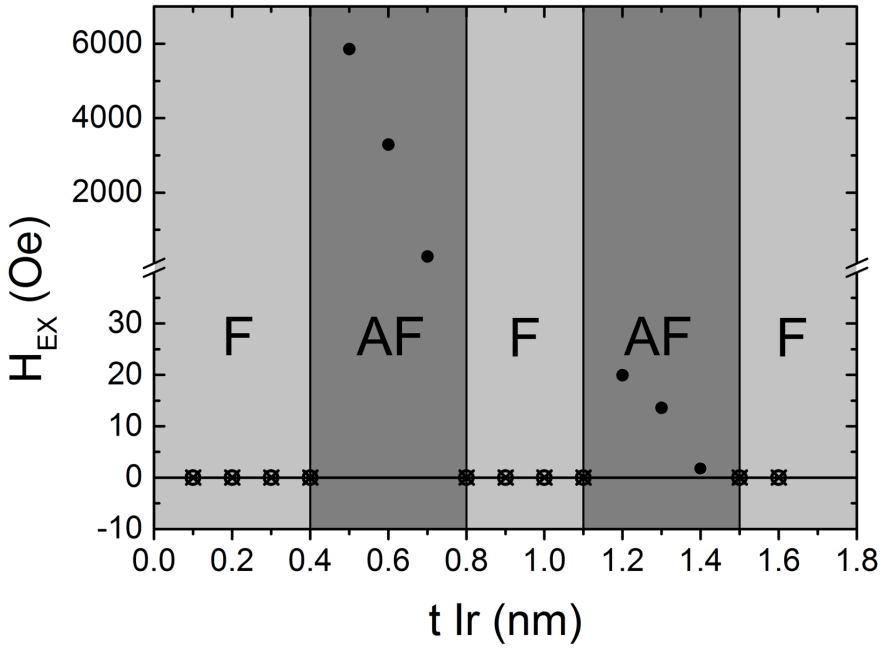

Figure 3.4: H_{EX} as a function of the iridium thickness, ferromagnetic (F) and antiferromagnetic (AF) ranges are represented by colored areas. For ferromagnetic coupling, H_{EX} cannot be defined and it is marked by crossed circle at H_{EX} = 0 Oe.

3.2.2 Gd-rich/FeCo-rich based

It is to be noted that it is possible to obtain a synthetic antiferromagnet with one FeCo-rich layer and one Gd-rich layer. This time, the coupling between FeCo sub-lattices needs to be ferromagnetic to obtain the lowest total magnetic moment. In order to obtain a Gd-rich layer, we used the properties of the interfaces studied in the previous chapter. For a FeCo-rich SAF, we used a $Gd_{25.7}FeCo$ layer at the bottom and a $Gd_{23.4}FeCo$ layer at the top separated by a 0.6 nm iridium spacer, to obtain strong coupling and sharp switchings (fig.3.5 (top)).

The difference of composition between the two ferrimagnetic layers is justified by the reverse set of interfaces seen by the GdFeCo that leads to two different compensation points. Changing the top layer composition from x = 23.4 to x = 25.7 is sufficient to get it Gd-rich. If we change the iridium thickness to 0.9 nm i.e. on the ferromagnetic peak (fig. 3.4 (bottom)), we ensure an synthetic antiferromagnet behavior and thus a compensated total magnetic moment at zero field. The Kerr signal is maximum at $H_Z = 0$ because the Kerr laser probes principally the cobalt and in this case, both FeCo sub-lattices are parallel when the magnetization is minimum. The value of H_{EX} and thus the amplitude of the coupling is as expected between the two AF peaks.

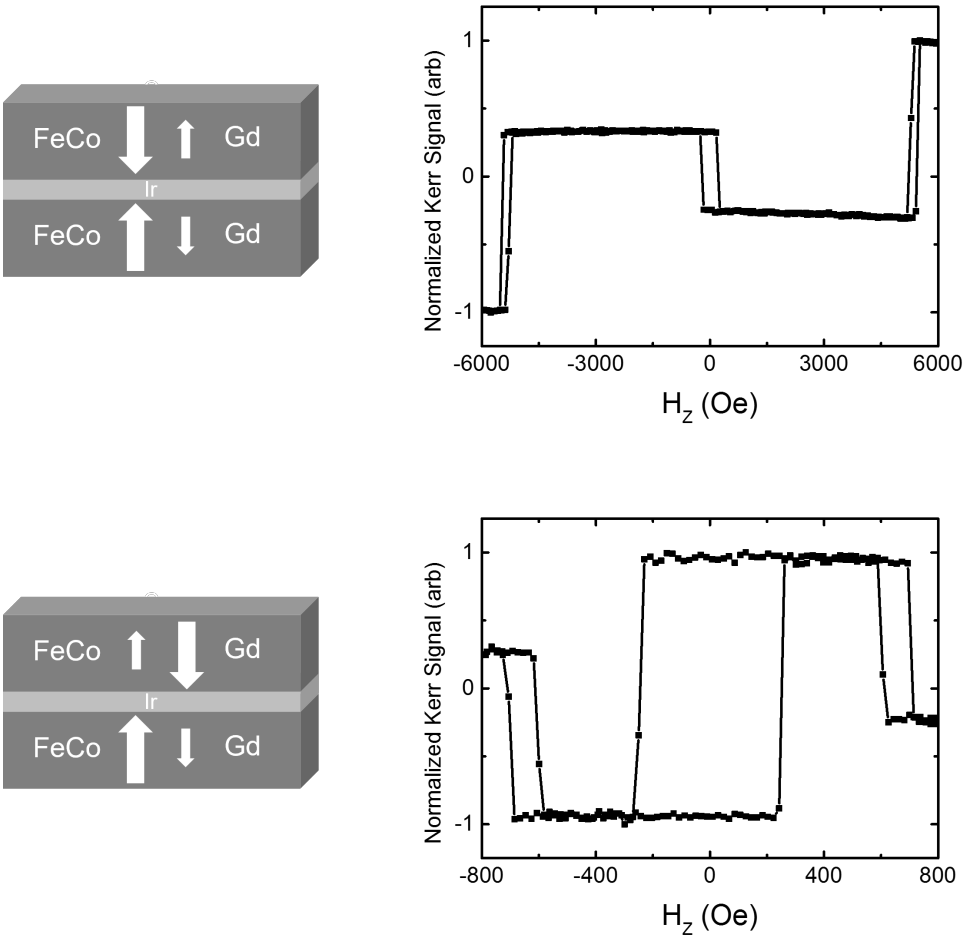

Figure 3.5: Hysteresis loop for (top) FeCo-rich SAF Ta/Cu/$Gd_{25.7}$FeCo/Ir(0.6 nm)/$Gd_{23.4}$FeCo/Cu/Pt and (bottom) Gd-rich/FeCo-rich SAF Ta/Cu/$Gd_{25.7}$FeCo/Ir(0.9 nm)/$Gd_{25.7}$FeCo/Cu/Pt

3.2.3 Transmission Electron Microscopy SAF

The quality of the SAF films has been confirmed by performing TEM again (fig.3.6 (top)). Both the top and bottom GdFeCo layers are amorphous as well as the Ir layer that is too thin (0.6 nm) to crystallize compared

to the 5 nm in the monolayer stacks. Both Cu layers and the Pt layer are crystallized and have a (111) texture e.g. the crystalline growth direction is [111] (fig.3.6 (bottom)). For Cu, d = 2.06 $\AA$, the interplane distance corresponds to the (111) planes: the lattice constant of the fcc Cu is a = 3.59 $\AA$, $d_{111} = \frac{a}{\sqrt{3}} = 2.06\AA$. For Pt, the lattice constant of the fcc Pt is a = 3.91 $\AA$ and thus $d_{111} = 2.25\AA$. We measure indeed d = 2.25 $\AA$.

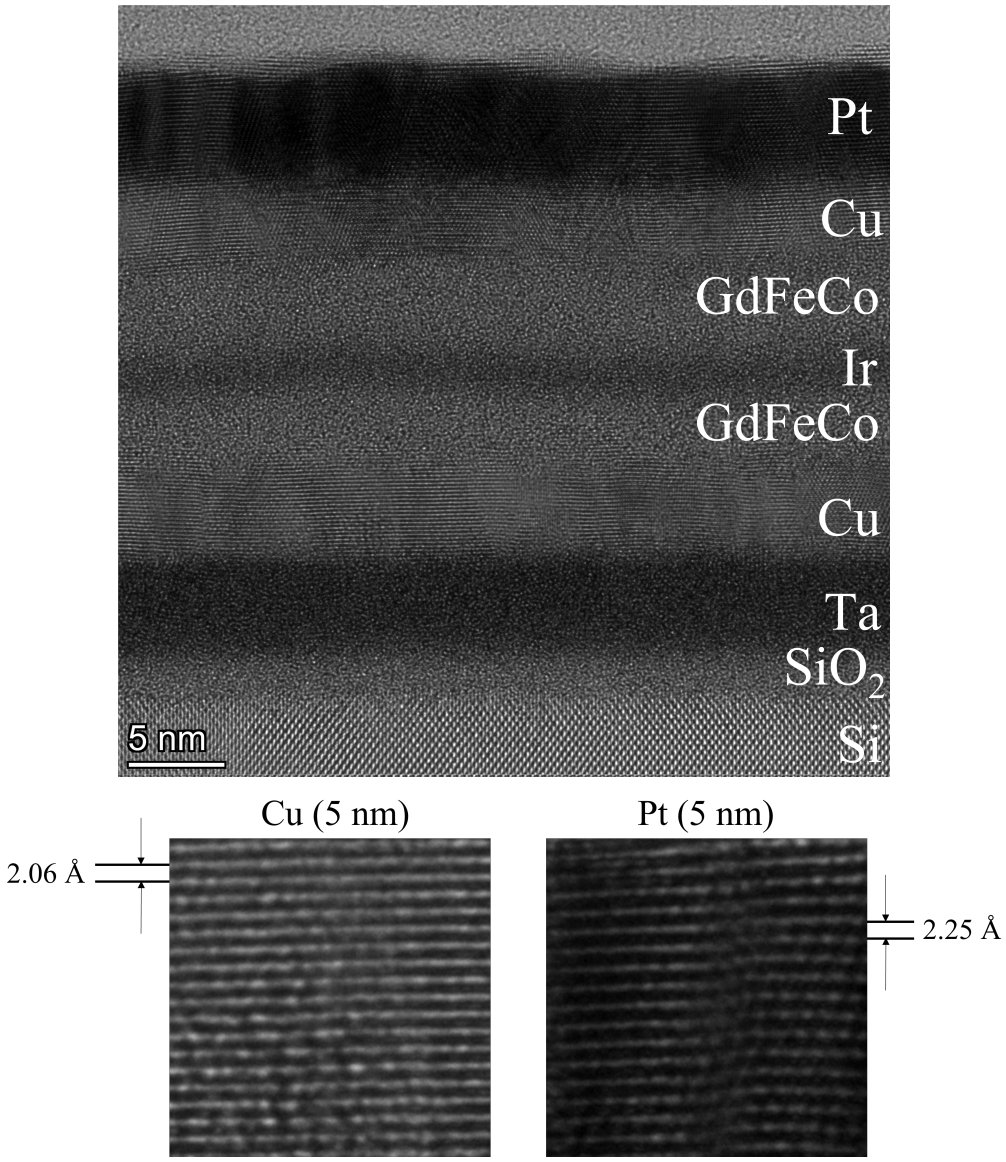

Figure 3.6: (Top) HRTEM micrograph for Ta(5)/Ir(5)/$Gd_{25.7}$FeCo(5)/Ir(0.6)/$Gd_{23.4}$FeCo(5)/Cu(5)/Pt(5). (Bottom) Zooms on (111) planes of Cu and Pt layers

We also performed Energy Dispersive X-Ray Spectroscopy (EDS) to determine the elemental composition as a function of the position in the bilayer (fig.3.7). The interfaces between Cu and GdFeCo, although irregular, are again well defined and the intermixing is limited. But in contrast, not surprisingly, the spectrums for Gd, Fe and Co show only one layer suggesting that the iridium spacer allows the diffusion even if we can clearly

distinguish it. Also the atomic fractions of the alloys drop a bit at the position of the Ir. Being a short-range interface interaction, the RKKY coupling is still ensured by the Ir atoms between neighbor Fe, Co atoms.

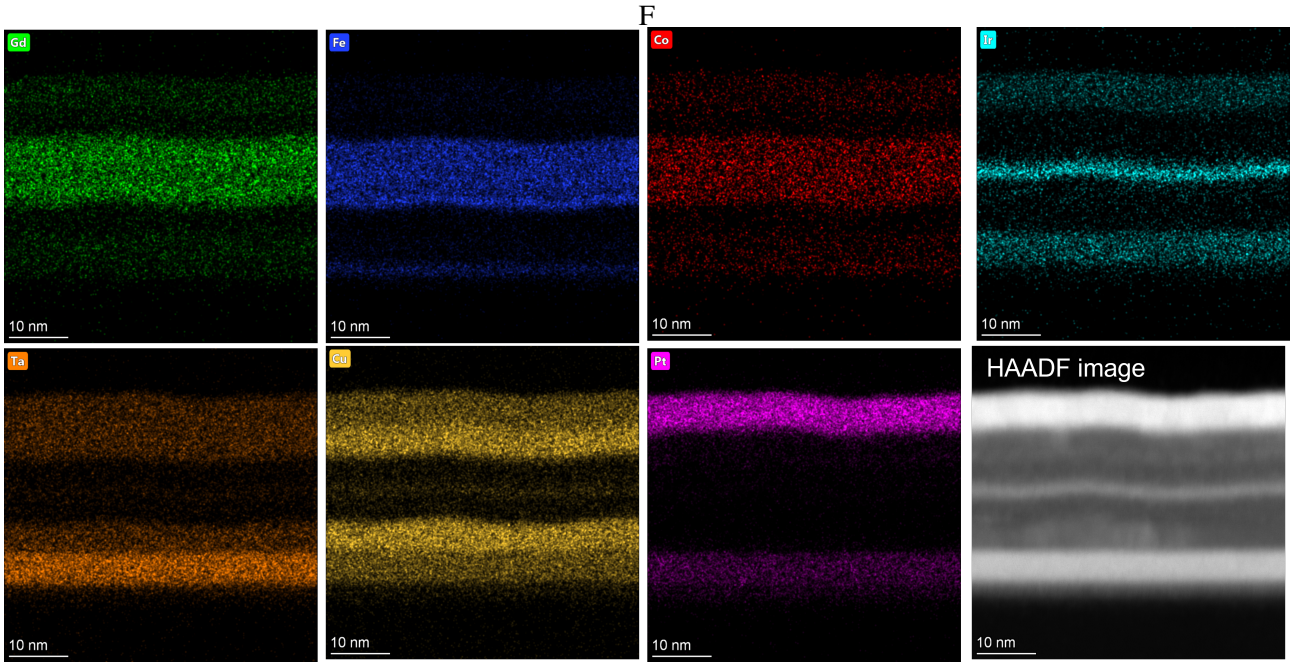

Figure 3.7: (Top) Atomic fraction and intensity of EDS for each element of the stack as a function of the position. (Bottom) EDS maps of Ta(5)/Ir(5)/$Gd_{25.7}$FeCo(5)/Ir(0.6)/$Gd_{23.4}$FeCo(5)/Cu(5)/Pt(5) cross-section for each element

3.3 Interactions in Synthetic Antiferromagnet

The typical hysteresis loop presented in figure 3.3 is interesting because we have access, with an applied field, to all the transitions between the different states. But under the effect of the temperature, the interfaces, the composition or after lithography, the interactions can lead to other kinds of hysteresis loops. A model can help us to understand the possible behaviors of the bilayers.

3.3.1 Stoner-Wohlfarth Model

The Stoner-Wohlfarth Model[71], which consists in a macrospin approach, describes a magnetic system at T = 0 K. This model can be completed by integrating the dependence with the temperature as an effective energy barrier. For magnetic multilayers stacks, different energy terms have to be taken in account and the total energy

of the synthetic antiferromagnet can be written as[72] :

$$E = E_{EX} + E_Z + E_{eff1} + E_{eff2} \tag{3.2}$$

with E_{EX} the exchange energy defined as $E_{EX} = -S.J_{EX}.\frac{\mathbf{M_1}.\mathbf{M_2}}{|\mathbf{M_1}|.|\mathbf{M_2}|}$ where J_{EX} is the surface exchange constant, S the surface, and M_1 and M_2 the magnetic moment of each layer. E_Z is the Zeeman energy defined as $E_Z = (\mathbf{M_1} + \mathbf{M_2}).\mathbf{H}$.

E_{eff1} and E_{eff2}, the potential barriers of reversal magnetization which are the difference between the zero temperature energy barriers caused by the magnetic anisotropy that is given by the Stoner-Wohlfarth model and the thermal energy $\varepsilon_T = k_B T$. The competition between those energies determines the aspect of the loop and the field necessary to the different state transitions. From the equation 3.2, we can calculate the energy of each stable state ($\uparrow\uparrow$, $\uparrow\downarrow$, $\downarrow\uparrow$, $\downarrow\downarrow$) as a function of the external field. The energies are lines in E(H) coordinates and the slope is determined by the mutual orientation of the magnetic moments $\mathbf{M_1}$ and $\mathbf{M_2}$ (fig. 3.8). Ruled by the principle energy minimization, the intersections of the lines determine the switching from a state to an other one and the threshold magnetic fields that correspond to these crossing points depends on field independent terms in equation 3.2. Indeed, E_{EX}, E_{eff1} and E_{eff2} terms change the threshold values by shifting straight lines along the energy axis. Then the switching occurs only when the energy of a stable state (solid lines) overcomes the threshold barrier of an other state (dotted lines) in figure 3.8. The critical switching magnetic fields are[72] :

- $H_{\uparrow\uparrow\Longrightarrow\uparrow\downarrow} = -H_{\downarrow\downarrow\Longrightarrow\downarrow\uparrow} = \frac{2|E_{EX}| - E_{eff2}}{2M_2}$,
- $H_{\uparrow\uparrow\Longrightarrow\downarrow\uparrow} = -H_{\downarrow\downarrow\Longrightarrow\uparrow\downarrow} = \frac{2|E_{EX}| - E_{eff1}}{2M_1}$,
- $H_{\uparrow\downarrow\Longrightarrow\downarrow\uparrow} = -H_{\downarrow\uparrow\Longrightarrow\uparrow\downarrow} = \frac{E_{eff1} + E_{eff2}}{2(M_2 - M_1)}$,
- $H_{\uparrow\downarrow\Longrightarrow\downarrow\downarrow} = -H_{\downarrow\uparrow\Longrightarrow\uparrow\uparrow} = -\frac{2|E_{EX}| + E_{eff1}}{2M_1}$,
- $H_{\downarrow\uparrow\Longrightarrow\downarrow\downarrow} = -H_{\uparrow\downarrow\Longrightarrow\uparrow\uparrow} = -\frac{2|E_{EX}| + E_{eff2}}{2M_2}$,
- $H_{\uparrow\uparrow\Longrightarrow\downarrow\downarrow} = -H_{\downarrow\downarrow\Longrightarrow\uparrow\uparrow} = \frac{E_{eff1} + E_{eff2}}{2(M_2 + M_1)}$.

In figure 3.8 (a) is represented the SAF behavior under the effect of an external magnetic field in the absence of the anisotropy barriers and is just then determined by the minimization of the sum of the exchange and Zeeman energies. By taking in account the additional potential barriers, we can distinguish three cases. When

$E_{eff1} > 2|E_{EX}|.\frac{M_1-M_2}{M_2}$ (fig.3.8 (b)), we reproduce the hysteresis loop that we already obtained in the previous parts. In this case, we have three types of transitions when we decrease the field from the saturated state ↑↑: ↑↑⟹↑↓,↑↓⟹↓↑ and ↓↑⟹↓↓. From the saturated state ↓↓, we have the three equivalent switchings: ↓↓⟹↓↑, ↓↑⟹↑↓ and ↑↓⟹↑↑. In figure 3.8 (c) is presented the case when $E_{eff2}.\frac{M_1}{M_2} - 2|E_{EX}|.\frac{M_1-M_2}{M_2} < E_{eff1} \leq 2|E_{EX}|.\frac{M_1-M_2}{M_2}$. It exhibits only two transitions. Indeed, it is not possible in this configuration to switch from the ↑↓ state to the ↓↑ in field. In order to access to one antiparallel state to the other, it is necessary to saturate the sample. Finally, we have a third case, when $E_{eff1} < E_{eff2}.\frac{M_1}{M_2} - 2|E_{EX}|.\frac{M_1-M_2}{M_2}$, that is similar as the one presented in (c) with only two transitions instead of three. But in this extreme case, the sample is still saturated when the field reaches zero and changes of sign.

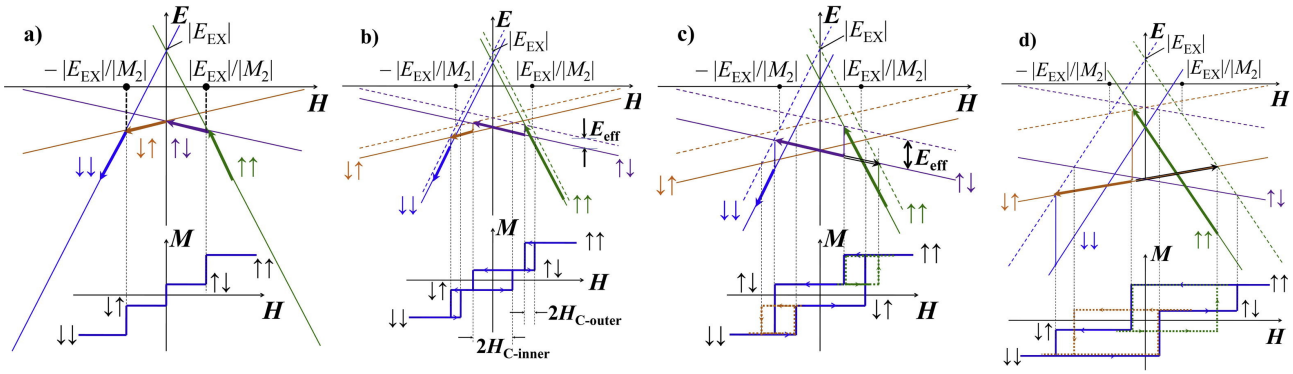

Figure 3.8: (Top) Energy diagrams and (bottom) simulated hysteresis loops of idealized M(H) curve (without energy barriers) (a), and different types of real hysteresis loops(b) (c) and (d) for antiferromagnetically coupled bilayer. For the energy diagrams, solid lines indicate the energy of the stable magnetic states ↑↑ (green), ↑↓ (violet), ↓↑ (orange) and ↓↓ (blue). The dashed lines are curves for the same states that takes in account the anisotropy barriers. Taken from [72]

3.3.2 Experimental results

Experimentally, we have observed some of the different types of loops presented in the previous section. Some of the full films present intrinsically different behaviors and some changes after patterning.

Effect of the interfaces

In figure 3.9 (top) is shown the loops obtained for Ta(5)/Cu(x)/Gd_{25}FeCo(5)/Ir(0.55)/$Gd_{22.8}$FeCo(5)/Cu(x)/Pt(5) with 0 nm < x < 5 nm. From 5 nm to 3 nm of Cu, there is no major change but a shift of the outer loop. At 2 nm, the shift is more important and with only 1 nm the Kerr sign of the inner loop changes indicating that

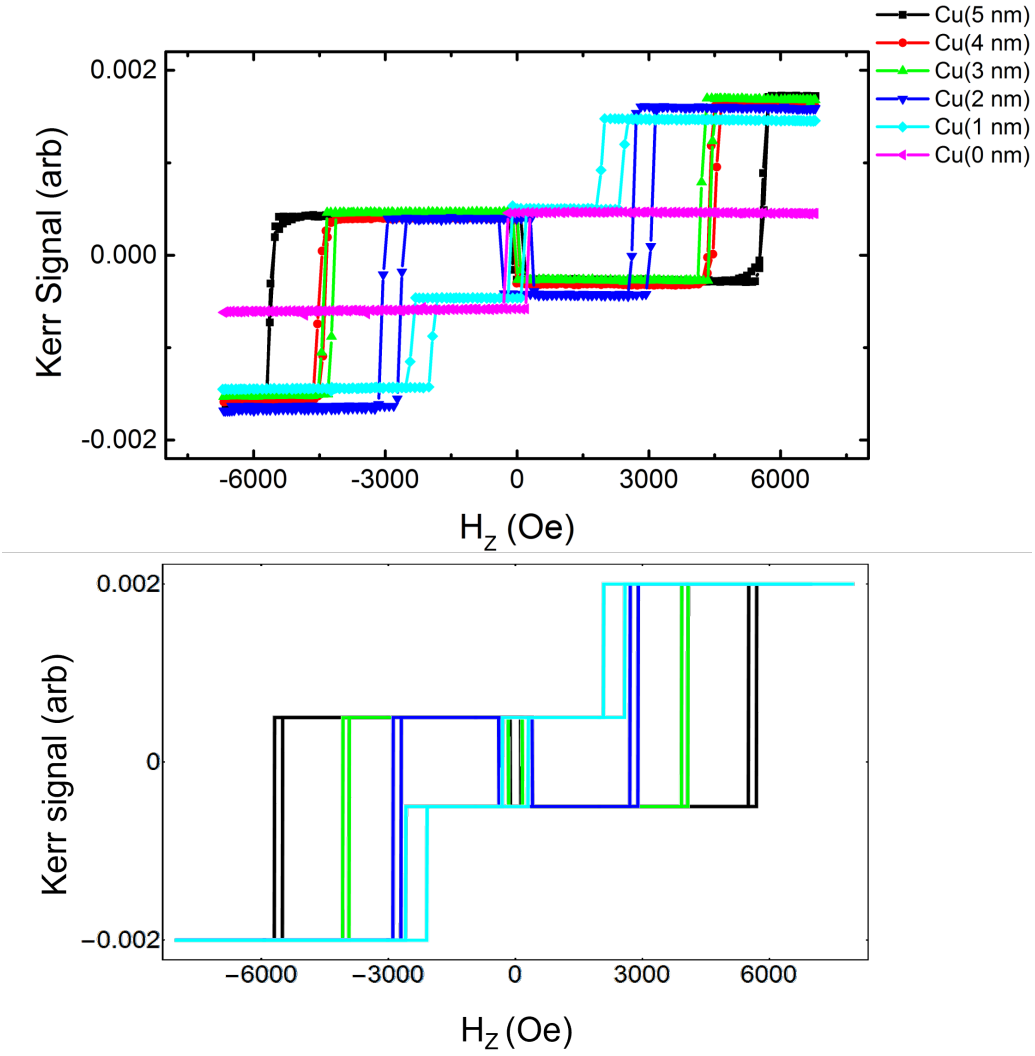

Figure 3.9: (Top) Hysteresis loops measured by Kerr laser for different Ta(5)/Cu(x)/Gd_{25}FeCo(5)/Ir(0.55)/$Gd_{22.8}$FeCo(5)/Cu(x)/Pt(5) with 0 nm < x < 5 nm. (Bottom) Simulated SAF hysteresis loops for $J_{EX} = -0.14$ erg/cm^2, (black) $E_{eff1} = 0.01$ erg/cm^2, $E_{eff2} = 0.01$ erg/cm^2, $M_2 = 150$ emu/cc $M_1 = 50$ emu/cc, (green) $E_{eff1} = 0.01$ erg/cm^2, $E_{eff2} = 0.01$ erg/cm^2, $M_2 = 150$ emu/cc, $M_1 = 70$ emu/cc, (blue) $E_{eff1} = 0.01$ erg/cm^2, $E_{eff2} = 0.01$ erg/cm^2, $M_2 = 150$ emu/cc, $M_1 = 100$ emu/cc and (cyan) $E_{eff1} = 0.01$ erg/cm^2, $E_{eff2} = 0.03$ erg/cm^2, $M_2 = 120$ emu/cc, $M_1 = 250$ emu/cc

the magnetization of one layer has exceeded the other. Without copper, the top layer is in plane and we only measure the hysteresis loop of the bottom one. We have seen in the previous chapter that the iron and the cobalt can be polarized at the vicinity of the Pt layer. When we decrease the copper thickness, the top layer becomes closer and closer to the platinum and thus the saturation magnetization of this layer increases. In figure 3.9 (bottom), we simulate the Kerr signal of the SAF based on the equation 3.2. Since the bottom layer should not polarize with the tantalum, from the initial state in black, we only increase the magnetization of the top layer. We are able to reproduce the linear behavior as a function of the thickness of the Cu layer. As the magnetization

increases, the switching fields of the outer loops decrease as expected since the $\uparrow\downarrow \Longrightarrow \downarrow\downarrow$ or $\downarrow\uparrow \Longrightarrow \uparrow\uparrow$ types of transitions are inversely proportional to the magnetization of the switching layer. In cyan is simulated the case when the initially highest magnetization layer becomes the lowest magnetization one and thus it switches first inverting the sign of the Kerr signal of the inner loop. To accurately simulate this case, it is also necessary to decrease the magnetization of the other layer suggesting a loss of moment in contact with tantalum that can be explained by a greater intermixing at the interface. All these results strengthen the hypothesis of the polarization of the GdFeCo with adjacent layers. One should note that ultimately some anisotropy adjustments have to be done to report the enlargement of the outer cycles.

Effect of the lithography

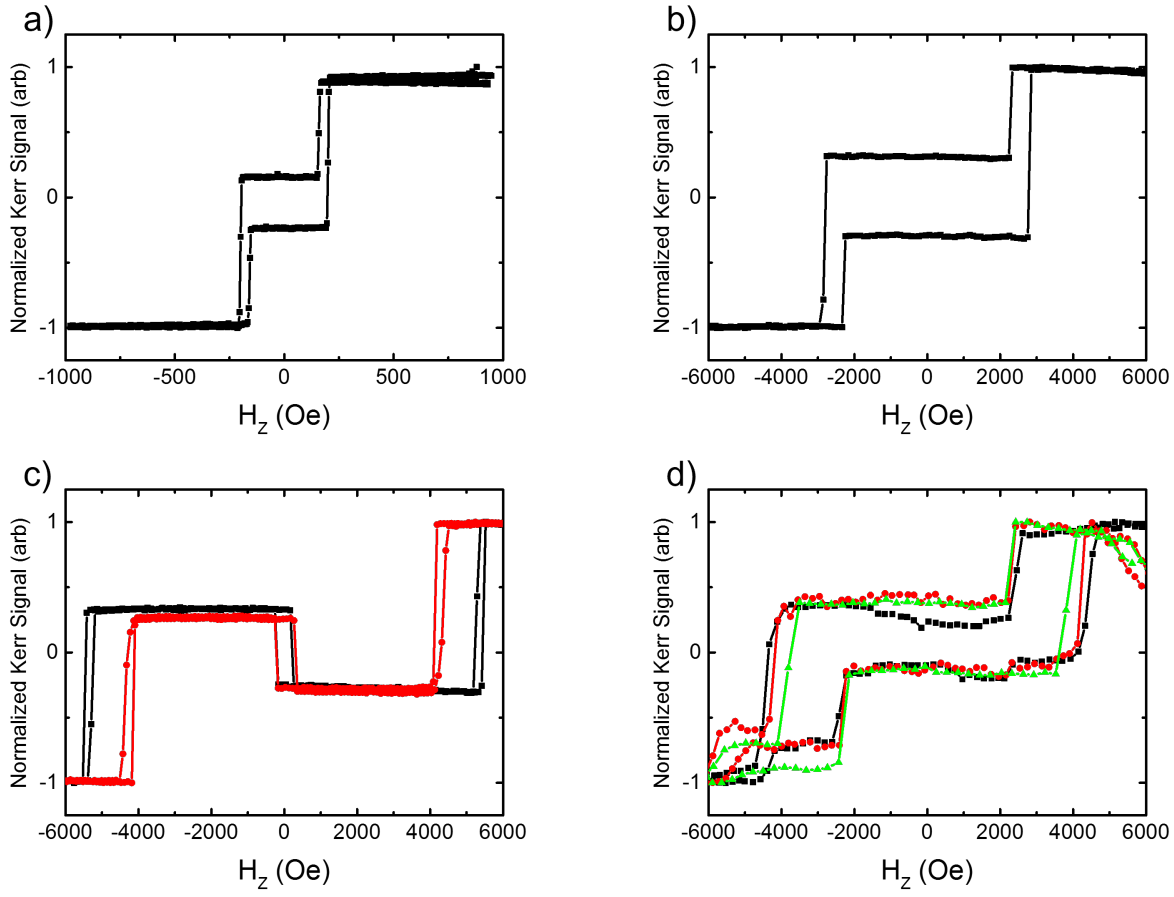

Figure 3.10: Hysteresis loops measured by Kerr laser of (a) Ta(5)/$Gd_{20.9}$FeCo(5)/Ir(0.6)/Gd_{25}FeCo(5)/Pt(5) full film, (b) Ta(5)/Cu(5)/$Gd_{22.2}$FeCo(5)/Ir(0.6)/$Gd_{24.6}$FeCo(5)/Cu(5)/Pt(5) full film, (c) Ta(5)/Cu(5)/$Gd_{23.4}$FeCo(5)/Ir(0.6)/$Gd_{24.6}$FeCo(5)/Cu(5)/Pt(5) full film before baking (black) and after 2 minutes at 115°C and then exposed to the ion beam without etching (red) and (d) Kerr signal from several micrometers devices (Hall crosses, wires) at different areas of the patterned film for Ta(5)/Cu(5)/$Gd_{23.4}$FeCo(5)/Ir(0.6)/$Gd_{24.6}$FeCo(5)/Cu(5)/Pt(5)

The hysteresis cycle presented in figure 3.8 (c) has been observed in full films when one layer is far from the compensation as show in figure 3.10 (a) and (b). But this type of cycles has been also observed after the patterning of some full films initially exhibiting an other loop. For the SAF presented in figure 3.10 (c), the initial loop is the black one. Then, in red, a piece of this full film has been entirely covered with resist and exposed to a temperature of 115°C during 2 minutes before being exposed to the same ion beam as for the etching of the pattern. Except a quite small shift of the outer loop, the sample remains the same. But, for an other piece that has been patterned into Hall crosses and wires, the loop is quite different and the transitions $\uparrow\downarrow \Longrightarrow \downarrow\uparrow$ and $\downarrow\uparrow \Longrightarrow \uparrow\downarrow$ are not accessible anymore (fig.3.10 (d)).

3.4 All-optical switching of the SAF

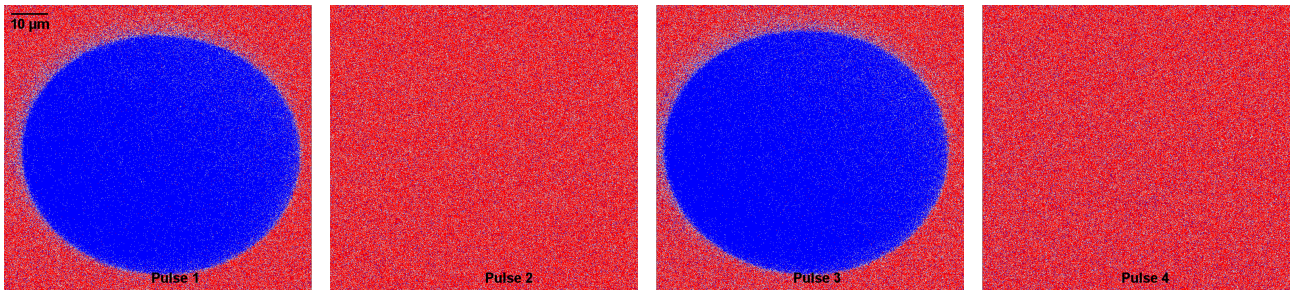

Figure 3.11: Kerr microscopy images of Glass/Ta(5)/Cu(5)/$Gd_{24.5}$FeCo(5)/Ir(0.6)/$Gd_{22.2}$FeCo(5)/Cu(5)/Pt(5) after successive single linearly polarized femtosecond laser pulses. The AP+ state is in red and the AP- in blue.

As explained in the introduction, the magneto-optical properties of GdFeCo are interesting and allow to reverse the magnetization of single layers of this material with a single linearly polarized femtosecond laser pulse. In this work, we also show that it is possible to switch the magnetization of the GdFeCo-based SAF with a pulse. We used a Ti:sapphire femtosecond laser source with regenerative amplifier. The typical profile of a pulse can be fitted by a Gaussian envelope and the pulse duration τ_l can be determined from the full width or full duration at half maximum as $\tau_l = 2\sqrt{2ln(2)}\sigma$ with σ the standard deviation. The pulse duration of the Ti:sapphire laser is around 35 fs. To determine the fluence, we first measure the power P of the laser using a power meter. The energy E is given by $E = P/f$ with f the repetition rate of the laser. Finally the fluence $\bar{F} = \frac{E}{\pi w^2}$ with w the beam radius determined from the beam profile where the optical intensity drops to $\frac{1}{e^2}$. In our case, $P = 3.19$ mW, the fluence is $\bar{F} \approx 6.18$ mJ/cm^2. As shown in figure 3.11, we have been able to successfully switch the magnetization back and forth of a GdFeCo/Ir/GdFeCo SAF (Kerr loop of the film is shown in figure 3.10 (c) in black) with a single femtosecond pulse. Before the first pulse, the sample is saturated in the P+ ($\uparrow\uparrow$)

state then the field is switched off. The SAF is then in the stable AP+ state (red). The first pulse reverses the magnetization and nucleates a AP- state (blue) magnetic domain of the size of the beam. A second pulse allows to return to the initial state. With a third pulse, we can re-nucleate a domain and go back and forth indefinitely between the two AP states.

3.5 Conclusion

In conclusion, we have shown the possibility to obtain an antiferromagnetic coupling between two GdFeCo ferrimagnetic layers mediated by an Ir spacer using the RKKY interaction. We have been able to observe the two first antiferromagnetic peaks of the Ir as well as ferromagnetic coupling. The Stoner-Wohlfarth model has allowed us to reproduce the behavior that we have observed and to understand the evolution of the hysteresis cycle of the SAF. These results support the findings of the previous chapter. We have shown that we can have a SAF with compensation of the net moments with a Gd-rich and a FeCo-rich layers and a ferromagnetic coupling between FeCo sub-lattices.

Moreover, with the magneto-optical properties of the GdFeCo, we have demonstrated that it is possible to switch the magnetization of the SAF with a femtosecond laser pulse. Even it is not the main part of this work, this a additional way to nucleate domains and it could be combined with SOT to efficiently manipulate the magnetization in the SAF.

Chapter 4

Magneto-transport measurements: current-induced switching in GdFeCo

Our GdFeCo films are now well characterized and all our stacks include Pt, Ir or Ta layers that exhibit very large spin Hall angle (SHA) and thus efficient magnetization switching via SOT is expected. Ta and Pt have opposite SHA in the same order of magnitude[73]. We also have Ir interfaces since it is necessary to ensure strong RKKY coupling and to maintain PMA in our SAF. The SHA of Ir and Pt have the same sign but the Ir one is estimated at only 26% of the one of Pt[74]. The switching of the GdFeCo by induced spin currents has already been studied either in simple stacks like Ta(10)/GdFeCo(5)/SiN(5)[36] or in more complex samples such as ferrimagnet layers with a gradient of composition[24]. From our study, it is clear that due to their very low thicknesses, our samples are sensitive to any change of composition or adjacent layers and it would be interesting to investigate their switching by SOT.

4.1 Experimental methods

4.1.1 Lithography

For AHE measurements and SOT reversal, the full films have to be patterned into micro-devices in a clean room in order to control the direction of injection of the current and to increase the current density. For the size of

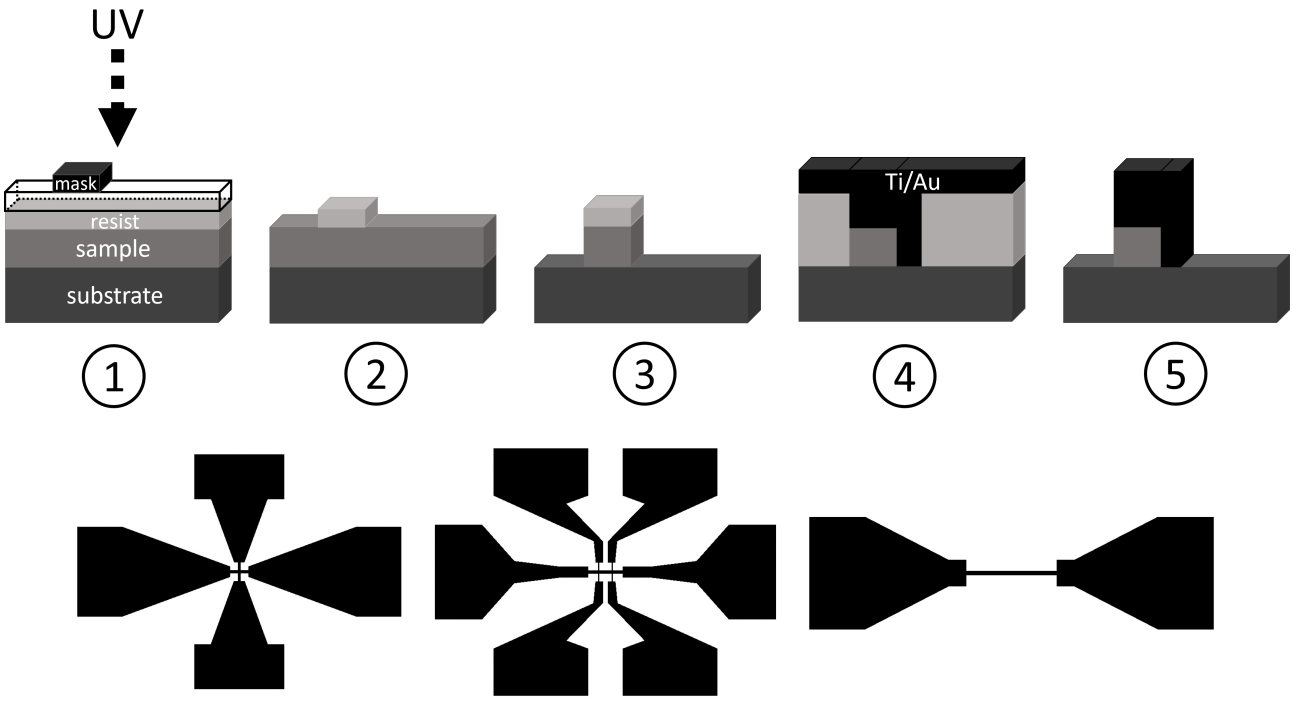

Figure 4.1: (Top) Schematic of the different steps of the UV lithography: (1) Spin coating and lithography (2) Development (3) etching (4) Spin coating, lithography and Ti/Au deposition (5) Lift-off. (Bottom) Examples of different lithographed micro-structures: (right) Hall bar (center) double Hall bar (right) wire

crosses targeted, the patterning is relatively simple and consists in different steps presented in figure 4.1 (top). First, the principle is to cover the sample with a photosensitive resist. This resist, baked at 115°C, is exposed to UV light or electrons beam. For UV lithography, the patterns are defined by a mask placed over the sample that only exposes the wanted part of the photo-resist (1). For e-beam lithography, the devices are drawn in the resist by a beam of electrons. In our case, the case of a positive resist, the long carbon chains that constitute the polymers of the resist are shortened by the UV light making them more soluble. A short dip in the developer will then only remove the exposed parts (2). It remains only on the surface of the sample, the pattern defined by non-exposed areas of the resist that will protect the layers below. After this step, all the sample is etched by Ar+ ions beam (3). The etching is stopped when the substrate is reached. At this point, only the parts protected by the resist remain on the sample, the ion milling being insufficient to etch the thick layer of resist. The resist over the non-etched areas is removed by a chemical solution called remover and the sample is coated again by two layers of resist with different initial solubilities that are baked at 140°C in order to define the electrical contacts. The pattern of the contacts is drawn by UV light through an other mask and then developed. The differences of solubility lead to a slight overdeveloping of the lower layer of resist allowing the remover to go underneath the top layer making the lift-off easier. The lift-off step (4) consists in a bilayer of Ti(10 nm)/Au(150 nm)

evaporated on the sample where the titanium is an adhesive layer for the gold that will be our electrical contact. Finally, after removing the resist and the extra Ti/Au, it remains the devices obtained at step (3) covered with gold (5).

Our devices consist in three patterns (fig.4.1 (bottom)): the single Hall cross, the double Hall cross and the wire. On lithographed films, all these devices are present with four different widths of 2, 5, 10 and 20 μm.

4.1.2 Magneto-transport setups

In order to perform electrical measurements, the patterned samples are diced and then mounted and glued on a chip-carrier which consists in a square-shaped piece of plastic with sixteen Electroless Nickel Immersion Gold (ENIG) pads connected to pins. The micro-devices gold pads are wire-bounded to the chip-carrier ENIG pads by ultrasonic bounding of an aluminum wire. The devices are then connected to the measurement setup by placing the chip-carrier into a chip-carrier-socket. During these steps, one have to take care of electrostatic discharges with grounded working area and wrist bands.

4.1.3 AHE and SOT measurement setup

An important part of this PhD project has been dedicated to the electrical transport measurement of our samples. For this, we have built a setup (fig.4.2) that consists in a chip holder, composed of a PCB board with a chip socket, placed into the air-gap of an electromagnet. A Keysight 34980A multifunction switch allows us to set every possible combinations of connections between the sixteen chip-carrier pads and the different instruments. We use a Keithley 6221 AC and DC Current Source that can deliver up to 110 mA and send pulses as short as 50 μs for I-V measurements. To measure the voltage, we have at our disposal a 2182A Nanovoltmeter optimized for low noise levels. The magnetic field is controlled by a KEPCO power supply and measured by a Lakeshore 455 DSP Gaussmeter mounted next to the sample. An oscilloscope can be added at the end of the circuit to check the shape of the pulses. The setup is interfaced with a computer via GPIB connectors and is fully automated by homemade programs using LabVIEW libraries.

For AHE measurement, we apply a DC current of I $\approx$ 1 mA and we measure the transverse voltage with the nanovoltmeter while sweeping the perpendicular to film plane magnetic field for coercive field measurement or the in-plane field for saturation field measurement. Our samples exhibit PMA meaning that the magnetization can take two stable orientations along the axis of anisotropy. We have then two maximum levels of transverse

Hall voltage at rest if we consider the full reversal of the Hall cross.

For SOT measurements, we inject current pulses with the Keithley 6221 that communicates with nanovoltmeter over the serial interface. We use the Pulse Delta mode that allows us to read the level of the Hall resistance during the pulse. The principle of the mode is to do an AHE measurement using the current of the pulse. For this, a 2 or 3-point repeating-average algorithm is used to calculate the readings. With 3 points, first a low pulse with defined parameters is sent by the I-source, the voltage is measured by the nanovoltmeter during the pulse (A). The second pulse is high level pulse and the voltage is also measured (B). Finally, the third pulse is a low one with a measure of the voltage again (C). The Pulse Delta reading is $\frac{2B-A-C}{2}$ and $\frac{2B-2A}{2}$ without the second low pulse. The reading of the voltage during the pulse can cause some artifacts because of the induction or the non-equilibrium of the system. Therefore, in parallel of the Delta measurement, after a small delay after each pulse to ensure that the sample is at rest, a small reading current is applied and the transverse voltage is measured. The length of the pulses is 100 μs and for a defined field, the current intensity is sweeped back and forth. After the SOT switching measurement at one field, a large in-plane saturation field of 5000 Oe is applied taking advantage of the out-of-plane component of the field to fully reverse the magnetization before the next measurement.

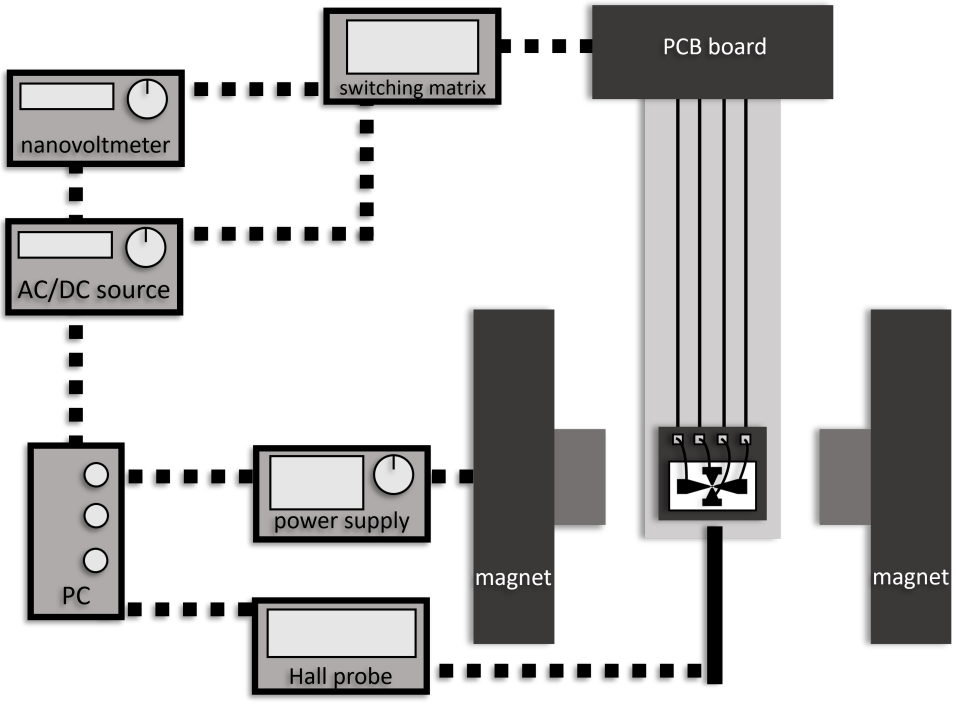

Figure 4.2: Schematic of the magneto-transport measurements setup

SOT measurement under Kerr microscope

A second setup very similar to the one presented in figure 4.2 has been also used. It consists in the same current source coupled to the same nanovoltmeter connected to a PCB board placed under a Kerr microscope. This setup allows us to image magnetic domain nucleation and propagation in micro-devices. After each pulse, a picture is taken and we have then a image corresponding to each point of the measured hysteresis loop.

4.2 Results

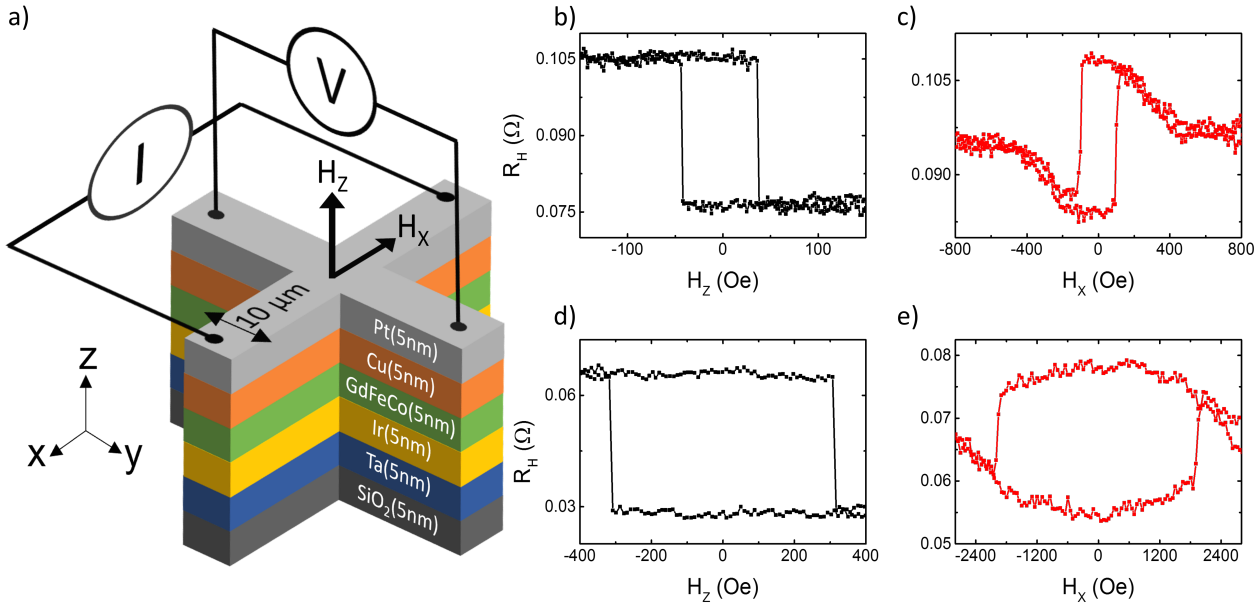

Figure 4.3: (a) Schematic of the experimental setup for the measurement of AHE and SOT switching in a Hall cross. Out-of-plane (black) and in-plane hysteresis (red) loop measured by AHE for respectively Cu/GdFeCo/Ir (b)(c) and Ir/GdFeCo/Cu (d)(e)

In this part, we focused our work on single GdFeCo layer samples. The typical stacks are Ta/Cu/GdFeCo/Ir/Pt and the same one with inverted copper and iridium layers. They are the sub-systems that make up the SAF and it is then interesting to investigate their behavior under SOT before focusing on the bilayers. Similar to MOKE measurement, the magneto-transport properties are dominated by the 3*d* orbitals of TM and the sign of the loop is also determined by the FeCo moment orientation thus a Hall signal can be measured even at the magnetic compensation point. In figure 4.3 (a) is shown the geometry of the measurement in the Hall cross. The current is injected along x-axis and the transverse voltage is measured along the y-axis. The external magnetic field

can be oriented either along the x or z-axis. The composition of the alloy is $Gd_{24.6}Fe_{67.3}Co_{8.1}$.

The AHE results are presented in figure 4.3 for Ta/Cu/GdFeCo/Ir/Pt (b)(c) and for Ta/Ir/GdFeCo/Cu/Pt (d)(e). We know from the study in chapter 2 that these samples are not equivalent in terms of magnetic properties. Indeed, we find that the magnetic compensation is not at the same composition for the two kind of samples. For the same nominal composition, we have two different coercive fields. Indeed, at $x = 24.6\%$, from figure 2.5, the Ta/Ir/GdFeCo/Cu/Pt sample is expected to be closer to the compensation than the sample with reverse interfaces and it is confirmed by the anomalous Hall signal with a larger coercive field ($\approx$ 300 Oe vs 40 Oe). Also, the in-plane saturation field is five times smaller for this particular Ta/Cu/GdFeCo/Ir/Pt sample suggesting that the anisotropy is weaker but the M_S is also expected to be much higher. Indeed for a sample with a composition at $x = 26.4\%$, the saturation field is around 2000 Oe. Then, one should note here that for other samples similar saturation fields have been observed independently of the nature of the seed layer. Nonetheless, it is interesting to compare the efficiency of the switching in these two samples.

The AHE experiments have been followed by SOT switching measurements. In our samples, we expect a current pulse to generate a transverse spin current when it goes through the heavy metal layers (Ta, Pt, Ir). We consider that the copper layer is transparent to a spin current because the spin length diffusion in this material is several hundred nanometers[75]. Depending on the sample stack order, the GdFeCo layer experiences different combination of torques. For the Ta/Cu/GdFeCo/Ir/Pt sample, the spin currents arise from Ta and Ir layer. The spin current from Pt is stopped in the Ir layer. Since Ta and Ir have opposite SHA, the SOT switching should be very efficient. In the other stack, Ta/Ir/GdFeCo/Cu/Pt, the spin currents arise from Ir and Pt which have the same SHA. Therefore, we expect a less efficient switching even if the SHA of the Pt is larger than the Ir one. The Keithley 6221 was parameterized to send square current pulses with 100 μs duration. An oscilloscope at the end of the circuit confirms that the pulse transmitted through our micro-device has the right shape, the right duration, the correct intensity and that the rising time is negligible (fig.4.4).

Several sizes of Hall crosses have been patterned but we have first used the 2 μm-wide ones for SOT measurements in order to have the highest current density. In figure 4.5 is shown an example of switching hysteresis loops for Ta(5)/Cu(5)/$Gd_{24.6}Fe_{67.3}Co_{8.1}$(5)/Ir(5)/Pt(5). For each in-plane applied field intensity, we probe the magnetic state of the sample by calculating the Hall resistance and we distinguish the increasing and the decreasing current parts of the loops. We define ΔR, the amplitude of the hysteresis loop as the decreasing part resistance minus the increasing part resistance. If we plot ΔR for any field , we can visualize the state diagram of the samples on which we can see the critical current of the switching and the amplitude of the switching. In

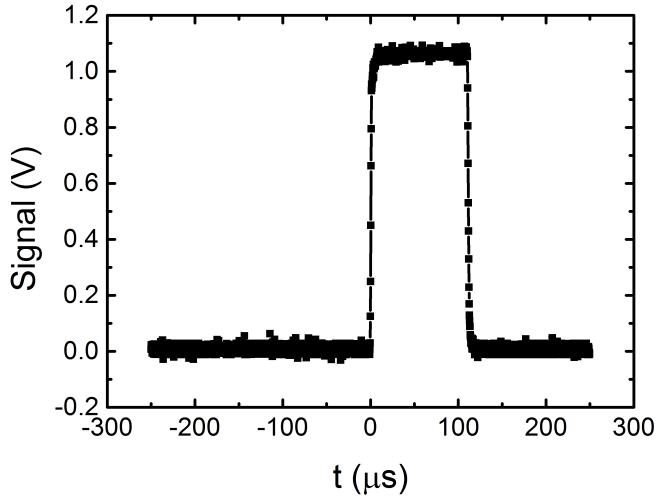

Figure 4.4: Shape of the transmitted pulse of 100 μs through a 2 μm-wide Hall cross

figures 4.5 (b) and (d), we show the state diagrams of the two different stacking order for $Gd_{24.6}Fe_{67.3}Co_{8.1}$. For the sample with Cu under and Ir over the GdFeCo, the switching occurs in a narrow range of fields. Around 200 Oe, we can see that the amplitude of the switching is decreasing until there is no switching at all when the field is too high and the magnetization is locked along the magnetic field. This is particularly visible with the projection of the diagram in the figure 4.5 (c). It is clear that the switching amplitude is the greatest for the lowest field. As expected, the critical current density increases when the magnetic field decreases. We can also note that the relative sign of the switching depends on the sign of the applied field which corresponds to the conventional geometry of SOT switching. More surprisingly, we still observe a switching at very low field and even in the absence of field. Indeed, a break of symmetry is needed in order to switch the magnetization of a material that exhibits PMA as seen in the introduction chapter of this thesis.

In the second sample, Ta/Ir/GdFeCo/Cu/Pt, we can observe SOT switching at larger field values since it becomes impossible to switch the magnetization after 2000 Oe (fig.4.5 (d)) which tends to confirm that the anisotropy is higher. We can note that the current density needed to switch is also higher than in the previous sample which can probably be explained by the less effective interfaces in terms of SHA. On the other hand, zero field switching cannot be achieved in this sample. In fact, no switching is observed in a range of -200 Oe < H_X < 100 Oe. The different asymmetries of the diagrams could be due to the small misalignment of the magnetic field with the plane of the Hall cross or the defects of the patterned devices.

These results first made us think that the anisotropy could play an important role in the switching in the absence of external magnetic field. The Joule heating caused by the current injection could bring the magneti-

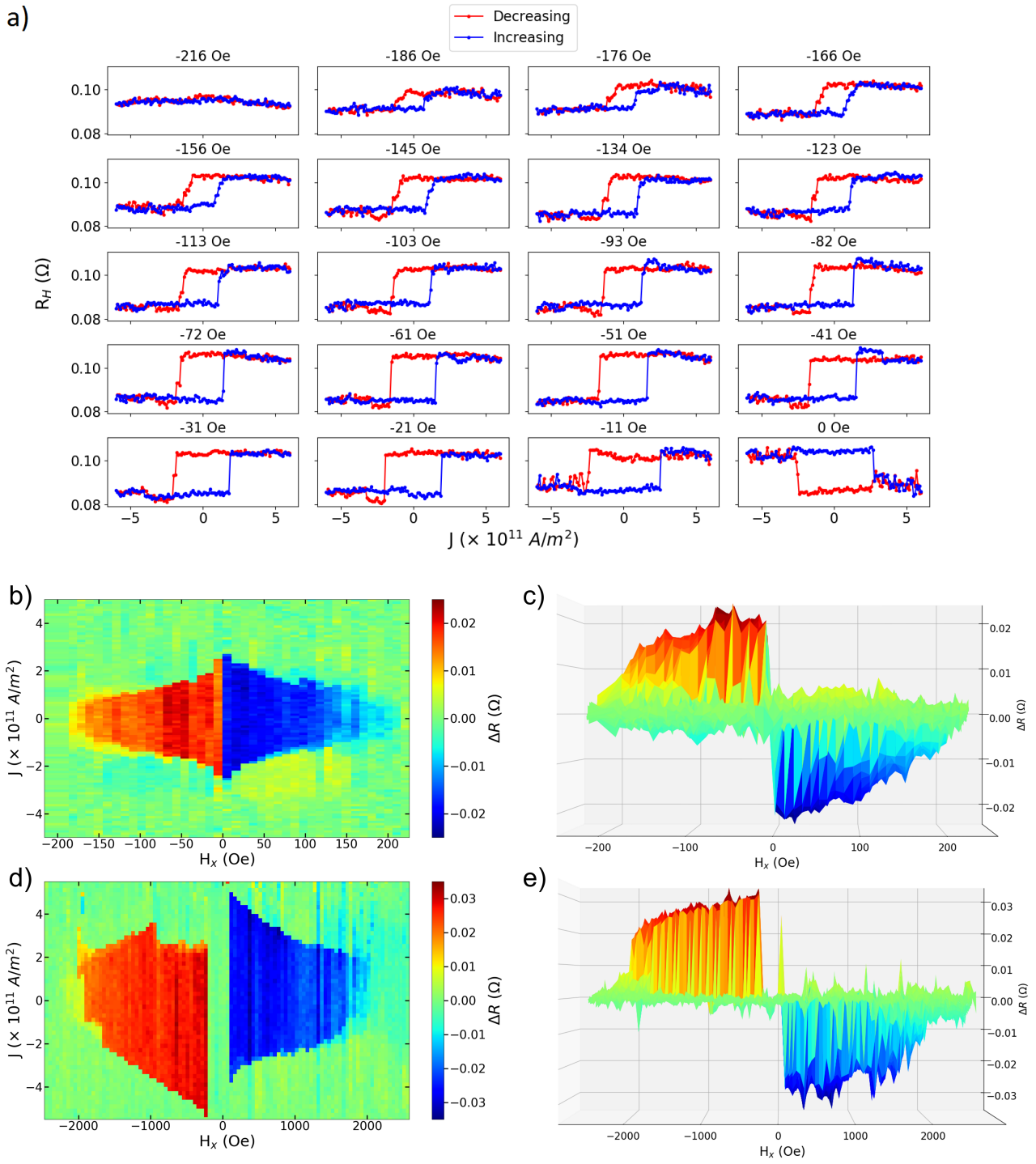

Figure 4.5: Example of hysteresis loops obtained by SOT switching for different negative field for Ta(5)/Cu(5)/$Gd_{24.6}Fe_{67.3}Co_{8.1}$(5)/Ir(5)/Pt(5) (a). SOT state diagrams and hysteresis loops amplitude as a function of magnetic field for 2 μm-wide Hall crosses of respectively Ta(5)/Cu(5)/$Gd_{24.6}Fe_{67.3}Co_{8.1}$(5)/Ir(5)/Pt(5) (b)(c) and Ta(5)/Ir(5)/$Gd_{24.6}Fe_{67.3}Co_{8.1}$(5)/Cu(5)/Pt(5) (d)(e)

zation to the plane of the sample breaking the symmetry as the external field could do it. This would explain that the sample with the higher saturation field does not switch without the bias field.

An other hypothesis is the gradient of composition that the seed layer could induce in the bulk of the GdFeCo. This leads to a bulk DMI that breaks the symmetry as well as it has been observed in [24].

4.3 Investigation

4.3.1 Measurements on 10 μm-wide Hall cross

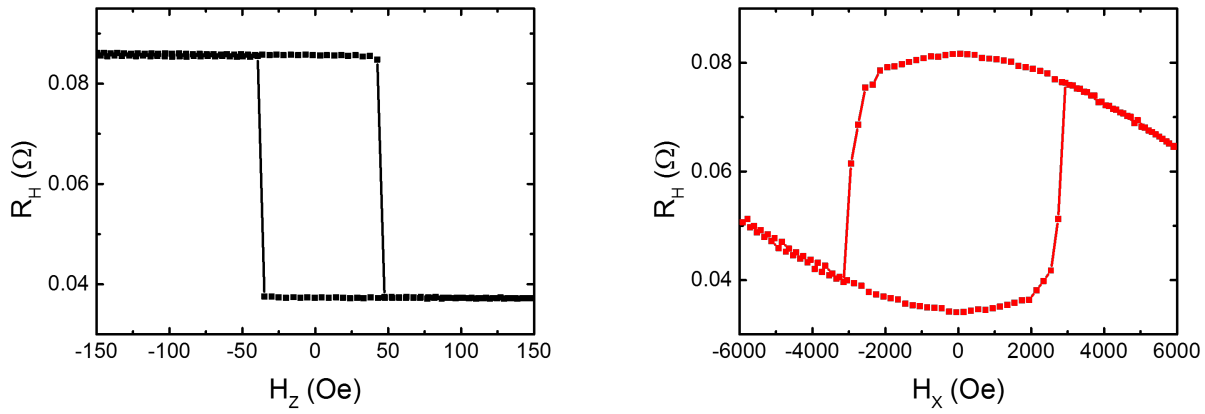

Figure 4.6: AHE measurements for Ta(5)/Ir(5)/$Gd_{24.3}Fe_{68.1}Co_{7.6}$(5)/Cu(5)/Pt(5) with out-of-plane field (left) and in-plane field (right)

The surprising result of the SOT switching in the absence of an external magnetic field has driven us to continue the magneto-transport measurements on this kind of sample but in 10 μm-wide Hall crosses in which the AHE signal is higher and the size makes easier the observation under the Kerr microscope. We studied a Ta/Ir/GdFeCo/Cu/Pt sample that exhibits mixed properties of the two previous ones since we have Ir as a seed layer but a composition further away from the magnetic compensation. In this case, the in-plane saturation field is much higher than in the 2 μm crosses (over 6000 Oe) but the coercive field remains below 50 Oe as shown respectively in figure 4.6 right and left. For this sample, we performed SOT switching measurements in two different 10 μm-wide Hall crosses next to each other. For both devices, the results are similar in terms of critical current density, maximum switching field and switching amplitude. However, we do observe the switching of the magnetization at very low field in figure 4.7 (b) and even without any field (a) which was not the case for the 2 μm Ta/Ir/GdFeCo/Cu/Pt. Thus, we can already conclude that the differences of saturation field or the changes observed in TEM micrographs between the two types of stacks do not play a role in the field-free switching.

In figures 4.5 (a), (b) and (c), the amplitude of the hysteresis loops at $H_X = 0$ seems to be roughly the same as the amplitude for higher fields before the decreasing due to strong in-plane field values. It is clear that it is not the case for the wider crosses. From the zoomed diagrams in figure 4.7 (c) and (d), we can tell that the amplitude for the loops around zero is definitely lower by a factor of 2 compared to the rest of the diagram. Moreover, the critical currents do not follow the same behavior and the loops seem to be shifted from the previous ones. This suggests that the reversal of the magnetization in the cross is incomplete and that the pulses nucleate magnetic domains in the device.

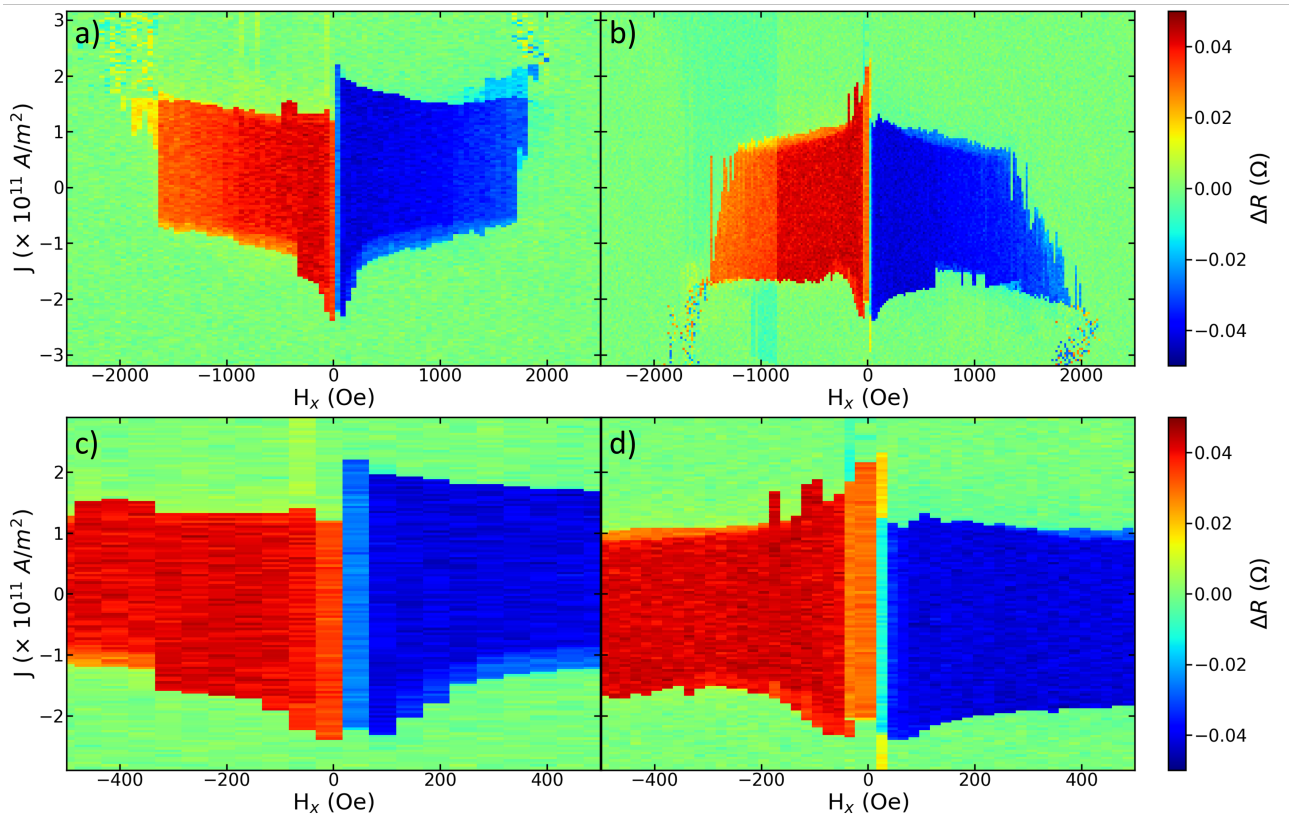

Figure 4.7: SOT state diagrams for two different 10 μm-wide Hall crosses (a) and (b) and their respective around zero zooms (c) and (d) for Ta(5)/Ir(5)/$Gd_{24.3}Fe_{68.1}Co_{7.6}$(5)/Cu(5)/Pt(5)

We now look at the hysteresis loops in details. For the loops obtained with an in-plane field of around $\pm$ 100 Oe (fig.4.8 (green) and (blue)), the amplitude matches with the out-of-plane AHE measurement (fig.4.6 (left)). As expected, the switchings are sharp and the sign of the loops depends on the direction of the external field.

In the absence of any magnetic field, we also obtain a perfect square hysteresis loop with sharp switchings (fig.4.8 (black)) that could suggest SOT induced reversal of the magnetization. However, the amplitude is half lower than the one expected. The high resistance state at 0.08 Ω and the low resistance state at 0.04 Ω repre-

sented by the red horizontal lines correspond to saturated states observable in the AHE measurements (fig.4.6). Intermediate magnetic states nevertheless exist that correspond to the resistance states at 0.055 Ω or 0.065 Ω confirming that the magnetization in the Hall crosses is not complete. Due to the aspect of the hysteresis loops of this partial reversal, one could question some field-free SOT switchings reported in the literature especially in sub-10μm devices where the difference of amplitude is less distinguishable.

Moreover, when on an intermediate state, the AHE signal decreases with the current showing that the magnetization state keeps changing whereas the AHE resistance is perfectly straight for saturated states. In the absence of field, in the case of the Hall cross presented in the diagram on the right in figure 4.7, we can observe the behavior reported by the red curve in the figure 4.8 (right). It exhibits, 4 switchings that allow the access to either full or intermediate states. To understand this behavior and the partial switching, we placed our samples on the Kerr microscope setup.

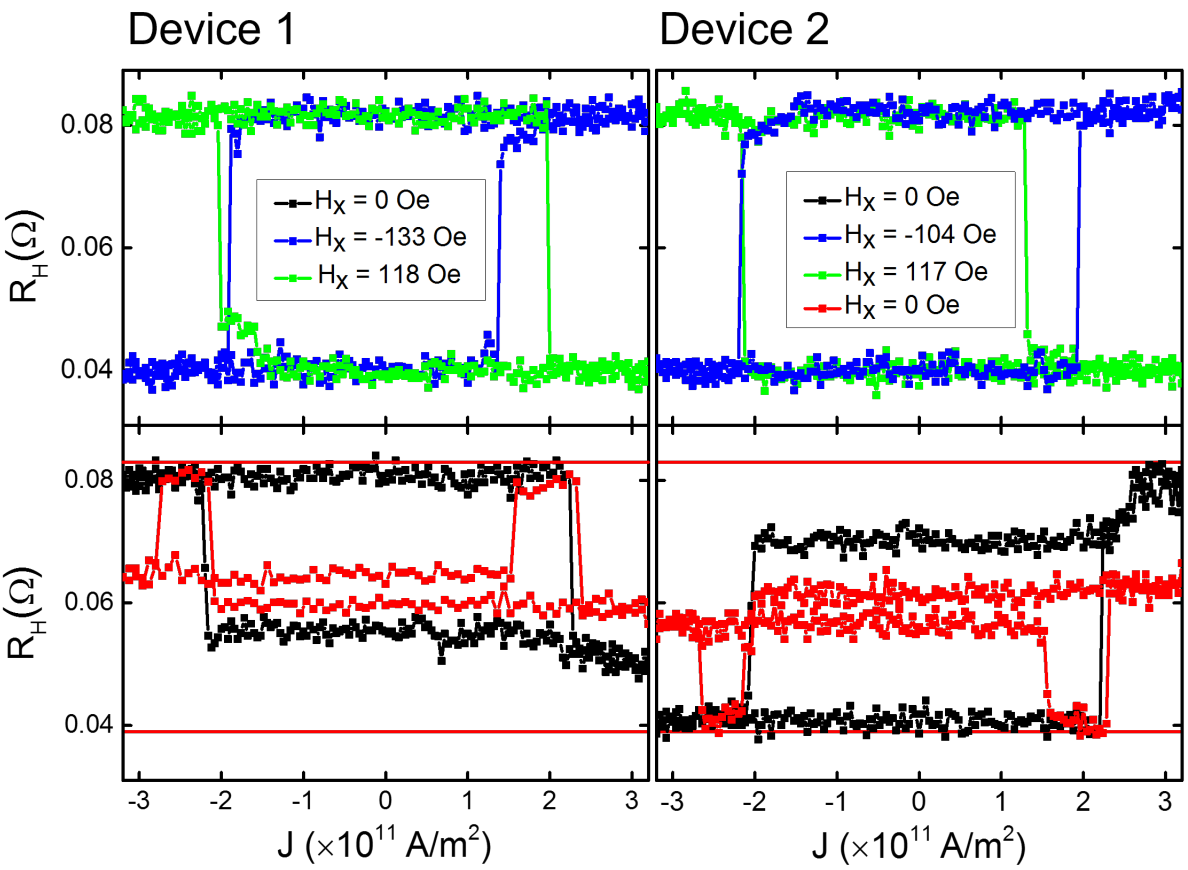

Figure 4.8: SOT switching hysteresis loops for Ta(5)/Ir(5)/$Gd_{24.3}Fe_{68.1}Co_{7.6}$(5)/Cu(5)/Pt(5) for two different 10 μm-wide Hall crosses at different in-plane magnetic fields. The red horizontal lines represent the saturated magnetization states

4.3.2 Zero-field switching under Kerr microscope

Results

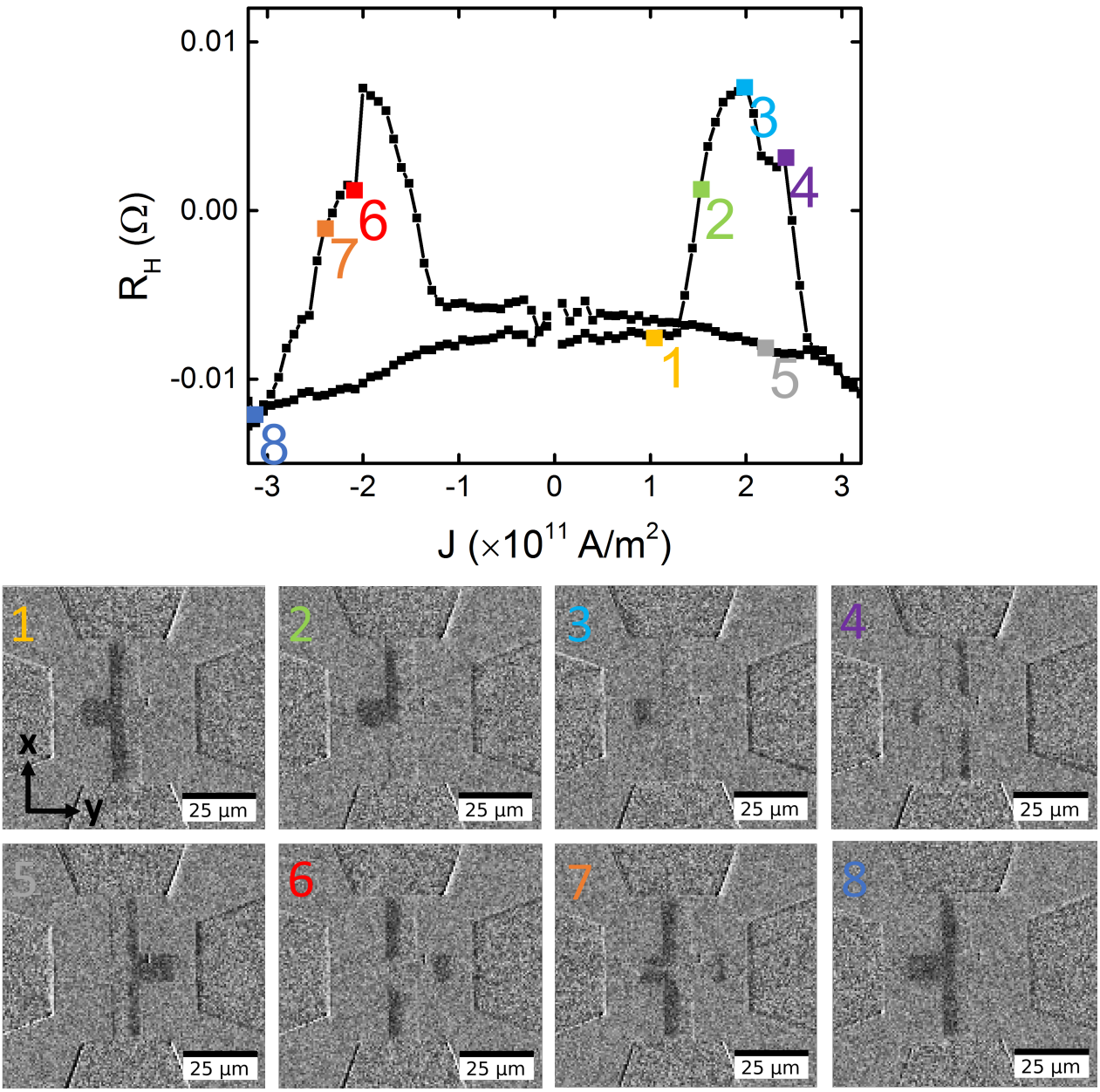

Figure 4.9: (Top) Hall resistance as a function of the current density without any magnetic field for Ta(5)/Ir(5)/$Gd_{24.3}Fe_{68.1}Co_{7.6}$(5)/Cu(5)/Pt(5) for a 10 μm-wide Hall cross. (Bottom) Kerr microscope images corresponding at different points of the curve

In this part, we show the results of the same measurements as in the previous part but performed under a Kerr microscope. This allows us to match each point of the hysteresis loops with a Kerr image of the device.

Also, in this configuration, our microscope setup does not have a magnetic coil installed avoiding any residual field. The instruments and the conditions are the same. We first reproduce the peculiar curve displayed in red in figure 4.8. The sample is saturated out of the plane by a manual magnet and the first pulse is at J = -3.2×10^{11} A/m^2. After this first pulse, we show that the intermediate state corresponds to a longitudinal half magnetic domain in the injection line of the cross i.e the x-axis on Kerr images (fig.4.9). The images (1) and (8) show the same magnetic configuration but the Hall resistance sightly increases between the two points. Because of the configuration of the measurement, the AHE signal is coming from the center of the cross and a very small part can come from current leaks in the reading leg i.e. the leg along the y-axis. Thus, the increase is due to a small displacement along x of the magnetic domain wall. The image (2) corresponds to a large increase of the resistance where we can see the progressive annihilation of the half domain. The third image (3) is associated to the maximum saturated level. In the center of the cross, the domain has completely disappeared and it only remains a small domain in the reading leg. For image (4), the resistance decreases and it corresponds to the nucleation of two new magnetic domains on the opposite edges of the current injection leg. On the other side, the size of the remaining domain keeps decreasing and it is completely shrinked in image (5). The new domains merge into a longitudinal domain on the opposite side of the leg compared to the initial domain. The resistance level matches with the same intermediate state because the occupied area by the domain is roughly the same. The image (6) summarizes the symmetric behavior, the domain in (5) is destroyed hence the resistance peak then in front new domains nucleate at the same equivalent regions as the first ones. The image (7) depicts the merge of the domain to form the longitudinal domain in (8).

Analysis

The fact that the domain nucleation occurs on one edge and on the other one when the polarity of the current is reversed would correspond to the effect of the Oersted field as shown in [76] in a 2-μm wide Pt(3)/CoFeB(0.6)/Pt(3). The nucleation is this publication induced by 25 μs pulses of J = 1×10^{12} A/m^2 and leads to a bidomain in the wire with the domain wall parallel to the direction of the current. When the direction of the current is reversed, the magnetization in the domain also reverses.

In our samples, it seems that we have the same phenomenon. Let us assume that the Oersted field induced by the first high pulse at J = -3.2×10^{12} is high enough to nucleate such a bidomain. The geometry of this case is shown in figure 4.10 (a) and it corresponds to the image (8) in the figure 4.9. Then, the pulse polarity is

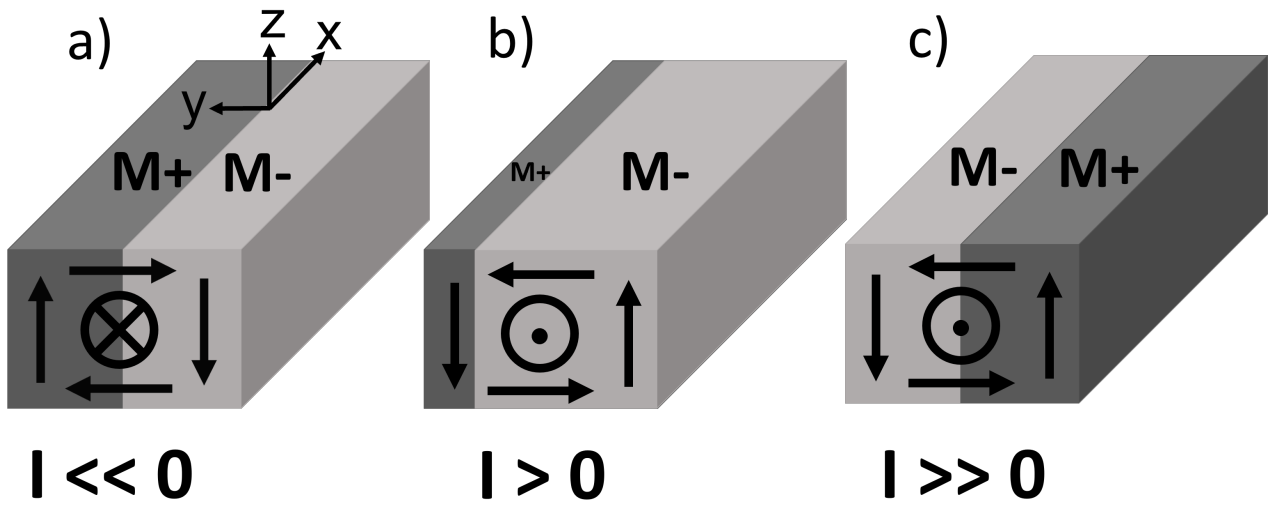

Figure 4.10: Schematics of the magnetic state in the Hall cross as a function of the current. The directions of the field are represented by the black arrows and the direction of the current is represented by the vector along the x-axis. M+ (M-) means that the magnetization is along +z (-z)

changed reversing the sign of the Oersted field which should be perpendicular to the film plane on the sides and in-plane at the center of the cross. Therefore, the Oersted field is now antiparallel to the moment of the domain and shrinks the present domain (fig.4.10 (b)) until a small one in the reading leg where the field is weaker as it can be seen in images (2)(3) in figure 4.9. When we continue to increase the current, the value of the field increases and is large enough to nucleate new domains (image (4) of fig.4.9). The geometry at this point is then symmetric to the initial one (fig.4.10 (c)). The Kerr contrast of the domains nucleated for $I < 0$ and $I > 0$ is the same since it is the same moment direction. We note that the nucleation is on the edge where the Oersted field is stronger but also on the etched part of the cross. Indeed, there is no nucleation at the intersection between the injection leg and the reading leg. It is probably because the etching introduce some defects of anisotropy reducing locally the nucleation field ($H_{nucleation}$). Both domains then propagate and merge together as it can be seen on image (7) at the center of the cross under the effect of the Oersted field and form the characteristic bidomain.

From the evolution of the Hall resistance, we can distinguish two important values for the Oersted field. One corresponds to the critical driving field (H_{drive}) that is high enough to move the domain wall and in our case it is for J > 1×10^{11} A/m^2. And the other is $H_{nucleation}$ for J > 2×10^{11} A/m^2. Because $H_{drive} < H_{nucleation}$, the domain is first moved out of the cross allowing the resistance to reach the maximum and then the nucleation occurs lowering the Hall signal. Due to the asymmetry of $H_{nucleation}$ when J > 0 and J < 0, in the considered

current range, we can reach the driving field without nucleating new domains for one polarity. This allows us to have a partial square hysteresis loop. In figure 4.11, we show the two possible paths for the AHE signal. From the intermediate state at 0.07 Ω shown in blue, we reach a saturated state at H_{drive}. At this point, either we continue to increase the current and reach $H_{nucleation}$ as shown in the orange and green images and we obtain the same double peaks signal (black curve) as in the figure 4.9 or we decrease the current and stay on the full state (red curve).

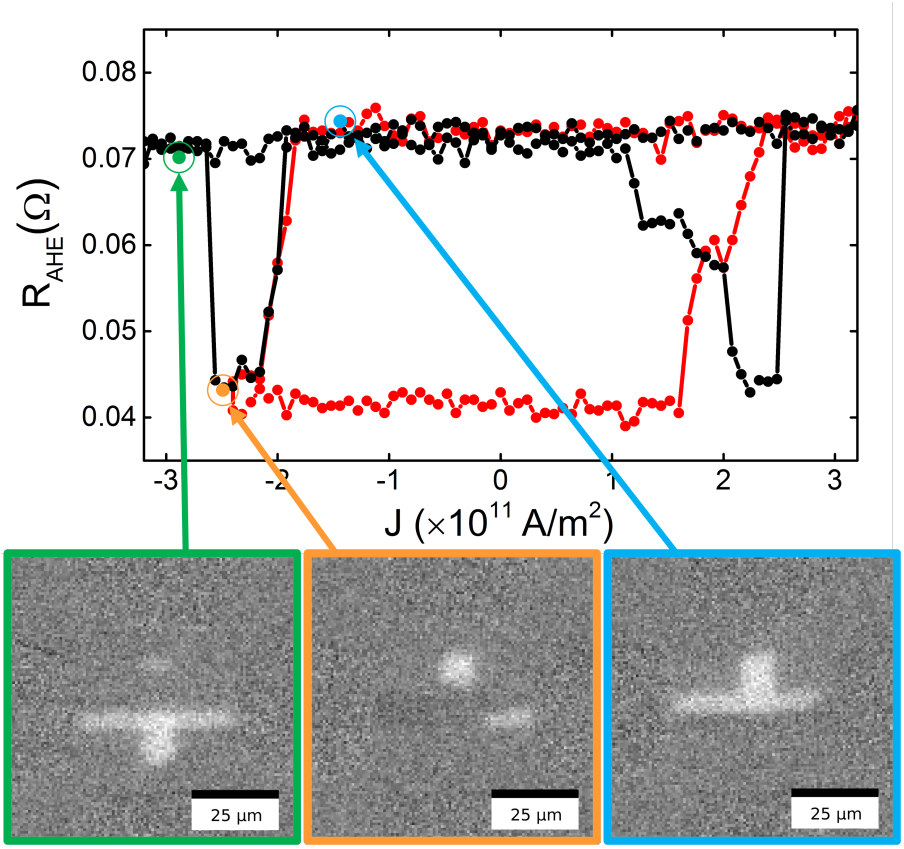

Figure 4.11: Hall resistance as a function of the current density without any magnetic field for Ta(5)/Ir(5)/$Gd_{24.3}Fe_{68.1}Co_{7.6}$(5)/Cu(5)/Pt(5) for a 10 μm-wide Hall cross for two different current ranges: from -3.2×10^{11} A/m^2 to 3.2×10^{11} A/m^2 in black and from -2.5×10^{11} A/m^2 to 3.2×10^{11} A/m^2 in red

The slight change of the intermediate states Hall resistance baseline observable in the figures 4.7 and 4.9 could result from the interplay of the domain equilibrium between the two OOP component of the Oersted field and the displacement induced by SOT[77].

Finally, when an in-plane field is applied, we obtain the full switching of the magnetization. As expected for SOT, the sign of the AHE loop depends on the direction of the field. Regarding the findings on the strong effect of the Oersted field, the SOT loops have to be affected by the field. If we take a look at them in the figure 4.7, we note that the switching current density is not always symmetric and can be importantly reduced. From

the red curve in the right panel, for the negative currents, the values of J needed to reach H_{drive} or $H_{nucleation}$ are superior to the critical current for SOT switching that is by consequence at the same value for $H_X > 0$ and $H_X < 0$ at J $\approx 2 \times 10^{11}$ A/m^2. On the other hand, for positive currents, we see with the red curve that J for H_{drive} is below 2×10^{11} A/m^2 to go to the saturated state at 0.04 Ω. The full switching for $H_X = 117$ Oe (from 0.08 Ω to 0.04 Ω) occurs exactly at the same current density whereas the one at $H_X = -104$ Oe with opposite sign is symmetric regarding the negative current. This reflects the effect of the Oersted field and that the SOT is combined with the Oersted field.

4.3.3 Oersted field simulations

To confirm the Oersted field induced switching, we performed Comsol simulations based on the analytical resolution of the Ampere's law. We take a wire of 10 μm x 50 μm x 25 nm that corresponds to the dimensions of one leg of the Hall cross. The 25 nm thickness is for a multilayer Ta(5)/Cu(5)/GdFeCo(5)/Ir(5)/Pt(5). The resistivities are the following[78]:

	Ta	Cu	Ir	Pt	GdFeCo[36]
Resistivity (nΩ.m)	131	17	47	105	3300

The first step consists in using Electric Currents in Shells (ecis) module with two boundary conditions: the current source with J = 3×10^{11} A/m^2 and the ground. This module gives us the distribution in the shells with their respective resistivities. The second step consists in estimating the magnetic fields generated by the current with the Magnetic Fields (mf) module. For this, the Ampere's law is solved with the current distribution obtained at the first step as a boundary condition. We obtain the classical distribution of the magnetic field when we inject a current in a wire (fig.4.12). The field loops around the wire. We have indeed a perpendicular to the film plane Oersted field at the edges of the wire with opposite orientation at each side and an in-plane Oersted field at the center of the wire. For our stack, for a current density of J = 3×10^{11} A/m^2, the magnetic field can reach an absolute value of 70 Oe which is larger than the coercive field (50 Oe) of the GdFeCo layer. This result is consistent with the observed behavior and his interpretation of a nucleation by Oersted field.

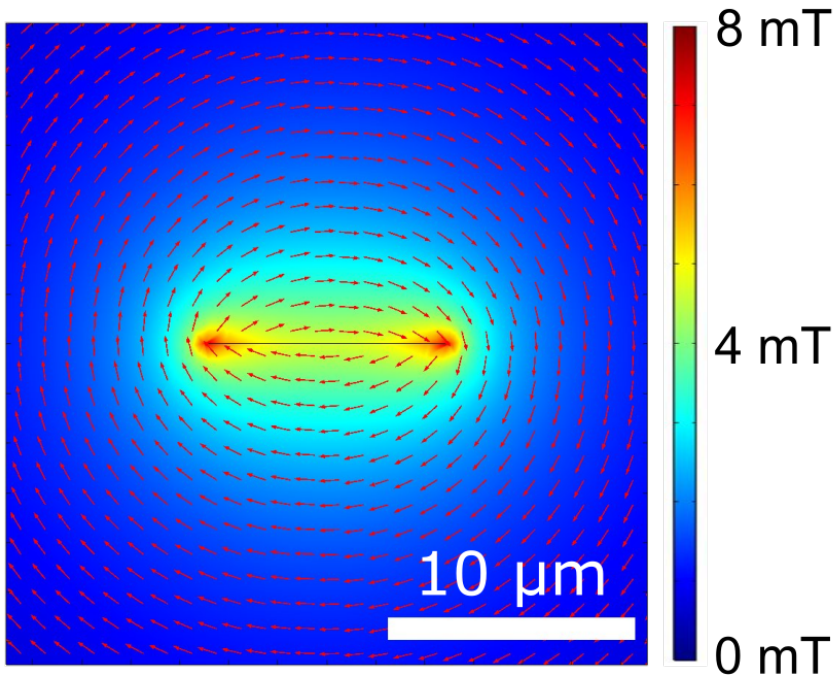

Figure 4.12: Cross-section of the Comsol simulation of the Oersted field generated by a current of J = 3×10^{11} A/m^2 in a Ta(5)/Cu(5)/GdFeCo(5)/Ir(5)/Pt(5) 10 μm x 50 μm x 25 nm wire

4.3.4 Hall cross with pillar

To avoid the effect of the Oersted field on our sample, we have tried an other geometry for the lithography consisting in a Ta(5)/Ir(5) Hall cross with a GdFeCo(5)/Cu(5)/Pt(5) pillar on the top and at the center of it (fig.4.13 (a)). The current should flow essentially in the Ta/Ir cross but the current in the pillar is enough to read the magnetic state even if the signal is blurrier. The first consequence of this device is the huge increase of the coercive field at 1200 Oe (fig.4.13 (b)). We do obtain a full SOT switching with the same amplitude as for the AHE measurement when an in-plane field is applied. However, we do not see any partial switching induced by Oersted field. Indeed, at zero field, the Hall resistance is constant (fig.4.13 (c)). With less current flowing through highly conductive metals such as copper and platinum, we could have imagined to lower the magnetic field. But due to the very large coercive field of the pillar, it is hard to conclude to the benefit of this geometry to avoid the current induced field. Moreover, for the following domain-wall propagation experiments, we are not interested in these devices. We will then pursue the measurements knowing that in our sample, the Oersted field cannot be neglected at all and it is in the range of the coercive field.

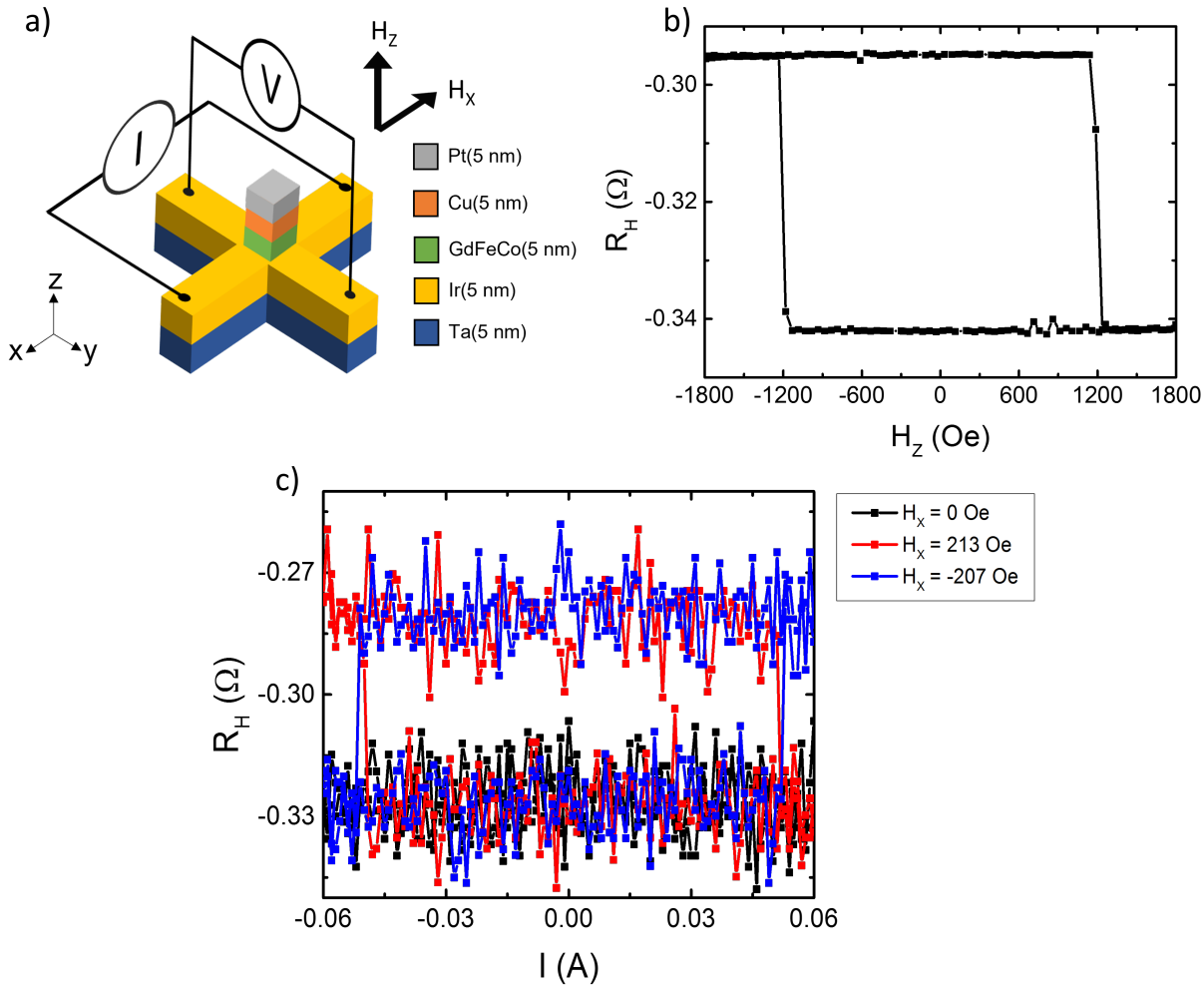

Figure 4.13: (a) Schematic of the experimental setup for the measurement of AHE and SOT switching in a pillar over a Hall cross. (b) Out-of-plane and in-plane hysteresis loop measured by AHE for Ta/Ir/GdFeCo/Cu/Pt. (c) SOT switching loops of the pillar for different external magnetic fields

4.3.5 Conclusion on the single layers

While measuring the SOT switching in our samples, we have observed a zero bias field switching feature. Despite what we may have thought after the first results, the difference of anisotropy does not seem to play a role, we can observe such a reversal in the absence of field either in Ta/Cu/GdFeCo/Ir/Pt or Ta/Ir/GdFeCo/Cu/Pt. The essential comparison of the loops amplitude revealed an incomplete switching of the Hall cross. After observation under a Kerr microscope, it is now clear that the underlying mechanism is the nucleation by Oersted field which explains why the sample with the higher coercive does not switch at zero field. This sample also exhibits higher current density threshold suggesting that the SOT switching is affected by the Oersted field. Moreover, the Oersted field leads to an asymmetry of the SOT loops.

4.4 Bilayer SOT switching

4.4.1 Antiferromagnetic coupling

The current-induced switching has also been investigated for the bilayer structure with the Ir thickness chosen for antiferromagnetic coupling. The measurement is the same as the one presented in subsection 4.1.3 in figure 4.3. Unfortunately, if the TM dominated transport properties allows to measure a Hall resistance even at the zero net moment, it is not the case for the SAF. Indeed, the two layers being antiferromagnetically coupled, the signal from the FeCo sub-lattice of each layer are compensated for AF states as it can be seen in figure 4.14 (a). The SOT switching loops of the SAF for different fields are shown in figure 4.14 (b) and (c). At in-plane field

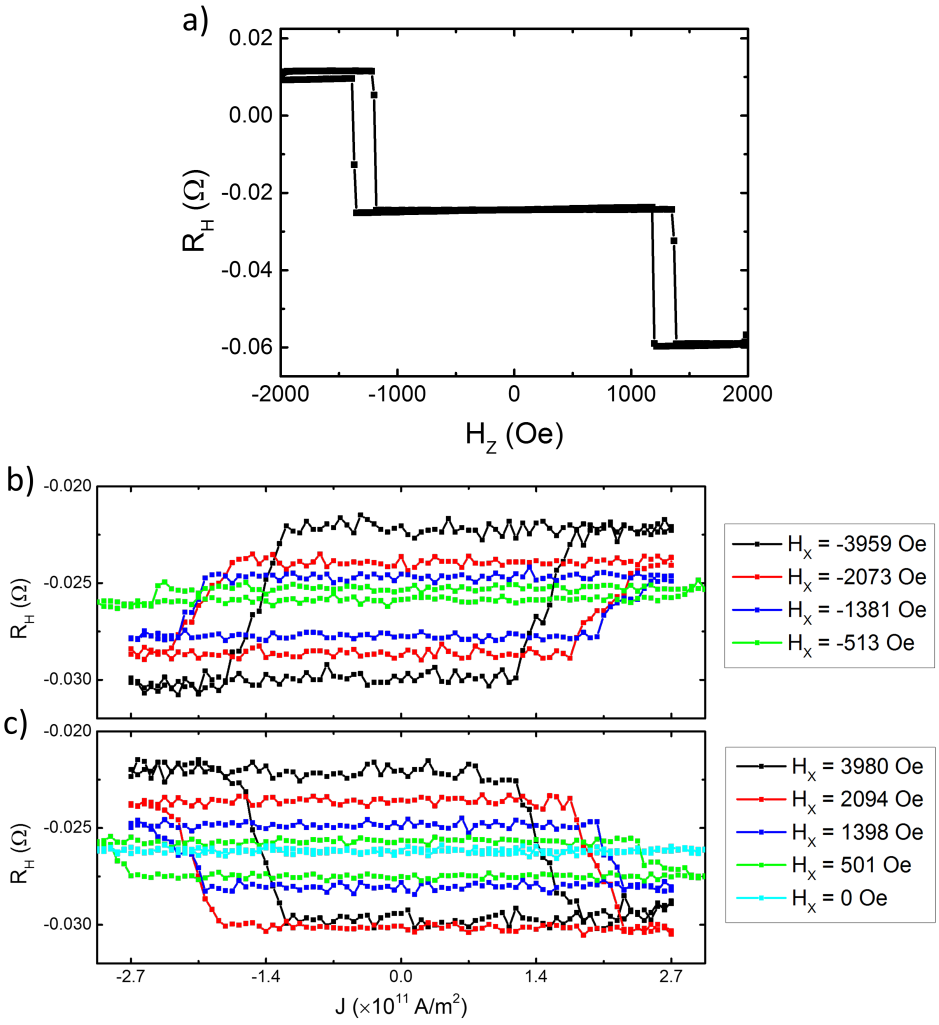

Figure 4.14: Out-of-plane hysteresis loop measured by AHE for the SAF Ta(5)/Cu(5)/$Gd_{26.4}$FeCo(5)/Ir(0.6)/$Gd_{24.3}$FeCo(5)/Cu(5)/Pt(5) (a). SOT switching loops of the SAF for different negative fields (b) and positive fields (c)

values of 500 Oe and above, the total moment of both FeCo sub-lattices tilts and is not compensated anymore. This has for consequence to open a cycle allowing us to observe SOT switching. One should note that the amplitude of the loops is not relevant here since it depends on the angle between TM magnetic moments. The switching occurs at higher current densities (at H_X = 500 Oe, $J_{switch} \approx 2.7 \times 10^{11}$ A/m^2 for the SAF versus $J_{switch} \approx 1.5 \times 10^{11}$ A/m^2 for the single layer) and the reversal of the magnetization is not as sharp as for the single layer. At zero field, it is not possible to detect the switching or any Oersted field induced nucleation via AHE.

4.4.2 Ferromagnetic coupling

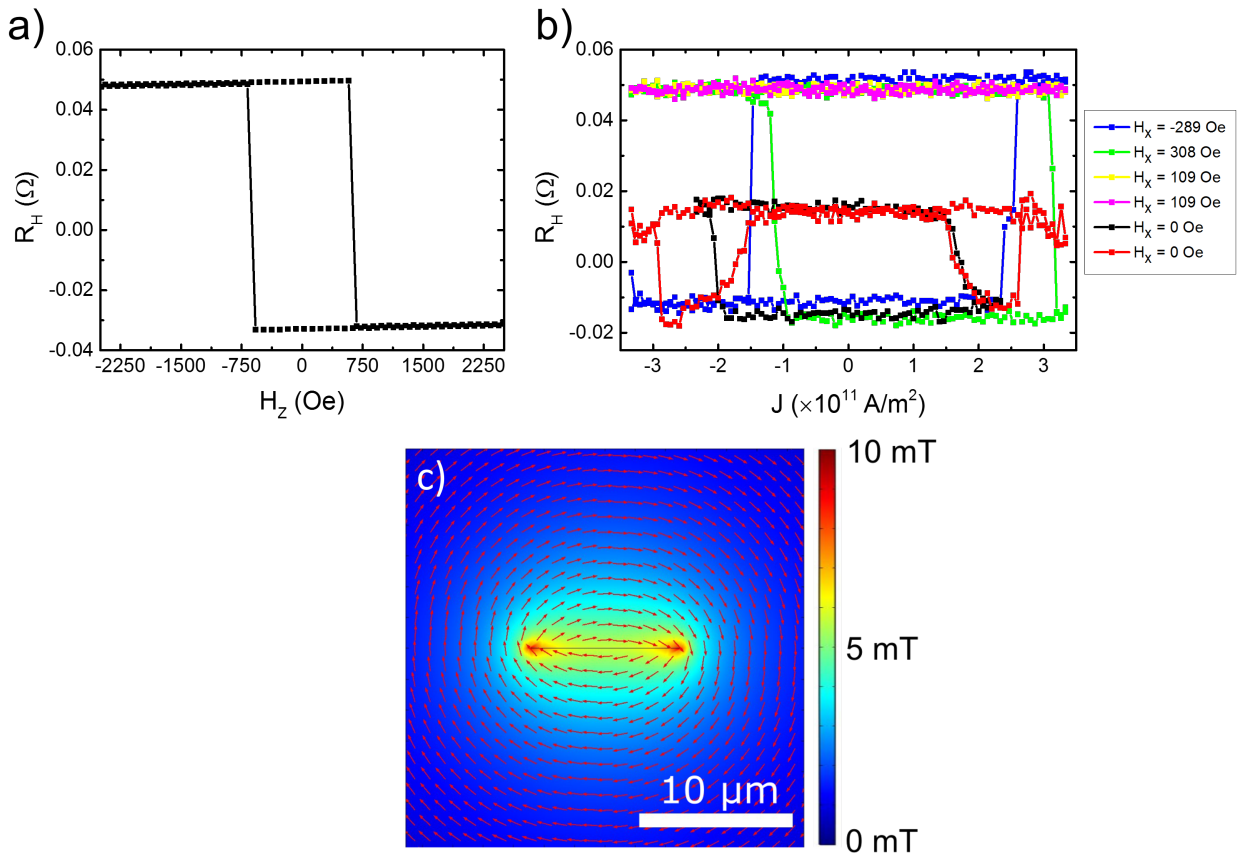

Figure 4.15: Ta(5)/Cu(5)/$Gd_{26.4}$FeCo(5)/Ir(0.4)/$Gd_{24.3}$FeCo(5)/Cu(5)/Pt(5) 10 μm-wide Hall cross AHE loop (a) and SOT loops for different in-plane fields (b). Comsol simulation of the Oersted field generated by a current of J = 3×10^{11} A/m^2 in a 10 μm x 50 μm x 25 nm wire

Finally, we show in the figure 4.15, the magneto-transport measurements for the stack equivalent to the SAF but with a thickness of iridium of 4 Å. The coupling between the ferrimagnetic layer is thus ferromagnetic. The AHE loop (a) reveals a much higher coercive field than for the single layer or the SAF, up to 750 Oe.

The Comsol simulation (c) estimates the Oersted field up to 100 Oe. By consequence, this sample should be immunized of the nucleation of longitudinal domain however we note that we find again the exactly same behavior as the one observed before (peaks of resistance and half amplitude square loop) in the absence of external field (b). This suggests that the heating and anisotropy defects on the edges lower sufficiently the coercive field. The full switching of the Hall cross occurs with the help of larger magnetic fields than seen before. We can only observe SOT switching above $\pm$300 Oe where we measure the right amplitude with the sign of the loops depending on the sign of the field.

4.4.3 Conclusion on the bilayers

Whether with antiferrimagnetic or ferromagnetic coupling, the bilayers are not more efficient for SOT switching even the needed current density is of the same order of magnitude. The magneto-transport measurement is not straight-forward for the SAF since the TM-dominated AHE signal is compensated. It would be interesting to measure more uncompensated samples either by changing the composition or the temperature. With the ferromagnetic coupled sample, we find a behavior similar to the single layers regarding the SOT switching with the only difference that the reversal vanishes at higher field values. However in the absence of field, the Oersted field nucleation still occurs and we are able again to obtain square loops with reduced amplitude. For the SAF, at zero field, we cannot distinguish one AP state from the other, but as we will see in chapter 5 under Kerr microscope, we do observe the effect of the Oersted field whereas we could have expected a lower Zeeman due to the small net moment.

Since the properties of the bilayers seem to not bring interesting advantages about current-induced switching, we focused on the domain-wall propagation.

Chapter 5

Domain-wall propagation

The main objective of this thesis is the high speed displacement of domain-walls (DW) which are nanoscale extended region where the magnetization is progressively re-oriented between two domains of opposite magnetic orientations. On one hand, GdFeCo is an interesting material in which has been already measured high velocities and that can exhibit angular momentum compensation which drastically changes the dynamics. On the other hand, using ferromagnetic materials, groundbreaking results have been obtained in SAF. Indeed the antiferromagnetic coupling seems to overcome some limits of the propagation in single layers. Moreover, low magnetization seems to be one of the key feature to achieve high velocity DW motion. We propose here to take a look at the DW displacement in samples that combine at the same time the ferrimagnets and the SAF properties. These systems present high fundamental interest since we could observe the effect of magnetization, angular momentum and net moment compensation in a single sample.

5.1 Domain-wall physics

The displacement of a magnetic domain-wall using current is actually something that came before the emergence of spintronics and that inspired the idea of STT. But with the newly understood phenomena to manipulate the magnetization, some ideas of new memory devices appeared such as domain wall devices based on an old concept of magnetic bubble memories[79] for which a very simple model was already developed to understand the dynamics of domain-walls. A 1D toy-model is widely used to describe the DW motion. Initially for STT, it allows us to well understand the behavior of DWs under the effect of torques. Directly derived from LLG equa-

tion, the model[80] consists in two coupled differential equations describing the time evolution of the position of the DW and the tilt angle of the center spin of the DW if we assume a constant profile in the wall:

$$\dot{\phi} + \alpha\dot{q}/\Delta = \gamma_0 H_a + \beta u/\Delta, \qquad \dot{q}/\Delta - \alpha\dot{\phi} = \gamma_0 H_K sin\phi cos\phi + u/\Delta \tag{5.1}$$

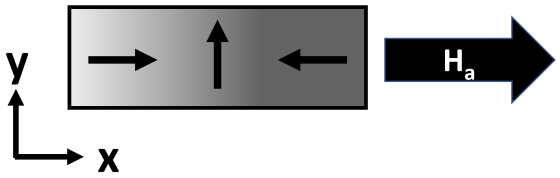

Figure 5.1: Schematic of the considered geometry for the 1D model for a transverse domain-wall with field applied along the x-axis

where ϕ is the wall magnetization angle, α the Gilbert damping constant, q the wall position, H_a the applied field, β the so-called non-adiabatic STT parameter, $\Delta = \sqrt{A/K}$ the DW width and H_K the anisotropy field defined as $H_K = 2K/(\mu_0 Ms)$. Finally u represents the role of the current as an effective velocity defined as $u = \frac{g\mu_B PJ}{2eM_S}$ with g the Landé factor, μ_B the Bohr magnetron, J the current density, P the spin polarization and e the elementary charge.

In figure 5.2 is shown the schematic results for the model in a case of an external applied field (left) or a current (right). For the case of a drive field, we can distinguish two regimes. At low values, the angle of the DW is tilted out of the easy axis plane but it reaches an equilibrium maintained by the internal torque. The velocity of the DW increases linearly as a function of the field until a certain point where the velocity collapses. This peculiar point is called the Walker breakdown and corresponds to the precession of the tilt angle. At high field values, the evolution of the velocity with the field is again linear but in a precessional regime.
For the dependence with the current in the case of STT, we can distinguish three cases. For pure adiabatic STT, when $\beta = 0$, the DW starts to move only above a certain threshold in a precessional motion. For $\beta > 0$, we find again both regimes as for the field driven displacement.
The perfect picture depicted by the model does not take in account the pinning that can exist in real materials. Indeed the movement of the DW can be affected by all sort of defects in the sample or the micro-structure. This will induce a field or current threshold before the DW starts to move then the DW jumps from a pinning site to an other, this is called the creep regime[81,82]. For higher values of field or current, the motion is freed from the pinning and recover the behavior described by the $q - \phi$ model, this is the flow regime (fig.5.2 (right red)).

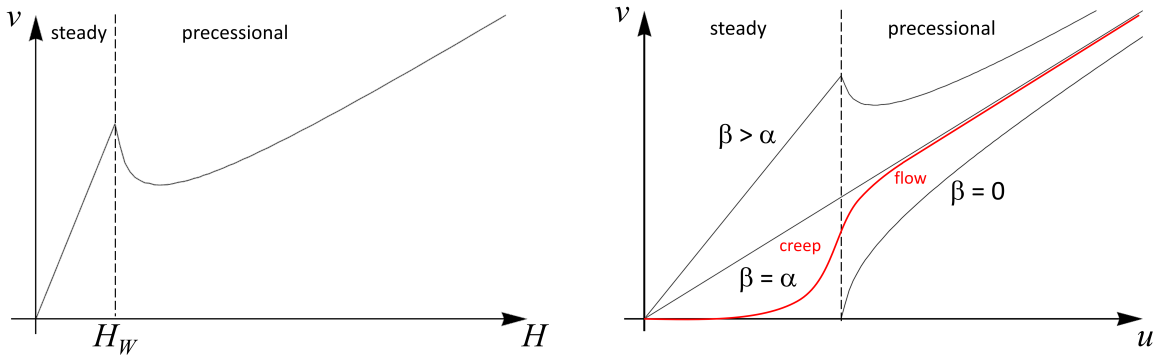

Figure 5.2: Schematic of the domain-wall velocity as obtained from the 1D-model (left) as a function of the field and (right) as a function of the STT current. In red is represented the DW velocity in high pinning material

Historically, the first studies on DWs were on in-plane domains. In this case, the DWs are wide because of the low magnetic anisotropy of the studied materials. Later, domains with PMA have been preferred due to their higher density. These perpendicular domains are narrower and can take two different forms: Bloch or Néel depending on the properties of the material or the interfaces. In the Bloch configuration (fig.5.3 (bottom)), the moments in the DW rotate in parallel to the wall plane whereas for a Néel DW (fig.5.3 (top)), the rotation occurs perpendicularly to the wall plane.

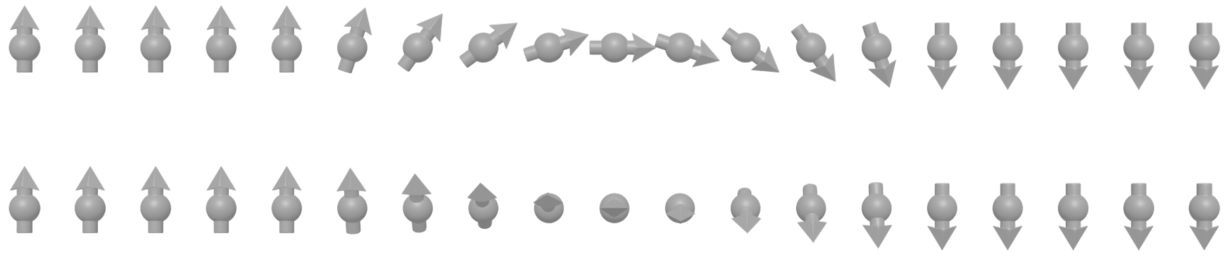

Figure 5.3: Schematic representation of two different types of domain-walls between up and down magnetization domains with Néel wall (top) and Bloch wall (bottom)

More recently, it has been found that SOT driven motion is more efficient and meets the needs for optimized memory devices[83]. In addition, the interfacial Dzyaloshinskii–Moriya interaction (DMI)[84,85], defined for neighboring spins $S_{1,2}$ as $H_{DMI} = -D_{12}.(S_1 \times S_2)$, stabilizes chiral domain wall texture such as Néel ones which has been proven as the most effective DW with SOT[86]. The magnitude and sign of D_{12}, the DMI parameter, are determined by the interface between the magnetic layer and the heavy metal with strong SOC. This new mechanism[87–92] that combines SHE and Rashba effect relies on the the Slonczewski-like torque that vanishes in the case of Bloch DWs. The 1D-model can be modified in order to consider the effect of the spin

current generated via SOT by adding an effective magnetic field[73,86]. SOT-driven DWs motion avoids the Walker breakdown issue and improves the velocity but also implies a tilt of the magnetization that limits the effectiveness and thus other ideas have been explored.

For DWs motion induced by STT or external magnetic field, it as been calculated that the SAF structure should reduce and even eliminate the effect of the Walker breakdown proportionally to the total net moment[93]. For SOT-induced motion, the SAF with two ferromagnetic layers has been proven to be also more efficient as a function of the total net moment compensation[65]. In ferrimagnets, high velocities has been shown as well but in function of the angular momentum compensation as presented in the next section.

5.2 State of the art of the magnetic domains propagation in micro-wires

Proposed 15 years ago[94,95], the racetrack memories are magnetic nanowires in which data are stored in sequences of magnetic domains that can be moved back and forth using spin-currents to bring them to read or write devices without physically moving any part of the device. The development of racetracks went through several phases[95]. Initially, the principle has been demonstrated in permalloy nanowires with an in-plane magnetization (fig.5.4 (a)) and a domain wall velocity of 100 m/s has been measured. But with this first test, two major issues have emerged, first the domain width was quite large because it depends on the shape anisotropy and secondly the domains tended to expand under current. The second version of the racetrack was made of Co/Ni superlattices nanowires. This version exhibits domains with a perpendicular magnetic anisotropy (PMA) resulting in narrower and robust domains (fig.5.4 (b)). But the velocity of the domains were the same as in the first version. In 2011, the role of the interfaces on the velocity and the chirality of the domain walls has been highlighted. As seen in the previous part, it is shown that a heavy metal layer under the magnetic layer set the chirality of the domain walls by DMI and will create a spin-current by SHE and Rashba. With all these effects combined, a velocity of 350 m/s has been measured (fig.5.4 (c)). In this chiral racetrack using SOT, the direction of the domains displacement depends on the spin hall angle of the adjacent layer[73] and can be in the direction of the current which is not the case for the two previous versions where the DWs are driven by STT. Now, some problems still have to be solved. In the third version of the racetrack, the velocity has been increased but it need to be higher in the idea to create a memory device. Moreover, the stray field coming couples neighbor domains and limits their density. The solution proposed is the synthetic antiferromagnet racetrack which consists of a nanowire made of two magnetic layer antiferromagnetically coupled (fig.5.4 (d)).

The SAF version of the racetrack has been already tested successfully. The demagnetizing field is reduced and a novel chiral exchange-coupling torque is observed that is directly proportional to the strength of the antiferromagnetic exchange coupling between the two sub-layers allowing high velocities up to 1000 m/s. The DW velocity increases as the net moment of the SAF decreases to zero[65].

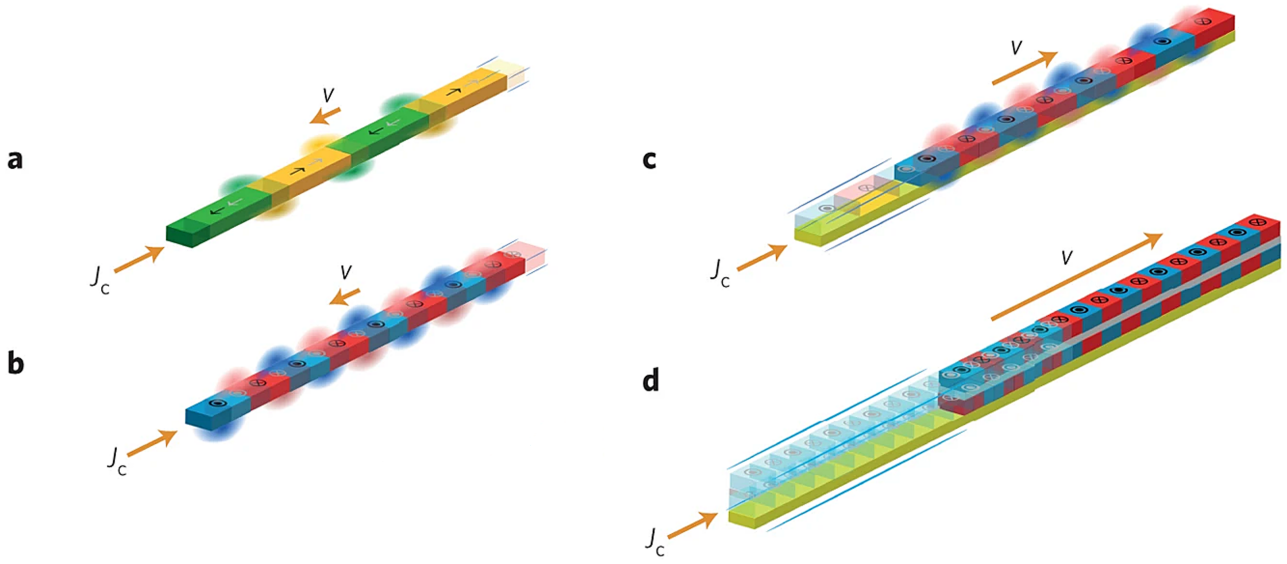

Figure 5.4: Evolution of racetrack memory from [95]. Schematic of (a) an in-place racetrack (b) an out-of-plane racetrack (c) a chiral racetrack (d) SAF racetrack

GdFeCo domain-wall propagation

Among the emerging fields in spintronics, the antiferromagnetic materials dynamics exhibits as well interesting properties for DW propagation. However, antiferromagnets with perfectly compensated magnetic sub-lattices are hard to probe and manipulate. As seen before GdFeCo as a ferrimagnetic RE-TM alloys has equivalent properties to the antiferromagnets via the coupling of its sub-lattices but its transport properties are dominated by the TM allowing easier manipulation. Additionally, the angular momentum compensation temperature (T_{AC}) and the magnetic compensation temperature (T_{MC}), that are different (with $T_{MC} < T_{AC}$) for GdFeCo, are tunable and interesting properties for DW motion. If T_{MC} changes the net magnetization, T_{AC} affects the dynamics. Indeed, the effect of T_{AC} has been observed in GdFeCo for field-driven DWs motion allowing estimation of the damping parameter[96] for example. Moreover, at this critical temperature has been associated a peak of the velocity[97] showing that antiferromagnetic spin dynamics is achievable in ferrimagnets. Since at T_{AC}, the net magnetization is not zero, it is still possible to manipulate the magnetization with an external field.

Under current, the same peak velocity has been measured by field-assisted STT in thick GdFeCo layers[98]. By SOT, high velocities are reached (> 700 m/s) for Pt/GdFeCo stacks exhibiting Néel DW profile[99]. Moreover, at T_{AC}, it is confirmed that the tilt induced by SOT vanishes maintaining Néel DW.

5.3 Experimental results

In order to investigate the DW motion in our GdFeCo samples, we use the same Kerr microscope setup as the one used before. Under microscope, we can see the behavior of the magnetization in the full film with an external applied magnetic field. For the GdFeCo in the range of composition of our study, for the single layer, a magnetic domain nucleates at one edge of the sample and then propagates as a single huge domain through the sample. The pinning seems limited but some defects are visible (fig.5.5 (a)).
In the SAF structure, the DWs between the AP+ and AP- states is smoother than the DWs in the single film. The propagation is less sensitive to the defects and the wall does not pin as much as for the monolayer (fig.5.5 (b)). One possible explanation is the exchange coupling between both layers, indeed if one defect pins the DW in one layer, the propagation is maintained by the other layer and drives the pinned DW. On the other hand, the AP to P domains do not nucleate at the sample edges but emerges from different points of the film. Moreover the AP/P DWs are very rough probably because the P states in the SAF go against the RKKY exchange and require a high field (fig.5.5 (c)).

Regarding the propagation in the full film as well as the presence of heavy metal layers next to our ferrimagnetic layers in our samples, we have all the ingredients to expect efficient SOT DW motion.

5.3.1 Propagation in micro-wires

We now use the 10 μm $\times$ 200 μm wires of our lithographed samples to study the DW motion under the effect of current pulses.

Nucleation

To store a magnetic domain in our device, the wire is first saturated with a strong permanent magnet then the objective is to nucleate a magnetic domain in the wire. Because the driving field in our sample is lower than

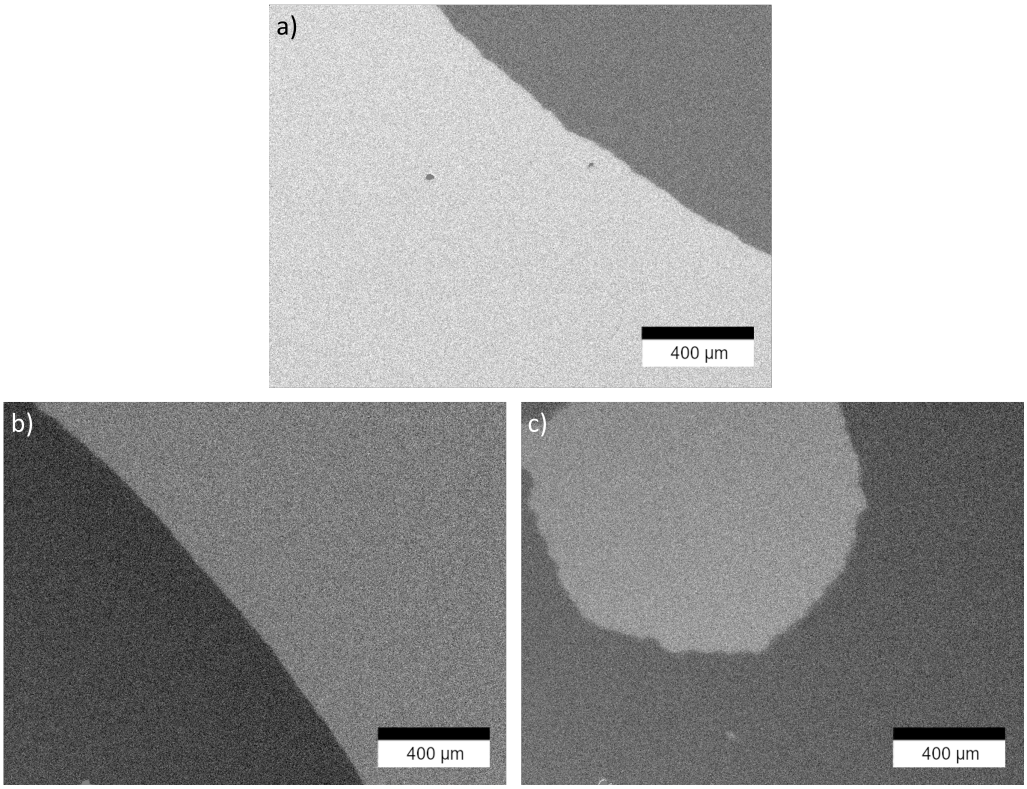

Figure 5.5: Wide-field Kerr microscope of magnetic domain-wall in (a) a M+/M- GdFeCo single layer, (b) a AP+/AP- SAF bilayer and (c) AP/P SAF bilayer

the coercive field and due the micrometer scale of our device, the nucleation by an external field leads always to a full reversal of the wire. One solution is the nucleation by Oersted field of a longitudinal domain all along the wire with a single 100 μs and 80 mA pulse using the properties of our samples seen before (fig.5.6 (top)). Finally, the domain is moved to its initial transverse position using the permanent magnet (fig.5.6 (bottom)).

Direction of propagation and chiralities

Once the transverse domain is placed in the track, successive pulses or train of pulses of 100 μs of a same current amplitude are sent. After each train or pulse, a Kerr image is recorded, the position of the DWs in the wire is then reported. The measurement is thus static and includes acceleration and deceleration times.
In figure 5.7 is shown the propagation of DWs in a Ta/Ir/GdFeCo/Cu/Pt track. The DWs, independently of the direction of the current or the type of DW (up-down or down-up), moves against the electron flow. This automatically disqualifies STT as the responsible mechanism and indicates that DWs are driven by SOT. Their direction of propagation could be consistent either with left-handed chirality of Néel DW and the sign of SHE[73] of the Ir seed layer or with right-handed Néel DWs and the spin Hall angle of the top Pt layer. Indeed, it has

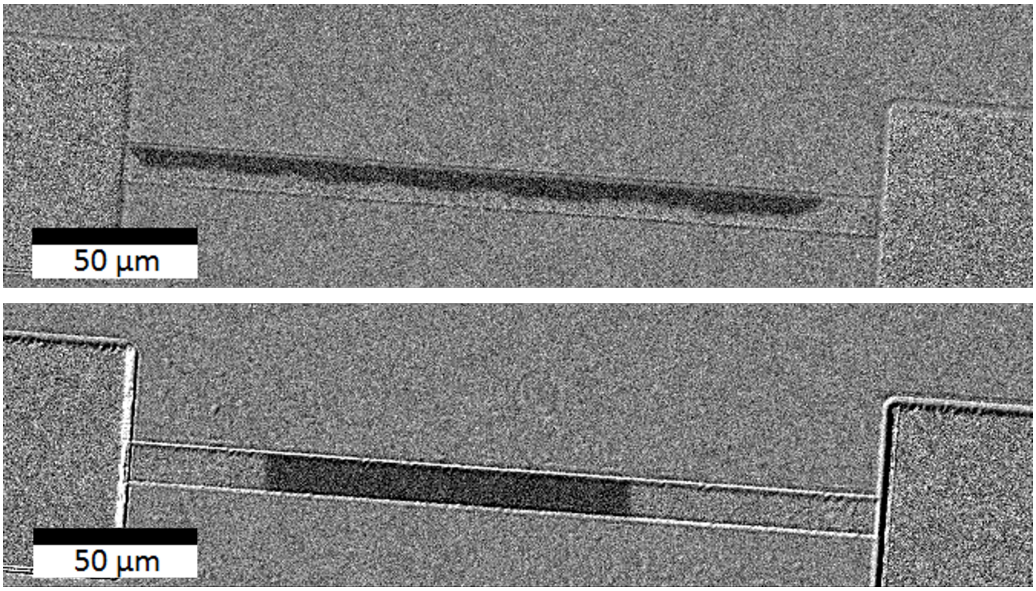

Figure 5.6: Microscope Kerr images of a 10 μm-wide wire after (top) the nucleation of a longitudinal domain by Oersted field and (bottom) the re-orientation of the domain with an applied magnetic field

been found spin Hall angle sign are the same for Pt and Ir[74] and as seen before the spin diffusion length in copper is greater than 5 nm, thus the Pt top layer is supposed to counter the torque induced by the spin current from the Ir. Concerning the DMI that sets the chirality, either for Ir/Fe[100,101] and Co/Ir[102], the sign of D is still controversial. Moreover, in the case of the SAF, the RKKY exchange coupling has to be taken in account and could take over the DMI. One has to be cautious before concluding with these results alone.

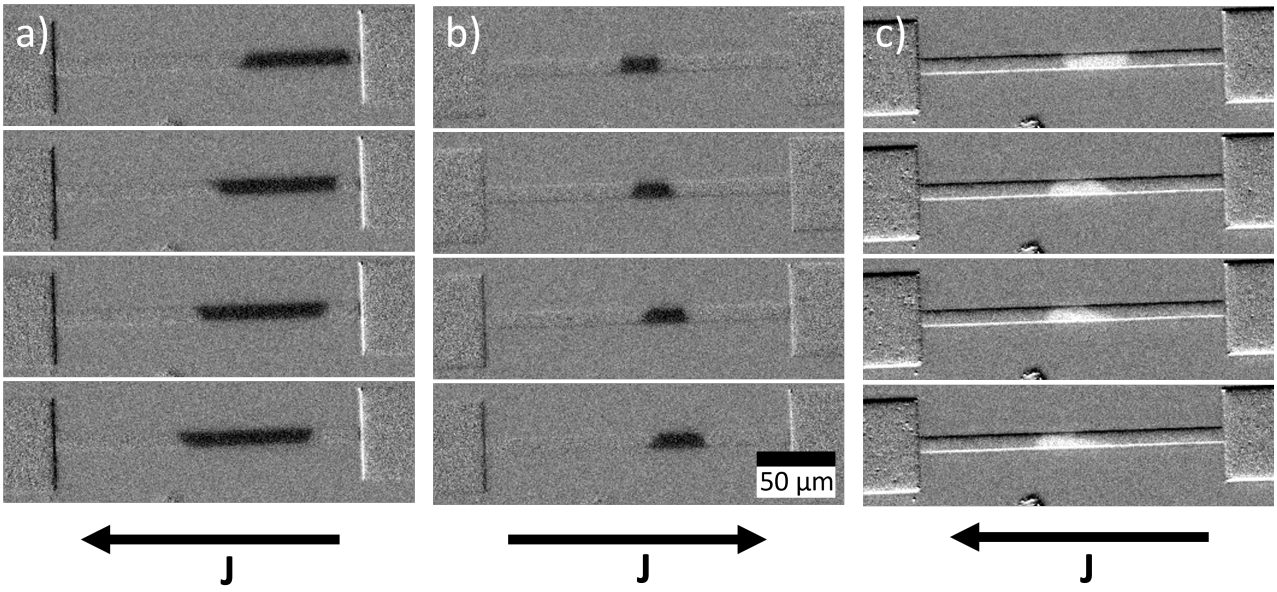

Figure 5.7: Kerr images of a DW driven by 35mA pulses of 100 μs in Ta/Ir/GdFeCo/Cu/Pt for two different directions of the current (a)(b) and for a reverse magnetization domain (c)

Along with Ir/GdFeCo/Cu/Pt, we also have studied three other kinds of samples: the Ta/Cu/GdFeCo/Ir/Pt single layer, one SAF sample and one GdFeCo bilayer with ferromagnetic RKKY coupling. The velocities are reported in figure 5.9. We choose the convention that the velocity is positive (negative) when the DWs move towards (away from) the positive electrical contact. The directions of propagation are summarized in figure 5.8. First, we notice that for Ta/Cu/GdFeCo/Ir/Pt, the DWs moves in the opposite direction of the Ta/Ir/GdFeCo/Cu/Pt DWs. In that case, it is then along the electron flow and it can correspond either to STT or SOT driven direction. But our samples are very thin and we demonstrated SOT dominated motion before, one can assume that STT is not the mechanism involved here. Moreover, Ta and Ir have opposite spin Hall angle and thus their torques combine. This would tend to consider a left-handed Néel DW.

Logically, the DWs in the SAF move as well against the electron flow. Indeed, the lower ferrimagnetic layer of the SAF corresponds to Ta/Cu/GdFeCo/Ir with only 6 $\AA$ of iridium that should not contribute to the spin current generated in our stacks. If, as seen before, we assume an anticlockwise chirality, the top layer of GdFeCo should have the same configuration by antiferromagnetic coupling and the spin current from Pt should drive the domain in the same direction as for the bottom layer.

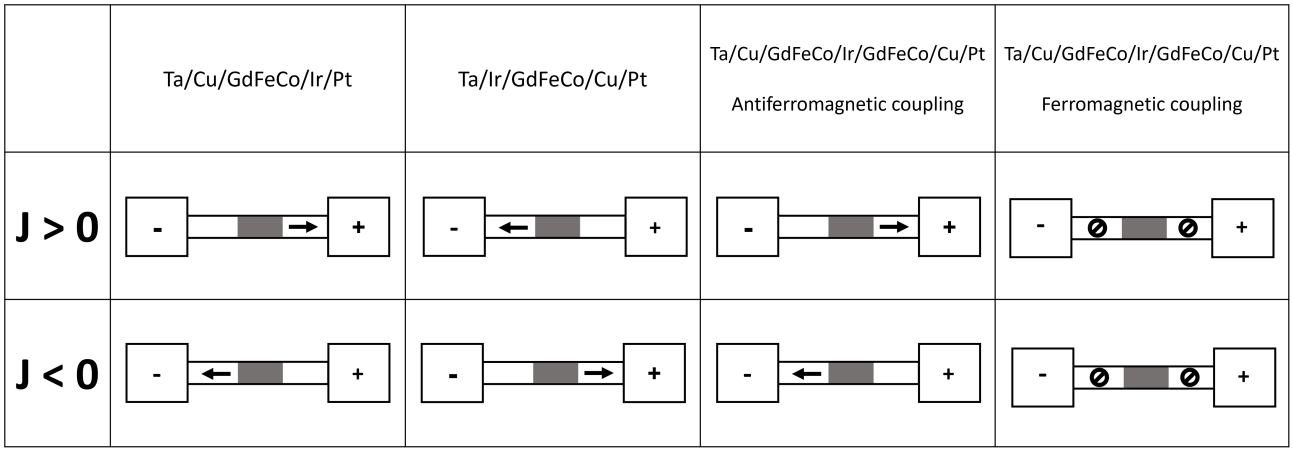

Figure 5.8: Summary table of the direction of propagation as the function of the sample and the current direction

Surprisingly, the DWs in the same stack with ferromagnetic coupling do not move at all. The coupling is not supposed to change the direction of propagation since it is defined by the chirality and the spin Hall angle and the iridium thickness of 4 $\AA$ should not affect the structure. But the main parameters changes here are the net total moment that goes from almost zero to the addition of the moment of both layers and the coercive field that is way higher than in the single layers. As seen in chapter 4, the SOT is not as efficient as in the other samples and higher currents are probably needed to overcome the threshold so that the DWs start to move which is impossible as it is explained in the next part.

Velocities and tilt angles

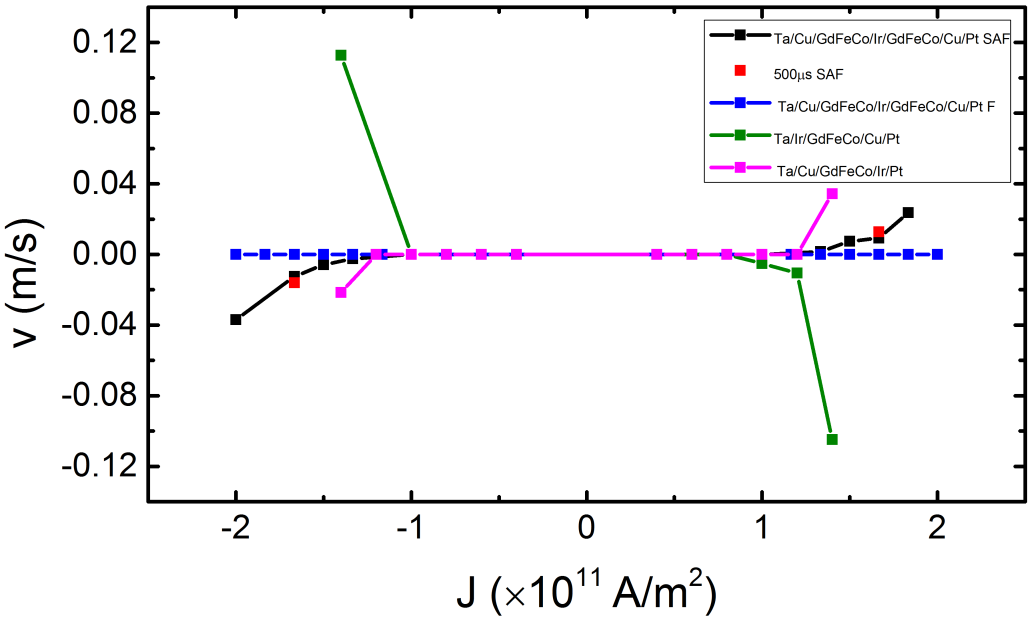

Figure 5.9: DW velocity as a function of the current density for 100 μs pulses in different stacks. The velocity is the mean value of the displacement for dozens of pulses divided by the pulse duration

All the points in figure 5.9 are calculated from images where the structure of the domain is maintained. For all the stacks, no motion is observed below a current density of J = 1×10^{11} A/m^2. Then, it is high enough to overcome the pinning and the DWs start to move. In the studied range of current, the motion is still dominated by the creep regime, and it happens that the size of the domain change due to the pinning of one DW. The velocities are in same order of magnitude for the different samples. The measured velocities are independent of the number or the duration of the pulses. Unfortunately, as one might expect, the Oersted field that allows us to easily nucleate domains in the device also interferes with the DW propagation. The effect of the Oersted field prevents us to go further in the analysis. From the most stable sample which is the SAF, we can tell that the behavior is the one expected: a depinning current threshold and then an increase of the domain wall velocity. However, the Oersted field generated by the pulses, in the range of the driving field, tilts both DWs of the domain towards the longitudinal direction (fig.5.10 (a)) as it has been observed in a couple of publication in (Ga,Mn)As wires[103,104]. Since it is an effect of the Oersted field, the reversal of the current polarity has for consequence to tilt the DWs of the opposite angle (fig.5.10 (b)). During the pulse, the domain is deformed and acquires the non-equilibrium shape as in the bottom image in figure 5.10 (b)) before returning to the oblique DW. In our sample, the effect of this field is dramatic, when the Oersted field reaches the respective coercive

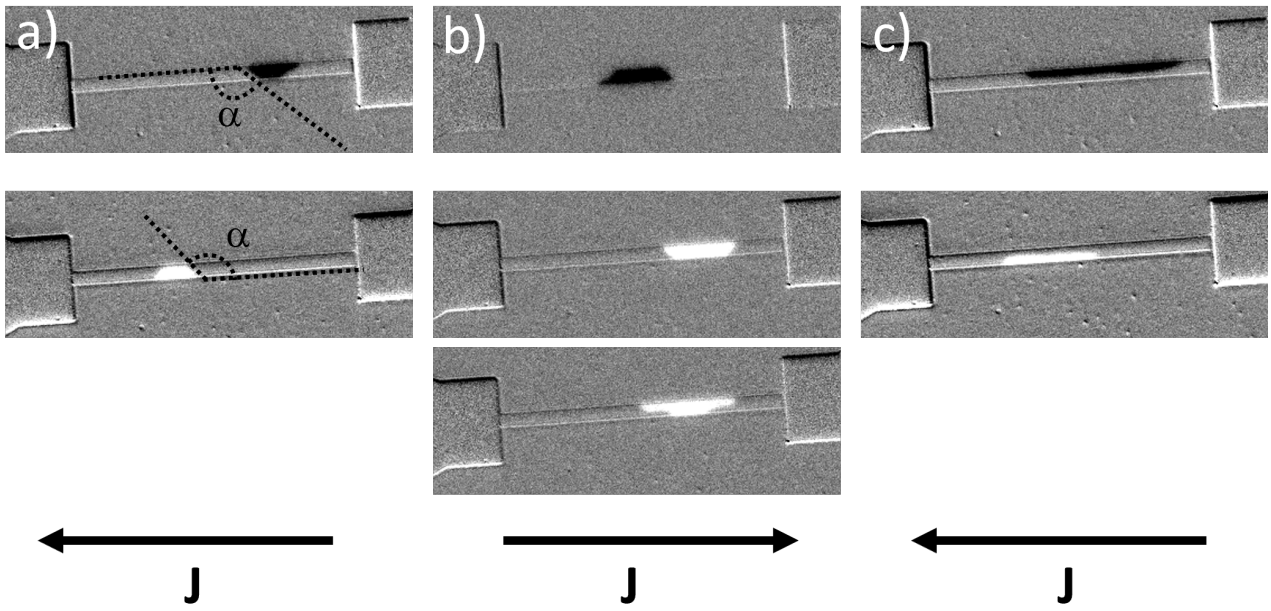

Figure 5.10: Kerr images of the DW obliqueness in Ta/Ir/GdFeCo/Cu/Pt after pulses of 100 μs and (a) 50mA (b) -50mA (bottom image has been taken during a pulse) (c) 60 mA

field of each sample, corresponding to the values reported in chapter 4, the domain splits in a half domain with a longitudinal DW (fig.5.10 (c)). As a consequence, it is impossible to increase the current density to the values necessary to achieve >100 m/s velocities that can be of one greater order of magnitude[99,105] in this kind of sample. One might note that despite its large values, the Oersted field does not dominate the propagation since the direction of the displacement does not depend on the initial magnetization configuration of the domain.

In figure 5.11 are reported the angle of the domain wall as a function of the current for the different stacks. The convention to measure the angle α is shown in figure 5.10 (a), an angle of $\alpha = 90°$ corresponding to a DW normal to the current injection direction. We notice that the evolution of the angle follows the same tendency for all the samples but their sensibility to the Oersted field seems to differ. The synthetic ferrimagnet bilayer and the Ta/Cu/GdFeCo/Ir/Pt have the same linear increase of the obliqueness until the nucleation Oersted field is attained. For Ta/Cu/GdFeCo/Ir/Pt, the values of the tilt are similar for the same current densities as the two previous samples except for the extreme angle which is smaller and it saturates around 110°. For the SAF, we observe also this saturation at 110° but before all the angles are much smaller, for instance at J = 1.3×10^{11}, the angle of DWs in the SAF is slightly above the initial state, at 93° when the other samples have already reached 110°. At J = 1.5×10^{11}, the SAF tilt is only of 103° when it is 20° more in the samples which do not saturate. The reason is likely the Zeeman interaction between the Oersted field and the net moment of each sample. The

SAF with almost zero net moment is therefore less sensitive to the field compared to the single layers or the opposite synthetic ferrimagnet where M_S is maximum which explains that the angle culminates at $\alpha = 135°$.

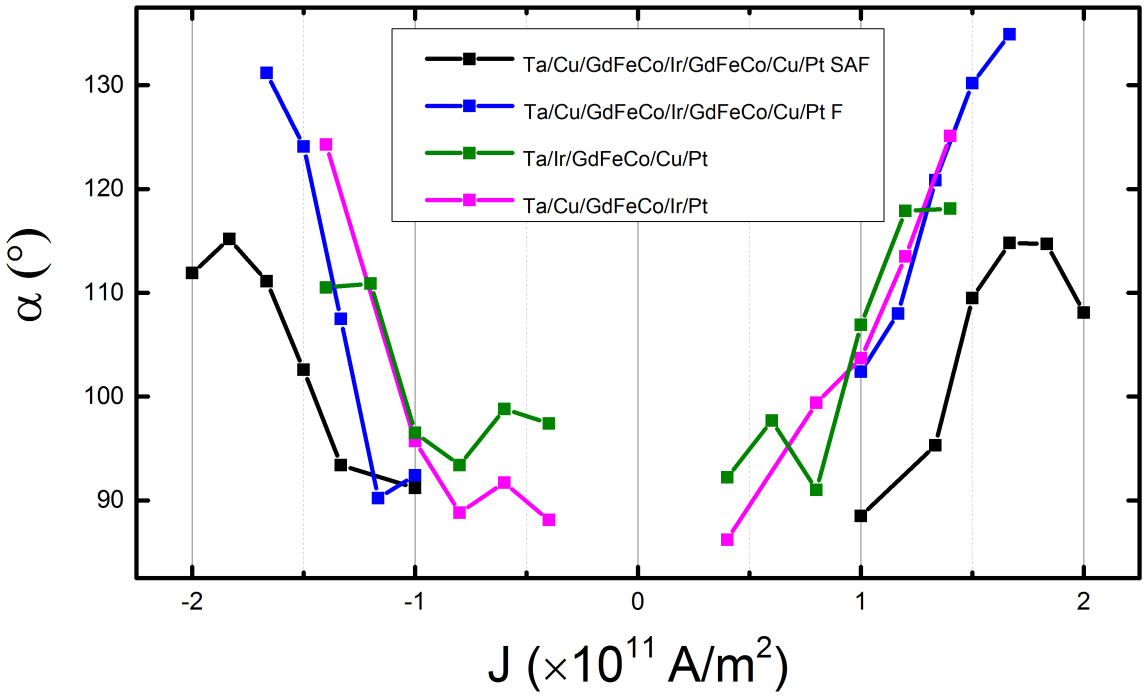

Figure 5.11: Angle of the DW formed with the current direction as a function of the current density for different stacks

5.3.2 Second harmonic measurements

In order to understand the absence of motion when the coupling is ferromagnetic in the bilayer, we have performed second harmonic measurement of the SAF and this sample to make the comparison. The second harmonic measurement[106] consists in estimating the magnitude of SOT using Hall measurements to probe current-induced effective fields. The geometry of the measurement is the same as for the AHE, the only difference resides in the fact that we use AC current instead of DC and the second harmonic transverse voltage is measured. To obtain the damping-like effective field ΔH_x an external magnetic field is applied along the current direction (x axis), while to have the field-like effective field ΔH_y the external field is applied perpendicularly to the current (y axis). The measure of ΔH_y also includes the Oersted field ΔH_{Oe}. The effective fields are defined as:

$$\Delta H_{x,y} = -2\frac{\partial V_{2\omega}}{\partial H_{x,y}} \Big/ \frac{\partial^2 V_{\omega}}{\partial H_{x,y}^2} \tag{5.2}$$

In figure 5.12 is shown the results of the second harmonic measurements for Ta/Cu/GdFeCo/Ir(x)/GdFeCo/Cu/Pt with x = 0.6 nm for a antiferromagnetic coupling (fig.5.12(a)(c) and 0.4 nm for ferromagnetic coupling (fig.5.12(b)(d)). We show that regardless of the coupling, the values of the damping-like and field-like effective fields are indeed the same for both samples and a difference of applied torques is not the reason of the absence of motion for the ferromagnetic bilayer.

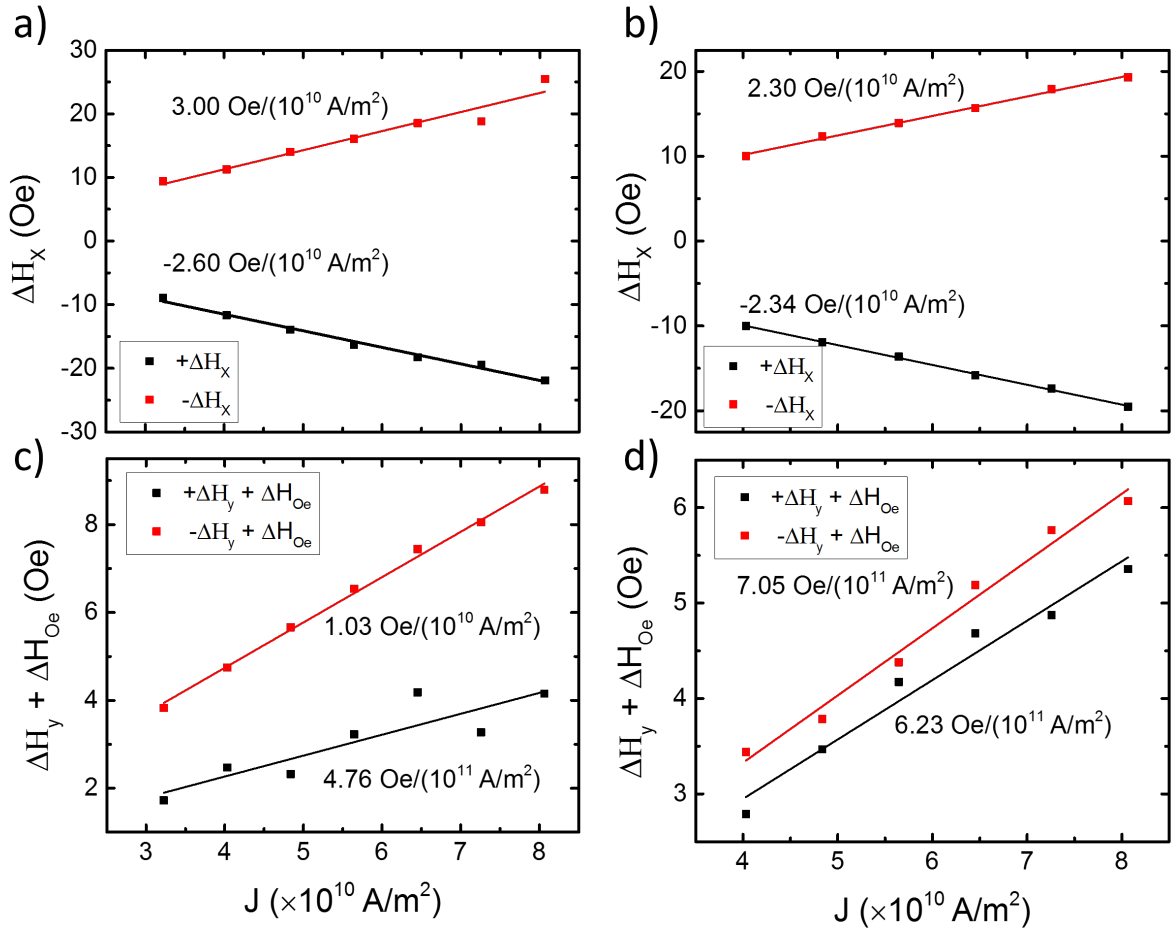

Figure 5.12: Field-like (ΔH_y) effective field + Oersted field (ΔH_{Oe}) and damping-like (ΔH_x) effective field as a function of current density and linear fitting for +M magnetization (black) and -M magnetization (red)

5.4 Conclusion

We have observed DWs propagation in our samples that is dominated by SOT. However it is impossible to reach the required current density in order to achieve high velocity displacement. Indeed, the Oersted field generated is sufficient to affect the magnetization of the domains even if it is not the driving mechanism. When motion can still be observed, the DWs are first tilted by an angle proportional to the current intensity. The deformation is symmetric for both walls of a domain leading to a trapezoid form. Finally, the Oersted field cuts in half the domain in the wire. Surprisingly, in the literature, even when a similar effect is reported, the value of the estimated Oersted field by empirical formula is almost two order of magnitude lower of what we have simulated or observed regarding the coercive field of our samples[103,104]. In GdFeCo, the effect of the Oersted field has not been reported despite the fact that much higher current density is applied. The structure of our stack might be involved since our magnetic material is surrounded by highly conductive metallic layers that can contribute to a high Oersted field generation. Moreover, in spite of the instantaneous effect of this field that is in the range of our coercive field, it is observed for microsecond pulses and heating cannot be neglected. It probably accentuates the consequence of the current-induced field.

Chapter 6

General conclusion

In the thesis, we focused on the effects of current-induced phenomena on the magnetization of GdFeCo ferrimagnet alloy and we grew coupled layers to investigate the benefits of such structures especially for domain-wall propagation.

Our first thin films depositions made us understand that at our considered thickness of 5 nm that the PMA is not always guaranteed and due to the unique magnetization governed by sub-lattices moment orientation, we have noticed major changes as a function of the adjacent layers. Indeed, if the dependence of the total moment of GdFeCo on the temperature and the composition was already known, we investigated the systematic variations as a function of the interfaces. We grew series of samples and we have shown that the composition of magnetic compensation depends both on the seed layer and the capping layer. The observed shifts were coherent with a polarization of the adjacent layers. If the increase of total magnetization leads to a higher demagnetizing field and thus favorizes an in-plane magnetization, this alone cannot explain the samples that exhibit PMA for a very small range of composition. Further investigations, such as TEM imaging, did not reveal observable changes in the amorphous bulk of the GdFeCo. With the knowledge of this study on the interfaces, we chose a structure for the SAF that contains layer with large SHA such as Pt or Ta for spin currents generation as well as Cu layers in order to maintain PMA. We have shown that is possible to obtain strongly RKKY coupled GdFeCo layers which offers many possibilities to tune the properties of the SAF.

The next part of this project focused on the current-induced switching of, first, the layers of the SAF individually and second, the SAF itself. Conventional SOT switching has been observed while an external magnetic field is applied. Surprisingly, we kept observing switching even in the absence of field. Kerr microscopy and

comparison of the amplitude allowed us to understand that it was actually partial switching induced by Oersted field. Already observed in the literature, we have shown here that the nucleation of a longitudinal domain parallel to the current direction in a Hall cross geometry has square AHE hysteresis cycles similar to SOT ones. Especially in small devices such as 2 μm-wide Hall crosses, the tiny difference of amplitude between full and partial reversal of the magnetization can lead to confusion between the two mechanisms. We have observed larger Oersted field values and consequences of what can be reported or estimated in the literature in which current-induced fields are very often neglected. From our work, we would recommend to complete switching measurements, especially in the case of partial switching, with Kerr microscopy.

The understanding of the magnetic behavior of our sample could be interesting to manipulate the magnetization by combining SOT and Oersted field effects on the magnetization. Adding an external field or not can permit to access more than two magnetic states (fig.6.1 (left)) with a good control. Moreover, with a small field, a longitudinal domain can be expanded in the entire Hall cross allowing to access to the two saturated states (fig.6.1 (right)) and not only switch between one intermediate state and a full one.

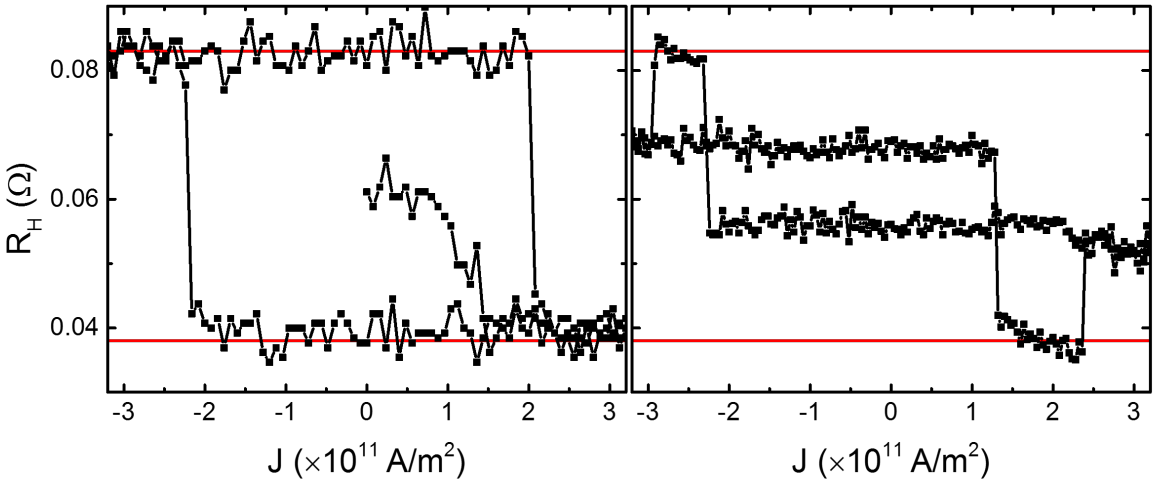

Figure 6.1: (Left) SOT switching of Ta/Ir/GdFeCo/Cu with an external applied field after the Oersted field nucleation of a domain without any external field. (Right) Oersted field induced switching with $H_X = 16$ *Oe*. Red horizontal lines are the resistances of saturated magnetic states

We have shown that the SOT switching in SAF is not as efficient as in single layers and also requires an in-plane magnetic field. AHE measurements is not convenient due to the compensation of the signal coming from each layer of the SAF. Without field, we observed longitudinal domains nucleation as well. Our SAF structure do not exhibit any advantages regarding the SOT switching at room temperature.

Finally, we focused on the domain wall propagation either in single GdFeCo layers or in SAF samples. We

have been able to confirm that the SOT is indeed the implied mechanism for the DW motion in our samples. Unfortunately, even if we could have expected high DW velocities given the propagation in the full films the effect of the Oersted field is dramatic whether on the velocity or the integrity of the DW. As we increase the current intensity, the tilt of the DW induced by the Oersted field increases too. Eventually, the domain is split in half and no more displacement can be observe. We have shown that the increase of the angle follows the same evolution for the different samples but the value of the angle saturates for the SAF which imply a dependence with the total moment. For high velocities over 100 m/s, we should inject much higher current densities and we have not been able to pursue the investigations.

Perspectives

Our preliminary study on the magnetism of GdFeCo shows a "set of rules" to grow more advanced structures and to tune the properties of the stack as needed. These results already allowed us to deposit enhanced stacks for some other projects in our team. However, after our measurements, the effect of the interfaces on the anisotropy is not clear and its origin is still uncertain. One could first consider to measure the saturation field in series of samples. Due to the complexity of SQUID measurements and the possible artifacts arising from the substrates, we could imagine AHE measurements of series of full films with direct wire-bonds on square-shaped pieces. Also, to go further into the origins of the anisotropy of the GdFeCo, EXAFS measurements in a synchrotron could help to investigate the atomic-scale structural anisotropy.

Since if it was not the objective of our project, we have not pursued the measurements of all-optical switching on our samples but it would be very interesting to observe the switching in coupled GdFeCo layers. Especially, we could try a SAF in which one layer is switchable by AOS and the other layer is not by changing its composition in order to see if the AOS of one layer can result in the switching of the other. By tuning whether the coupling or the composition, we could study the effects on the threshold fluence or the timescale of the switching.

To solve the problems caused by the Oersted field, we have started to look at the impact of reducing the thickness of the Cu layers. With the right composition, near to the compensation, and by removing gold pads (to avoid the heat stress of the lithography), we have been able to remove the Cu layers. Nevertheless, magnetic domains kept nucleating by Oersted field in our device. At our considered compositions and stack orders, the Oersted field may be inherent but we could consider depositing our ferrimagnet directly on the substrate and having only a Pt capping layer. An other stack could include an insulator as capping layer and only one layer to provided the spin current such as Pt/GdFeCo/SiN. If the Oersted field problem can be overcome, the

velocity measurements as a function of the temperature could turn out to be very interesting combining total net moment compensation, layer magnetic compensation and angular momentum compensation. Even if they are less interesting from an application point of view, field-driven DW propagation could give us information in the first place, especially the maximum reachable velocity or the temperatures of compensation. We could also confirm that we are actually able to reduce the effect of the Walker breakdown as in function of the total magnetic moment in the SAF.

Bibliography

[1] Baibich, M. N., Broto, J. M., Fert, A., Van Dau, F. N., Petroff, F., Etienne, P., Creuzet, G., Friederich, A., and Chazelas, J. "Giant Magnetoresistance of (001)Fe/(001)Cr Magnetic Superlattices". *Physical Review Letters*. **61**, 21 (1988), pp. 2472–2475.

[2] Parkin, S. "Magnetotransport in transition metal multilayered structures". *Matematisk Fysiske Meddelelser-Kongelige Danske Videnskabernes Selskab*. **45**, (1997), pp. 113–132.

[3] Slonczewski, J. "Current-driven excitation of magnetic multilayers". *Journal of Magnetism and Magnetic Materials*. **159**, 1 (1996), pp. L1–L7.

[4] Berger, L. "Exchange interaction between ferromagnetic domain wall and electric current in very thin metallic films". *Journal of Applied Physics*. **55**, 6 (1984), pp. 1954–1956.

[5] Berger, L. "Emission of spin waves by a magnetic multilayer traversed by a current". *Physical Review B*. **54**, 13 (1996), p. 9353.

[6] Marrows, C. "Spin-polarised currents and magnetic domain walls". *Advances in Physics*. **54**, 8 (2005), pp. 585–713.

[7] Fert, A. and Campbell, I. A. "Two-Current Conduction in Nickel". *Physical Review Letters*. **21**, 16 (1968), pp. 1190–1192.

[8] Cohen-Tannoudji, C., Diu, B., and Laloë, F. *Quantum mechanics*. Wiley, 1977.

[9] Nagaosa, N., Sinova, J., Onoda, S., MacDonald, A. H., and Ong, N. P. "Anomalous Hall effect". *Reviews of Modern Physics*. **82**, 2 (2010), pp. 1539–1592.

[10] Sinova, J., Valenzuela, S. O., Wunderlich, J., Back, C. H., and Jungwirth, T. "Spin Hall effects". *Reviews of Modern Physics*. **87**, 4 (2015), pp. 1213–1260.

[11] Kimura, T., Otani, Y., Sato, T., Takahashi, S., and Maekawa, S. "Room-Temperature Reversible Spin Hall Effect". *Physical Review Letters*. **98**, 15 (2007), p. 156601.

[12] Ganichev, S., Ivchenko, E., Bel'Kov, V., Tarasenko, S., Sollinger, M., Weiss, D., Wegscheider, W., and Prettl, W. "Spin-galvanic effect". *Nature*. **417**, 6885 (2002), pp. 153–156.

[13] Ando, K., Takahashi, S., Harii, K., Sasage, K., Ieda, J., Maekawa, S., and Saitoh, E. "Electric Manipulation of Spin Relaxation Using the Spin Hall Effect". *Physical Review Letters*. **101**, 3 (2008), p. 036601.

[14] Miron, I. M., Garello, K., Gaudin, G., Zermatten, P.-J., Costache, M. V., Auffret, S., Bandiera, S., Rodmacq, B., Schuhl, A., and Gambardella, P. "Perpendicular switching of a single ferromagnetic layer induced by in-plane current injection". *Nature*. **476**, 7359 (2011), pp. 189–193.

[15] Prenat, G., Jabeur, K., Vanhauwaert, P., Di Pendina, G., Oboril, F., Bishnoi, R., Ebrahimi, M., Lamard, N., Boulle, O., Garello, K., et al. "Ultra- and high-reliability SOT-MRAM: From cache replacement to normally-off computing". *IEEE Transactions on Multi-Scale Computing Systems*. **2**, 1 (2015), pp. 49–60.

[16] Kurenkov, A., Zhang, C., DuttaGupta, S., Fukami, S., and Ohno, H. "Device-size dependence of field-free spin-orbit torque induced magnetization switching in antiferromagnet/ferromagnet structures". *Applied Physics Letters*. **110**, 9 (2017), p. 092410.

[17] Oh, Y.-W., Baek, S.-H. C., Kim, Y., Lee, H. Y., Lee, K.-D., Yang, C.-G., Park, E.-S., Lee, K.-S., Kim, K.-W., Go, G., et al. "Field-free switching of perpendicular magnetization through spin–orbit torque in antiferromagnet/ferromagnet/oxide structures". *Nature nanotechnology*. **11**, 10 (2016), pp. 878–884.

[18] Kong, W., Ji, Y., Zhang, X., Wu, H., Zhang, Q., Yuan, Z., Wan, C., Han, X., Yu, T., Fukuda, K., et al. "Field-free spin Hall effect driven magnetization switching in Pd/Co/IrMn exchange coupling system". *Applied Physics Letters*. **109**, 13 (2016), p. 132402.

[19] Lau, Y.-C., Betto, D., Rode, K., Coey, J., and Stamenov, P. "Spin–orbit torque switching without an external field using interlayer exchange coupling". *Nature nanotechnology*. **11**, 9 (2016), pp. 758–762.

[20] Seung-heon, C. B., Amin, V. P., Oh, Y.-W., Go, G., Lee, S.-J., Lee, G.-H., Kim, K.-J., Stiles, M. D., Park, B.-G., and Lee, K.-J. "Spin currents and spin–orbit torques in ferromagnetic trilayers". *Nature materials*. **17**, 6 (2018), pp. 509–513.

[21] Wang, M., Cai, W., Zhu, D., Wang, Z., Kan, J., Zhao, Z., Cao, K., Wang, Z., Zhang, Y., Zhang, T., et al. "Field-free switching of a perpendicular magnetic tunnel junction through the interplay of spin–orbit and spin-transfer torques". *Nature electronics*. **1**, 11 (2018), pp. 582–588.

[22] Chen, J.-Y., Dc, M., Zhang, D., Zhao, Z., Li, M., and Wang, J.-P. "Field-free spin-orbit torque switching of composite perpendicular CoFeB/Gd/CoFeB layers utilized for three-terminal magnetic tunnel junctions". *Applied Physics Letters*. **111**, 1 (2017), p. 012402.

[23] Yu, G., Upadhyaya, P., Fan, Y., Alzate, J. G., Jiang, W., Wong, K. L., Takei, S., Bender, S. A., Chang, L.-T., Jiang, Y., et al. "Switching of perpendicular magnetization by spin–orbit torques in the absence of external magnetic fields". *Nature nanotechnology*. **9**, 7 (2014), pp. 548–554.

[24] Wu, H., Nance, J., Razavi, S. A., Lujan, D., Dai, B., Liu, Y., He, H., Cui, B., Wu, D., Wong, K., et al. "Chiral Symmetry Breaking for Deterministic Switching of Perpendicular Magnetization by Spin–Orbit Torque". *Nano letters*. **21**, 1 (2020), pp. 515–521.

[25] Brooks, M., Nordstrom, L., and Johansson, B. "3d-5d band magnetism in rare earth-transition metal intermetallics: total and partial magnetic moments of the RFe2 (R= Gd-Yb) Laves phase compounds". *Journal of Physics: Condensed Matter*. **3**, 14 (1991), p. 2357.

[26] Pogorily, A., Shypil, E., and Alexander, C. "A study of magnetization in exchange-coupled FM/Gd bilayers". *Journal of magnetism and magnetic materials*. **286**, (2005), pp. 493–496.

[27] Jensen, J. and Mackintosh, A. R. *Rare earth magnetism*. Clarendon Press Oxford, 1991.

[28] Graves, C., Reid, A., Wang, T., Wu, B., De Jong, S., Vahaplar, K., Radu, I., Bernstein, D., Messerschmidt, M., Müller, L., et al. "Nanoscale spin reversal by non-local angular momentum transfer following ultrafast laser excitation in ferrimagnetic GdFeCo". *Nature materials*. **12**, 4 (2013), pp. 293–298.

[29] Beaurepaire, E., Merle, J.-C., Daunois, A., and Bigot, J.-Y. "Ultrafast spin dynamics in ferromagnetic nickel". *Physical review letters*. **76**, 22 (1996), p. 4250.

[30] Stanciu, C. D., Hansteen, F., Kimel, A. V., Kirilyuk, A., Tsukamoto, A., Itoh, A., and Rasing, T. "All-optical magnetic recording with circularly polarized light". *Physical review letters*. **99**, 4 (2007), p. 047601.

[31] Lambert, C.-H., Mangin, S., Varaprasad, B. C. S., Takahashi, Y., Hehn, M., Cinchetti, M., Malinowski, G., Hono, K., Fainman, Y., Aeschlimann, M., et al. "All-optical control of ferromagnetic thin films and nanostructures". *Science*. **345**, 6202 (2014), pp. 1337–1340.

[32] Mangin, S., Gottwald, M., Lambert, C., Steil, D., Uhlíř, V., Pang, L., Hehn, M., Alebrand, S., Cinchetti, M., Malinowski, G., et al. "Engineered materials for all-optical helicity-dependent magnetic switching". *Nature materials*. **13**, 3 (2014), pp. 286–292.

[33] Awano, H., Ohnuki, S., Shirai, H., Ohta, N., Yamaguchi, A., Sumi, S., and Torazawa, K. "Magnetic domain expansion readout for amplification of an ultra high density magneto-optical recording signal". *Applied physics letters*. **69**, 27 (1996), pp. 4257–4259.

[34] Hansen, P., Clausen, C., Much, G., Rosenkranz, M., and Witter, K. "Magnetic and magneto-optical properties of rare-earth transition-metal alloys containing Gd, Tb, Fe, Co". *Journal of applied physics*. **66**, 2 (1989), pp. 756–767.

[35] Kimel, A., Kirilyuk, A., Usachev, P., Pisarev, R., Balbashov, A., and Rasing, T. "Ultrafast non-thermal control of magnetization by instantaneous photomagnetic pulses". *Nature*. **435**, 7042 (2005), pp. 655–657.

[36] Roschewsky, N., Matsumura, T., Cheema, S., Hellman, F., Kato, T., Iwata, S., and Salahuddin, S. "Spin-orbit torques in ferrimagnetic GdFeCo alloys". *Applied Physics Letters*. **109**, 11 (2016), p. 112403.

[37] Parkin, S. S. *Shiftable magnetic shift register and method of using the same*. US Patent 6,834,005. 2004.

[38] Parkin, S. S., Hayashi, M., and Thomas, L. "Magnetic domain-wall racetrack memory". *Science*. **320**, 5873 (2008), pp. 190–194.

[39] Shen, M., Zhang, Y., You, L., and Yang, X. "Readable racetrack memory via ferromagnetically coupled chiral domain walls". *Applied Physics Letters*. **113**, 15 (2018), p. 152401.

[40] Tono, T., Taniguchi, T., Kim, K.-J., Moriyama, T., Tsukamoto, A., and Ono, T. "Chiral magnetic domain wall in ferrimagnetic GdFeCo wires". *Applied Physics Express*. **8**, 7 (2015), p. 073001.

[41] Lalieu, M. L., Lavrijsen, R., and Koopmans, B. "Integrating all-optical switching with spintronics". *Nature communications*. **10**, 1 (2019), pp. 1–6.

[42] Ebert, H. "Magneto-optical effects in transition metal systems". *Reports on Progress in Physics*. **59**, 12 (1996), p. 1665.

[43] Landau, L. D., Bell, J., Kearsley, M., Pitaevskii, L., Lifshitz, E., and Sykes, J. *Electrodynamics of continuous media*. elsevier.

[44] Sato, K. and Togami, Y. "Magneto-optical spectra of RF-sputtered amorphous Gd-Co and Gd-Fe films". *Journal of magnetism and magnetic materials*. **35**, 1-3 (1983), pp. 181–182.

[45] Larkin, A. and Melnikov, V. "Magnetic impurities in an almost magnetic metal". *SOV PHYS JETP*. **34**, 3 (1972), pp. 656–661.

[46] Parkin, S. S. "Systematic variation of the strength and oscillation period of indirect magnetic exchange coupling through the 3d, 4d, and 5d transition metals". *Physical Review Letters*. **67**, 25 (1991), p. 3598.

[47] Le Dang, K., Veillet, P., Chappert, C., Farrow, R., Marks, R., Weller, D., and Cebollada, A. "Antiferromagnetic coupling in (111)-oriented Co/Pt superlattices". *Physical Review B*. **50**, 1 (1994), p. 200.

[48] Simopoulos, A., Devlin, E., Kostikas, A., Jankowski, A., Croft, M., and Tsakalakos, T. "Structure and enhanced magnetization in Fe/Pt multilayers". *Physical Review B*. **54**, 14 (1996), p. 9931.

[49] Knepper, J. and Yang, F. "Oscillatory interlayer coupling in Co/ Pt multilayers with perpendicular anisotropy". *Physical review B*. **71**, 22 (2005), p. 224403.

[50] Meier, F., Lounis, S., Wiebe, J., Zhou, L., Heers, S., Mavropoulos, P., Dederichs, P. H., Blügel, S., and Wiesendanger, R. "Spin polarization of platinum (111) induced by the proximity to cobalt nanostripes". *Physical Review B*. **83**, 7 (2011), p. 075407.

[51] Wu, R., Chen, L., and Kioussis, N. "Structural and magnetic properties of fcc Pt/Fe (111) multilayers". *Journal of applied physics*. **79**, 8 (1996), pp. 4783–4785.

[52] McGuire, T., Aboaf, J., and Klokholm, E. "Magnetic and transport properties of Co-Pt thin films". *Journal of applied physics*. **55**, 6 (1984), pp. 1951–1953.

[53] Mukhopadhyay, A., Vayalil, S. K., Graulich, D., Ahamed, I., Francoual, S., Kashyap, A., Kuschel, T., and Kumar, P. A. "Asymmetric modification of the magnetic proximity effect in Pt/Co/Pt trilayers by the insertion of a Ta buffer layer". *Physical Review B*. **102**, 14 (2020), p. 144435.

[54] Perini, M., Meyer, S., Dupé, B., Von Malottki, S., Kubetzka, A., Von Bergmann, K., Wiesendanger, R., and Heinze, S. "Domain walls and dzyaloshinskii-moriya interaction in epitaxial co/ir (111) and pt/co/ir (111)". *Physical Review B*. **97**, 18 (2018), p. 184425.

[55] Wilhelm, F., Poulopoulos, P., Wende, H., Scherz, A., Baberschke, K., Angelakeris, M., Flevaris, N., and Rogalev, A. "Systematics of the Induced Magnetic Moments in 5 d Layers and the Violation of the Third Hund's Rule". *Physical review letters*. **87**, 20 (2001), p. 207202.

[56] Samant, M., Stöhr, J., Parkin, S., Held, G., Hermsmeier, B., Herman, F., Van Schilfgaarde, M., Duda, L.-C., Mancini, D., Wassdahl, N., et al. "Induced spin polarization in Cu spacer layers in Co/Cu multilayers". *Physical review letters*. **72**, 7 (1994), p. 1112.

[57] Held, G., Samant, M., Stöhr, J., Hermsmeier, B., Schilfgaarde, M. van, and Nakajimas, R. "X-ray magnetic circular dichroism study of the induced spin polarization of Cu in Co/Cu and Fe/Cu multilayers". *Zeitschrift für Physik B Condensed Matter*. **100**, 3 (1997), pp. 335–341.

[58] Kuch, W., Salvietti, M., Gao, X., Klaua, M., Barthel, J., Mohan, C. V., and Kirschner, J. "Artificial FeCu (100) epitaxial ordered alloy films: Element-selective magnetic properties". *Journal of applied physics*. **83**, 11 (1998), pp. 7019–7021.

[59] Leamy, H. and Dirks, A. "Microstructure and magnetism in amorphous rare-earth–transition-metal thin films. II. Magnetic anisotropy". *Journal of Applied Physics*. **50**, 4 (1979), pp. 2871–2882.

[60] Takeno, Y., Kaneko, K., and Goto, K. "Magnetic properties of amorphous (Tb1-xGdx) 30Fe70 thin films". *Japanese journal of applied physics*. **30**, 8R (1991), p. 1701.

[61] Coey, J. M. D., Chappert, J., Rebouillat, J., and Wang, T. "Magnetic structure of an amorphous rare-earth transition-metal alloy". *Physical Review Letters*. **36**, 17 (1976), p. 1061.

[62] Harris, V., Aylesworth, K., Das, B., Elam, W., and Koon, N. "Structural origins of magnetic anisotropy in sputtered amorphous Tb-Fe films". *Physical review letters*. **69**, 13 (1992), p. 1939.

[63] Harris, V. G. and Pokhil, T. "Selective-resputtering-induced perpendicular magnetic anisotropy in amorphous TbFe films". *Physical review letters*. **87**, 6 (2001), p. 067207.

[64] Ding, M. and Poon, S. J. "Tunable perpendicular magnetic anisotropy in GdFeCo amorphous films". *Journal of Magnetism and Magnetic Materials*. **339**, (2013), pp. 51–55.

[65] Yang, S.-H., Ryu, K.-S., and Parkin, S. "Domain-wall velocities of up to 750 m s- 1 driven by exchange-coupling torque in synthetic antiferromagnets". *Nature nanotechnology*. **10**, 3 (2015), pp. 221–226.

[66] Ruderman, M. A. and Kittel, C. "Indirect exchange coupling of nuclear magnetic moments by conduction electrons". *Physical Review*. **96**, 1 (1954), p. 99.

[67] Kasuya, T. "A theory of metallic ferro-and antiferromagnetism on Zener's model". *Progress of theoretical physics*. **16**, 1 (1956), pp. 45–57.

[68] Yosida, K. "Magnetic properties of Cu-Mn alloys". *Physical Review*. **106**, 5 (1957), p. 893.

[69] Bruno, P. "Theory of interlayer magnetic coupling". *Physical Review B*. **52**, 1 (1995), p. 411.

[70] Parkin, S. and Mauri, D. "Spin engineering: Direct determination of the Ruderman-Kittel-Kasuya-Yosida far-field range function in ruthenium". *Physical Review B*. **44**, 13 (1991), p. 7131.

[71] Stoner, E. C. and Wohlfarth, E. "A mechanism of magnetic hysteresis in heterogeneous alloys". *Philosophical Transactions of the Royal Society of London. Series A, Mathematical and Physical Sciences*. **240**, 826 (1948), pp. 599–642.

[72] Koplak, O., Talantsev, A., Lu, Y., Hamadeh, A., Pirro, P., Hauet, T., Morgunov, R., and Mangin, S. "Magnetization switching diagram of a perpendicular synthetic ferrimagnet CoFeB/Ta/CoFeB bilayer". *Journal of Magnetism and Magnetic Materials*. **433**, (2017), pp. 91–97.

[73] Emori, S., Bauer, U., Ahn, S.-M., Martinez, E., and Beach, G. S. "Current-driven dynamics of chiral ferromagnetic domain walls". *Nature materials*. **12**, 7 (2013), pp. 611–616.

[74] Fache, T., Rojas-Sanchez, J., Badie, L., Mangin, S., and Petit-Watelot, S. "Determination of spin Hall angle, spin mixing conductance, and spin diffusion length in CoFeB/Ir for spin-orbitronic devices". *Physical Review B*. **102**, 6 (2020), p. 064425.

[75] Yakata, S., Ando, Y., Miyazaki, T., and Mizukami, S. "Temperature dependences of spin-diffusion lengths of Cu and Ru layers". *Japanese journal of applied physics*. **45**, 5R (2006), p. 3892.

[76] Boulle, O., Heyne, L., Rhensius, J., Kläui, M., Rüdiger, U., Joly, L., Le Guyader, L., Nolting, F., Heyderman, L. J., Malinowski, G., et al. "Reversible switching between bidomain states by injection of current pulses in a magnetic wire with out-of-plane magnetization". *Journal of Applied Physics*. **105**, 7 (2009), p. 07C106.

[77] Bhowmik, D., Nowakowski, M. E., You, L., Lee, O., Keating, D., Wong, M., Bokor, J., and Salahuddin, S. "Deterministic domain wall motion orthogonal to current flow due to spin orbit torque". *Scientific reports*. **5**, 1 (2015), pp. 1–10.

[78] Gale, W. F. and Totemeier, T. C. *Smithells metals reference book*. Elsevier, 2003.

[79] Malozemoff, A. and Slonczewski, J. C. *Magnetic domain walls in bubble materials: advances in materials and device research*. Vol. 1. Academic press, 2016.

[80] Thiaville, A., Nakatani, Y., Miltat, J., and Suzuki, Y. "Micromagnetic understanding of current-driven domain wall motion in patterned nanowires". *EPL (Europhysics Letters)*. **69**, 6 (2005), p. 990.

[81] Labrune, M., Andrieu, S., Rio, F., and Bernstein, P. "Time dependence of the magnetization process of RE-TM alloys". *Journal of magnetism and magnetic materials*. **80**, 2-3 (1989), pp. 211–218.

[82] Metaxas, P., Jamet, J., Mougin, A., Cormier, M., Ferré, J., Baltz, V., Rodmacq, B., Dieny, B., and Stamps, R. "Creep and flow regimes of magnetic domain-wall motion in ultrathin Pt/Co/Pt films with perpendicular anisotropy". *Physical review letters*. **99**, 21 (2007), p. 217208.

[83] Brataas, A. and Hals, K. M. "Spin–orbit torques in action". *Nature nanotechnology*. **9**, 2 (2014), pp. 86–88.

[84] Dzyaloshinsky, I. "A thermodynamic theory of "weak" ferromagnetism of antiferromagnetics". *Journal of physics and chemistry of solids*. **4**, 4 (1958), pp. 241–255.

[85] Moriya, T. "Anisotropic superexchange interaction and weak ferromagnetism". *Physical review*. **120**, 1 (1960), p. 91.

[86] Thiaville, A., Rohart, S., Jué, É., Cros, V., and Fert, A. "Dynamics of Dzyaloshinskii domain walls in ultrathin magnetic films". *EPL (Europhysics Letters)*. **100**, 5 (2012), p. 57002.

[87] Liu, L., Lee, O., Gudmundsen, T., Ralph, D., and Buhrman, R. "Current-induced switching of perpendicularly magnetized magnetic layers using spin torque from the spin Hall effect". *Physical review letters*. **109**, 9 (2012), p. 096602.

[88] Liu, L., Pai, C.-F., Li, Y., Tseng, H., Ralph, D., and Buhrman, R. "Spin-torque switching with the giant spin Hall effect of tantalum". *Science*. **336**, 6081 (2012), pp. 555–558.

[89] Pai, C.-F., Liu, L., Li, Y., Tseng, H., Ralph, D., and Buhrman, R. "Spin transfer torque devices utilizing the giant spin Hall effect of tungsten". *Applied Physics Letters*. **101**, 12 (2012), p. 122404.

[90] Haazen, P., Murè, E., Franken, J., Lavrijsen, R., Swagten, H., and Koopmans, B. "Domain wall depinning governed by the spin Hall effect". *Nature materials*. **12**, 4 (2013), pp. 299–303.

[91] Khvalkovskiy, A., Cros, V., Apalkov, D., Nikitin, V., Krounbi, M., Zvezdin, K., Anane, A., Grollier, J., and Fert, A. "Matching domain-wall configuration and spin-orbit torques for efficient domain-wall motion". *Physical Review B*. **87**, 2 (2013), p. 020402.

[92] Kim, K.-W., Seo, S.-M., Ryu, J., Lee, K.-J., and Lee, H.-W. "Magnetization dynamics induced by in-plane currents in ultrathin magnetic nanostructures with Rashba spin-orbit coupling". *Physical Review B*. **85**, 18 (2012), p. 180404.

[93] Kuteifan, M., Lubarda, M., Fu, S., Chang, R., Escobar, M., Mangin, S., Fullerton, E., and Lomakin, V. "Large exchange-dominated domain wall velocities in antiferromagnetically coupled nanowires". *AIP Advances*. **6**, 4 (2016), p. 045103.

[94] Parkin, S. *Shiftable magnetic shift register and method of using the same*. US Patent n6,834,005. 2003.

[95] Parkin, S. and Yang, S.-H. "Memory on the racetrack". *Nature nanotechnology*. **10**, 3 (2015), pp. 195–198.

[96] Kim, D.-H., Okuno, T., Kim, S. K., Oh, S.-H., Nishimura, T., Hirata, Y., Futakawa, Y., Yoshikawa, H., Tsukamoto, A., Tserkovnyak, Y., et al. "Low magnetic damping of ferrimagnetic GdFeCo alloys". *Physical review letters*. **122**, 12 (2019), p. 127203.

[97] Kim, K.-J., Kim, S. K., Hirata, Y., Oh, S.-H., Tono, T., Kim, D.-H., Okuno, T., Ham, W. S., Kim, S., Go, G., et al. "Fast domain wall motion in the vicinity of the angular momentum compensation temperature of ferrimagnets". *Nature materials*. **16**, 12 (2017), pp. 1187–1192.

[98] Okuno, T., Kim, D.-H., Oh, S.-H., Kim, S. K., Hirata, Y., Nishimura, T., Ham, W. S., Futakawa, Y., Yoshikawa, H., Tsukamoto, A., et al. "Spin-transfer torques for domain wall motion in antiferromagnetically coupled ferrimagnets". *Nature Electronics*. **2**, 9 (2019), pp. 389–393.

[99] Haltz, E., Sampaio, J., Krishnia, S., Berges, L., Weil, R., and Mougin, A. "Measurement of the tilt of a moving domain wall shows precession-free dynamics in compensated ferrimagnets". *Scientific reports*. **10**, 1 (2020), pp. 1–7.

[100] Belabbes, A., Bihlmayer, G., Bechstedt, F., Blügel, S., and Manchon, A. "Hund's rule-driven dzyaloshinskii-moriya interaction at 3 d- 5 d interfaces". *Physical review letters*. **117**, 24 (2016), p. 247202.

[101] Heinze, S., Von Bergmann, K., Menzel, M., Brede, J., Kubetzka, A., Wiesendanger, R., Bihlmayer, G., and Blügel, S. "Spontaneous atomic-scale magnetic skyrmion lattice in two dimensions". *nature physics*. **7**, 9 (2011), pp. 713–718.

[102] Yang, H., Hu, S., Tang, M., Chen, S., Chen, H., Wu, D., and Qiu, X. "Spin-orbit torque and Dzyaloshinskii-Moriya interaction in perpendicularly magnetized heterostructures with iridium". *Applied Physics Letters*. **118**, 6 (2021), p. 062409.

[103] Yamanouchi, M., Chiba, D., Matsukura, F., Dietl, T., and Ohno, H. "Velocity of domain-wall motion induced by electrical current in the ferromagnetic semiconductor (Ga, Mn) As". *Physical review letters*. **96**, 9 (2006), p. 096601.

[104] Adam, J.-P., Vernier, N., Ferré, J., Thiaville, A., Jeudy, V., Lemaître, A., Thevenard, L., and Faini, G. "Nonadiabatic spin-transfer torque in (Ga, Mn) As with perpendicular anisotropy". *Physical Review B*. **80**, 19 (2009), p. 193204.

[105] Caretta, L., Mann, M., Büttner, F., Ueda, K., Pfau, B., Günther, C. M., Hessing, P., Churikova, A., Klose, C., Schneider, M., et al. "Fast current-driven domain walls and small skyrmions in a compensated ferrimagnet". *Nature nanotechnology*. **13**, 12 (2018), pp. 1154–1160.

[106] Kim, J., Sinha, J., Hayashi, M., Yamanouchi, M., Fukami, S., Suzuki, T., Mitani, S., and Ohno, H. "Layer thickness dependence of the current-induced effective field vector in Ta| CoFeB| MgO". *Nature materials*. **12**, 3 (2013), pp. 240–245.

[107] Yang, H., Hu, S., Tang, M., Chen, S., Chen, H., Wu, D., and Qiu, X. "Spin–orbit torque and Dzyaloshinskii–Moriya interaction in perpendicularly magnetized heterostructures with iridium". *Applied Physics Letters*. **118**, 6 (2021), p. 062409.

Résumé

L'amélioration des techniques de croissance a permis d'observer pour la première fois en 1988 l'effet de magnétorésistance géante (GMR) dans les vannes de spin (pour cette découverte, le prix Nobel a été décerné à Albert Fert et Peter Grünberg en 2007). Une vanne de spin est un système qui consiste à superposer deux couches magnétiques séparées par un mince séparateur conducteur non magnétique. Lorsqu'un courant traverse le système, la conductivité dépend de l'orientation respective de l'aimantation de chacune des couches. Par exemple, la différence de résistance à température ambiante peut aller jusqu'à 110% pour les multicouches Co-Fe/Cu donnant de nouvelles idées pour les dispositifs de stockage de l'information. Le premier succès a été une tête de lecture magnétique basée sur une structure de vanne de spin qui permet d'augmenter la densité surfacique de stockage des disques durs. Parallèlement au développement de la tête de lecture à vanne de spin, il a été prédit en 1996 que le moment angulaire de spin d'un courant polarisé en spin pouvait être transféré à l'aimantation d'une couche mince magnétique. Par exemple, dans une vanne de spin, l'aimantation d'une couche est fixée de sorte qu'un courant qui la traverse acquiert une polarisation de spin. Les électrons polarisés, du fait de l'interaction d'échange, vont alors aligner leur moment avec l'aimantation de la couche libre. Pour respecter la loi de conservation du moment angulaire total, l'aimantation de la couche libre aura tendance à s'aligner sur la direction des moments magnétiques du courant de spin, c'est le couple de transfert de spin (STT). Dans le cas du STT, un courant de spin est généré en raison de la structure de bande des matériaux magnétiques. En effet, la forte interaction d'échange a pour conséquence de décaler différemment en énergie les bandes de spin-up et de spin-down qui sont à l'origine du moment ferromagnétique. De ce décalage des bandes, des transitions conservant le spin et des probabilités de diffusion dépendant du spin, il résulte deux canaux de conduction différents.

La découverte de la GMR a été le point de départ d'un nouveau domaine de recherche en magnétisme : l'électronique de spin. Pour répondre à la nécessité d'augmenter la densité, la vitesse de fonctionnement et de

réduire la consommation d'énergie des dispositifs de stockage de l'information, les matériaux magnétiques font l'objet de recherches intenses. La possibilité de déposer des couches minces d'une dizaine de nanomètre ou moins a permis de mieux contrôler l'anisotropie des matériaux magnétiques et d'obtenir un cycle d'hystérésis de l'aimantation qui est essentiel pour développer des mémoires magnétiques. De plus, c'est un point clé d'avoir un moyen efficace de manipuler leur aimantation pour coder l'information. Avant l'émergence de l'électronique de spin, seuls les champs magnétiques étaient utilisés pour lire et écrire l'information. La génération de courants polarisés en spin, leur injection dans des structures magnétiques complexes et les couples de transfert de spin ont été des résultats qui ont révolutionné ce domaine. Plus récemment, une nouvelle façon de générer des courants de spin et de créer un couple sur l'aimantation a été envisagée : les couples de spin-orbite (SOT). A l'origine de ce phénomène, il y a le couplage spin-orbite (SOC) qui peut être compris comme le mouvement de l'électron dans le champ électrostatique créé par le proton. Selon la relativité restreinte, l'électron voit alors dans son référentiel, le champ magnétique généré par son propre mouvement. Le SOC est l'interaction entre ce champ et le moment magnétique intrinsèque de l'électron. Le SOC relativiste est à l'origine d'un certain nombre de phénomènes qui sont utilisés pour la manipulation de l'aimantation des matériaux magnétiques.

L'un d'eux est l'effet Hall anomal (AHE). Similaire à l'effet Hall ordinaire (OHE) dans un métal maintenu dans un champ magnétique, il génère une tension transverse via un courant de charge longitudinal, généralement dans un métal ferromagnétique (FM). L'AHE dans les solides dont la symétrie temporelle est brisée en raison du couplage spin-orbite, peut être considéré comme une diffusion dépendant du spin et, en raison de la différence de population entre les porteurs majoritaires et minoritaires dans les ferromagnétiques, une tension transversale peut être mesurée et être utilisée pour sonder localement l'aimantation du matériau.

L'effet Hall de spin (SHE) est un effet très proche de l'AHE dans un matériau non magnétique (NMs). Ainsi, un courant de spin pur est généré et une accumulation de spin de signe opposé apparaît aux bords opposés au lieu d'une tension transverse. En 2007, il a été démontré expérimentalement qu'il est possible d'injecter un courant de spin dans un FM via un NM qui lui est attaché et réciproquement (ISHE : Effet Hall de spin inverse). L'injection d'un courant de spin, créé dans un NM, dans un FM résulte en un STT qui peut être appelé SHE-STT ou SOT. Il faut noter que la polarizatiion en spin à l'interface et l'aimantation du FM sont mutuellement orthogonaux, ce qui implique qu'un courant de charge injecté dans le plan du film ne peut conduire qu'à une polarisation dans le plan à la surface du film. Il est donc nécessaire d'appliquer un champ dans le plan sur un matériau magnétique perpendiculaire afin d'obtenir un couple. Cependant, il a été découvert que le SHE n'est pas le seul mécanisme responsable du couple appliqué sur la couche adjacente. Dans un tel système, la symétrie d'inversion structurelle est brisée par l'interface FM-NM, ce qui donne lieu aux phénomènes dits

galvanique de spin: un courant électrique est induit par une polarisation hors équilibre, mais uniforme, des spins des électrons. En électronique de spin, l'effet galvanique de spin inverse (ISGE), également connu sous le nom d'effet Edelstein, est vraiment intéressant car il génère une polarisation de spin à partir d'un courant électrique.

Ces effets que l'on retrouve dans les matériaux à fort couplage spin-orbit nous donnent des moyens de retourner l'aimantion de matériaux magnétiques. Parmi ces matériaux certains présentent des propriétés très intéressantes.

Le GdFeCo est un alliage terre rare-métal de transition amorphe. Le magnétisme de cet alliage provient de deux sous-réseaux différents qui sont couplés de manière antiferromagnétique. En raison de cette configuration unique, ses propriétés magnétiques (aimantation nette, anisotropie et température de Curie) peuvent être ajustées en changeant sa composition. De plus, une autre particularité du GdFeCo réside dans les différents facteurs Landé g des éléments de terre rare ($g_{Gd} \approx 2$) et de métal de transition ($g_{FeCo} \approx 2.2$) entrainant différentes températures de compensation de l'aimantation et du moment angulaire, auxquelles, respectivement, les aimantations et les moments angulaires des deux sous-réseaux ont la même amplitude mais des directions opposées. La composition typique des films minces de GdFeCo utilisés dans de nombreuses applications est $Gd_x(Fe_{90}Co_{10})_{100-x}$ et selon celle-ci ou la température, l'aimantation totale peut être dominée soit par le moment total du sous-réseau de Gd, soit par le moment total du sous-réseau de FeCo. Les films minces de GdFeCo sont bien connus pour présenter de nombreuses caractéristiques intéressantes en électronique de spin. Parmi ces propriétés, l'aimantation perpendiculaire au plan du film peut être stabilisée avec de faibles anisotropies, ce qui n'est pas encore bien compris et le faible champ parasite dû à l'alignement antiferromagnétique des moments n'est pas suffisant pour l'expliquer.

En plus des champs magnétiques, il a été démontré que l'aimantation du GdFeCo peut être est renversée soit par SOT ou par une seule impulsion laser femtoseconde par retournement tout-optique (AOS). Le GdFeCo semble également être un bon candidat pour être intégré dans des dispositifs à parois de domaines. Proposées il y a 15 ans, les "racetrack memories" sont des pistes nanométriques magnétiques dans lesquels les données sont stockées dans des séquences de domaines magnétiques dont les parois peuvent être déplacées à l'aide de courants de spin pour les amener vers des dispositifs de lecture ou d'écriture. Dans cette technologie, le champ démagnétisant provenant de chaque domaine entraîne de fortes interactions dipolaires entre eux et limite la densité. Dans les matériaux ferrimagnétiques, le champ démagnétisant est réduit et des vitesses élevées ont déjà été démontrées dans des pistes de GdFeCo. De plus, ses propriétés magnéto-optiques pourraient être un

moyen intéressant d'unifier l'AOS avec le mouvement des parois de domaine induit par le courant.

Concernant le propagation de parois de domaine, les pistes d'antiferromagnétiques synthétiques (SAF) qui consiste en un fil nanoscopique constitué de deux couches magnétiques couplées antiferromagnétiquement, semblent être plus performantes que des couches simples. Elles ont déjà été testées et il a été observé que le champ démagnétisant était réduit ainsi qu'un nouveau couple chiral de couplage d'échange qui est directement proportionnel à la force du couplage d'échange antiferromagnétique entre les deux couches permettant des vitesses élevées jusqu'à 1000 m/s. La vitesse de la paroi de domaine augmente lorsque le moment net du SAF diminue jusqu'à zéro.

L'objectif principal de cette thèse est le déplacement à grande vitesse des parois de domaines. Nous proposons ici d'essayer de combiner à la fois les propriétés des ferrimagnétiques et des SAF. Ces systèmes présentent un intérêt fondamental élevé puisque nous pouvons observer l'effet de la compensation de l'aimantation, du moment angulaire et de la compensation du moment net dans un seul échantillon.

Pour cette thèse, nous nous sommes concentrés sur des films très minces de 5 nm d'épaisseur de GdFeCo avec l'objectif de favoriser le SOT par rapport au STT. Ainsi, nous ne pouvons pas considérer à première vue que le comportement du matériau est dominé par les propriétés de volume et que les échantillons doivent être sensibles aux interfaces. La compétition entre le champ démagnétisant et l'anisotropie est la condition essentielle pour maintenir l'aimantation perpendiculaire au plan du film. L'objectif étant d'intégrer des films minces de GdFeCo dans différents types d'empilements avec des couches adjacentes nécessaires pour le couplage ou la génération de courant de spin, il est nécessaire de s'intéresser à une étude préliminaire de l'effet des interfaces sur les propriétés magnétiques du ferrimagnétique.
Nous avons montré que dans les monocouches d'alliages ferrimagnétiques $Gd_x(Fe_{90}Co_{10})_{1-x}$ pour x entre 22% et 33%, la composition nécessaire pour atteindre la compensation magnétique peut être décalée jusqu'à 3% en fonction des interfaces. Nous avons constaté que la raison principale est la polarisation bien connue des couches adjacentes avec le fer et le cobalt de notre matériau. Ceci a pour conséquence directe l'augmentation du moment de l'échantillon dans la direction du FeCo et donc la nécessité d'ajouter plus de gadolinium dans l'échantillon pour compenser le moment total net. Nous avons observé que la possibilité de maintenir l'aimantation perpendiculaire au plan du film est également fortement affecté par les interfaces. Même si un champ démagnétisant plus important peut expliquer que l'aimantation de l'échantillon éloigné de la compensation tombe plus facilement dans le plan, cela ne peut pas expliquer le comportement de tous les échantillons considérés.

L'anisotropie dans ces alliages amorphes provient du volume et certains mécanismes ont été observés dans la littérature comme les textures colonnaires, la microcristallinité ainsi que l'anisotropie magnétique et l'anisotropie à l'échelle atomique. Nos mesures ont seulement permis de constater l'état amorphe de nos couches et l'origine de l'anisotropie reste incertaine. Cependant nous disposons maintenant des règles pour ajuster le magnétisme de nos couches ferrimagnétiques et pour les intégrer dans l'empilement antiferromagnétique synthétique.

Ensuite, nous avons montré la possibilité d'obtenir un couplage antiferromagnétique entre deux couches ferrimagnétiques de GdFeCo par le biais d'une intercouche d'Ir en utilisant l'interaction RKKY. Nous avons pu observer les deux premiers pics antiferromagnétiques de l'Ir ainsi qu'un couplage ferromagnétique. Au moyen d'un modèle de Stoner-Wohlfarth, nous avons pu reproduire le comportement que nous avons observé et comprendre l'évolution du cycle d'hystérésis du SAF. Ces résultats confirment les conclusions du chapitre précédent. Nous avons montré que nous pouvons également avoir un SAF avec une compensation des moments nets avec un couplage ferromagnétique entre une couche riche en Gd et une couche riche en FeCo.
De plus, grâce aux propriétés magnéto-optiques du GdFeCo, nous avons démontré qu'il est possible de retourner l'aimantation du SAF avec une impulsion laser femtoseconde. Même si ce n'est pas la partie principale de ce travail, il s'agit d'un moyen supplémentaire de nucléer des domaines et cela pourrait être combiné avec le SOT pour manipuler efficacement l'aimantation dans le SAF.

Dans des dispositifs micrométriques, nous avons ensuite étudié le retournement de l'aimantation sous l'effet de couple de spin dans nos systèmes antiferromagnétiques synthétiques ainsi que dans les couches simples qui les composent. Si le retournement de l'aimantation conventionnel qui requiert un champ magnétique externe a pu être observé, nous avons également trouvé que le renversement s'obtient en l'absence de champ externe. Malgré ce que nous avons pu penser après les premiers résultats, la différence d'anisotropie ne semble pas jouer un rôle, nous pouvons observer un tel retournement en l'absence de champ soit dans Ta/Cu/GdFeCo/Ir/Pt soit dans Ta/Ir/GdFeCo/Cu/Pt. La comparaison essentielle de l'amplitude des boucles a révélé un retournement incomplet de nos dispositifs. Après observation sous un microscope Kerr, il est apparu que le mécanisme sous-jacent est la nucléation par le champ d'Oersted ce qui explique pourquoi l'échantillon avec la champ coercitif le plus élevé ne se retourne pas à champ nul. Cet échantillon présente également un seuil de densité de courant plus élevé, ce qui suggère que la renversement par SOT est affectée par le champ d'Oersted. De plus, le champ d'Oersted conduit à une asymétrie des cycles d'hysterèse obtenus par SOT.
Que ce soit avec un couplage antiferrimagnétique ou ferromagnétique, les bicouches ne sont pas plus efficaces pour le retournement SOT même si la densité de courant nécessaire est du même ordre de grandeur.

En l'absence de champ, la nucléation du champ d'Oersted se produit toujours et nous pouvons à nouveau obtenir des boucles carrées avec une amplitude réduite. Les propriétés des bicouches ne semblent pas apporter d'avantages intéressants sur le retournement induit par le courant.

Enfin, nous avons observé la propagation des parois de domaines dans nos échantillons et nous avons constaté que celle-ci est bel et bien dominée par le SOT. Cependant, il est impossible d'atteindre la densité de courant nécessaire pour obtenir une vitesse de déplacement élevée. En effet, le champ d'Oersted généré est suffisant pour affecter l'aimantation des domaines même s'il n'est pas le mécanisme moteur. Lorsque le mouvement peut encore être observé, les parois de domaines sont d'abord inclinées d'un angle proportionnel à l'intensité du courant. La déformation est symétrique pour les deux parois d'un domaine conduisant à une forme trapézoïdale. Enfin, le champ d'Oersted coupe en deux le domaine dans le fil. De manière surprenante, dans la littérature, même lorsqu'un effet similaire est rapporté, la valeur du champ d'Oersted estimé par une formule empirique est presque deux ordres de grandeur plus bas que ce que nous avons simulé ou observé. La structure de nos échantillons pourrait être impliquée puisque notre matériau magnétique est entouré de couches métalliques hautement conductrices qui peuvent contribuer à la génération d'un champ d'Oersted élevé. De plus, malgré l'effet instantané de ce champ qui est de l'ordre de notre champ coercitif, il est observé pour des impulsions de l'ordre de la microseconde et le chauffage ne peut être négligé. Il accentue probablement la conséquence du champ induit par le courant.

Notre étude préliminaire sur le magnétisme de GdFeCo montre un "ensemble de règles" permettant de faire croître des structures plus avancées et d'ajuster les propriétés de l'empilement selon les besoins. Ces résultats nous ont déjà permis de déposer des multicouches améliorés pour d'autres projets de notre équipe. Cependant, après nos mesures, l'effet des interfaces sur l'anisotropie n'est pas clair. On pourrait d'abord envisager de mesurer le champ de saturation dans des séries d'échantillons. En raison de la complexité des mesures SQUID et des artéfacts possibles provenant des substrats, nous pourrions imaginer des mesures AHE de séries de films complets où les fils pour le contact électrique serait directement soudés sur des morceaux carrées. Par ailleurs, pour approfondir les origines de l'anisotropie du GdFeCo, des mesures EXAFS dans un synchrotron pourraient permettre d'étudier l'anisotropie structurelle à l'échelle atomique.
Puisque ce n'était pas l'objectif de notre projet, nous n'avons pas poursuivi les mesures de retournement tout-optique sur nos échantillons mais il serait très intéressant de l'observer dans des couches de GdFeCo couplées. En particulier, nous pourrions essayer un SAF dans lequelle l'aimantation d'une couche peut être retournée par AOS et l'autre couche ne l'est pas en changeant sa composition afin de voir si l'AOS d'une couche peut

entraîner le retournement de l'autre. En changeant le couplage ou la composition, nous pourrions étudier les effets sur la fluence seuil ou l'échelle de temps du renversement.

Pour résoudre les problèmes causés par le champ d'Oersted, nous avons commencé à étudier l'impact de la réduction de l'épaisseur des couches de cuivre. Avec la bonne composition, proche de la compensation, et en retirant les contatcs en or (pour éviter le stress thermique de la lithographie), nous avons été en mesure d'éliminer les couches de Cu. Néanmoins, les domaines magnétiques ont continué à se former par le champ d'Oersted dans notre dispositif. Avec les compositions et les ordres d'empilement de couches que nous avons considérés, le champ d'Oersted semble être inhérent mais nous pourrions envisager de déposer notre matériau ferrimagnétique directement sur le substrat et d'avoir seulement une couche de recouvrement en Pt. Un autre empilement pourrait inclure un isolant comme couche de recouvrement et une seule couche pour fournir le courant de spin, par exemple Pt/GdFeCo/SiN. Si le problème du champ d'Oersted peut être surmonté, les mesures de vitesse en fonction de la température pourraient s'avérer très intéressantes en combinant la compensation du moment net total, la compensation magnétique de la couche et la compensation du moment angulaire. Même si elles sont moins intéressantes du point de vue de l'application, la propagation de parois de domaine sous l'effet du champ pourrait nous donner des informations, notamment la vitesse maximale atteignable ou les températures de compensation. Nous pourrions également confirmer que nous sommes effectivement en mesure de obtenir de hautes vitesses de déplacement.

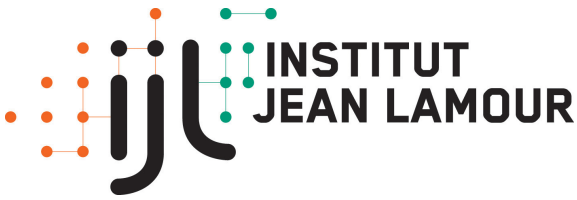

Institut Jean Lamour - UMR 7198

Université de Lorraine

Campus Artem, 2 allée André Guinier, 54011 Nancy, France